

**IMPLEMENTATION AND APPLICATION OF DENSITY FUNCTIONAL
THEORY BASED SYMMETRY-ADAPTED PERTURBATION THEORY FOR
DIMERS, TRIMERS AND MOLECULAR CRYSTALS**

A Dissertation
Presented to
The Academic Faculty

By

Yi Xie

In Partial Fulfillment
of the Requirements for the Degree
Doctor of Philosophy in the
College of Science
School of Chemistry and Biochemistry

Georgia Institute of Technology

Aug 2022

© Yi Xie 2022

**IMPLEMENTATION AND APPLICATION OF DENSITY FUNCTIONAL
THEORY BASED SYMMETRY-ADAPTED PERTURBATION THEORY FOR
DIMERS, TRIMERS AND MOLECULAR CRYSTALS**

Thesis committee:

Dr. C. David Sherrill, Advisor
School of Chemistry and Biochemistry
Georgia Institute of Technology

Dr. Edmond Chow
School of Computational Science and En-
gineering
Georgia Institute of Technology

Dr. Jesse G. McDaniel
School of Chemistry and Biochemistry
Georgia Institute of Technology

Dr. Joshua S. Kretchmer
School of Chemistry and Biochemistry
Georgia Institute of Technology

Dr. Thomas M. Orlando
School of Chemistry and Biochemistry
Georgia Institute of Technology

Date approved: July 25, 2022

To my mother, Jia Yan, who has been supporting me on this long academic journey.

ACKNOWLEDGMENTS

I would like to present my greatest appreciation first to my advisor, Dr. David Sherrill, for his support and guidance in the past five years. He is an astounding scientist, and has always been able to provide insightful comments on the big picture of my research projects, which was crucial for me to take progress on my projects, since capturing the big picture has always been one of my weaknesses. He also cares about his students' academic career, in that he had provided lots of opportunity for us to become a better scientist, from holding regular literature group meetings to bringing us to academic conferences like SETCA and SERMACS. Dr. Sherrill has also always been a kind and patient supervisor; I have to admit that I had made a lot of mistakes during my five-year long Ph. D. study, but he had always been the person that patiently helped me to fix them and ensured that everything was on the right track. It would not be an exaggeration to say that without Dr. Sherrill, I would not be able to accomplish this long journey successfully.

I would also like to thank my current and former committee members: Dr. Jesse McDaniel, Dr. Jean-Luc Brédas, Dr. Thomas Orlando, Dr. Edmond Chow, and Dr. Joshua Kretchmer. The advice and guidance of all of you have been precious for me, and allowed me to know what are my strengths and weaknesses. This helped me to understand what can I do to improve my ability to pursue scientific researches, and the ability to present my researches to the audiences. You are also all very good teachers; I have taken classes, worked as teaching assistant or learned specialized knowledges in your field of study from many of you. These experiences and knowledges are what turns me from a fresh and innocent graduate student to a Ph. D. candidate, who is ready for the upcoming challenges in the future after saying farewell to the campus.

In addition to Dr. Sherrill and my thesis committee, I would like to thank everyone I had worked together with, currently or formerly in the Sherrill Group: Dr. Lori Burns, Dr. Daneil Smith, Dr. Brandon Bakr, Dr. Dominic Sirianni, Dr. Asim Alenaizan, Mr.

Matthew Schieber, Ms. Constance Warden, Mr. Zachary Glick, Mr. Derek Metcalf, Mr. Joseph O'Brien, Dr. Carlos Borca, Dr. Daniel Nascimento, Mr. Andy Jiang, Dr. Jeffrey B. Schriber, Mr. Philip Nelson, Ms. Caroline Sargent, Dr. David Poole, and Dr. Rameshwar Kumawat. The experience working with all of you as colleagues were exceptional, and I have received help in my research and life from many of you. I have also enjoyed having you as my friends in these years, talking on a bunch of different topics: from science, to programming tricks and funny mathematical problems, and even our favorite lunch spot around the campus. Special thanks also goes to professors and researchers outside of Georgia Tech: Dr. Alston Misquitta, Dr. Konrad Patkowski, and Dr. Mary Van Vleet, for the valuable discussions on my research projects. I am also grateful to everyone who guided me on the path of theoretical chemistry before I come to Georgia Tech: Mr. Zuxiong Liu, my first teacher in programming in the middle school, who taught me the basics of programming languages and how powerful the computers are in solving problems in a variety of different fields; Mr. Jinyang Wang, my high school chemistry teacher who had been leading me on the very first steps on studying chemistry; Dr. Zhigang Shuai, my Bachelor dissertation advisor at Tsinghua University, with whom for the first time I start to understand the underlying physical principles of chemistry and how my programming skills are helpful in studying and applying these principles; Dr. So Hirata and Dr. Soohaeng Yoo Willow at University of Illinois at Urbana-Champaign, where I was enrolled in a summer research program, during which I learned how to read scientific literatures and how to work on a research project; Dr. Henry "Fritz" Schaerfer III and Dr. Wesley Allen, who supervised me and taught me the basics of quantum chemistry at the University of Georgia, and also Dr. Justin Turney and Dr. Andreas Copan who taught me the fundamentals of algorithms in quantum chemistry and their implementations.

I would also like this opportunity to thank my father Wentao Xie, and my mother Jia Yan, for raising me up into a healthy and responsible adult, and devoting everything to my education. Since I was a baby of 1 year old, you had been teaching me to learn the Chinese

characters and English alphabets, as well as teaching me simple arithmetics, which allows the success in my academic life after I started to attend school. You have always been seeking the best educational opportunity for me available, from elementary school, middle school to high school. Without all the effort you had made on networking in Shenzhen, it is impossible for me to have the chance to study with Mr. Zuxiong Liu and Mr. Jinyang Wang, and all the other great teachers I had met in my early life. After I left my hometown for Beijing to attend college, and then came to the United States for the Ph. D. study, you have always been caring about me, telling me that everyone in China is missing me and wishing my success.

Finally, I would have to give my deepest gratitude to my beloved one, Xiao Han. It is definitely not easy to pursue a doctoral study, and I had encountered numerous difficulties during my preparation of this thesis. Everytime I am feeling pressured and starting to lose confidence, you are the one standing behind me. When I am making good progress in my research, or even in my diet, you are always there to encourage me, and say that you are proud of me. It is your support and encourage that takes me here, and I wish — will be taking me to the every single milestone in the rest of my life.

TABLE OF CONTENTS

Acknowledgments	iv
List of Tables	x
List of Figures	xii
Summary	xiv
Chapter 1: Introduction	1
1.1 Noncovalent interactions	1
1.2 Supermolecular approach	2
1.3 Symmetry-Adapted Perturbation Theory	5
1.4 Organization of thesis	7
Chapter 2: Implementation of Symmetry-Adapted Perturbation Theory based on density functional theory and using hybrid exchange-correlation kernels for dispersion terms	9
2.1 Abstract	9
2.2 Introduction	10
2.3 Theory	15
2.3.1 JK-based terms	15
2.3.2 Asymptotic correction	19

2.3.3	Dispersion Terms	21
2.3.4	Exchange-Dispersion Scaling	26
2.4	Results and Discussions	28
2.4.1	Exchange-Dispersion Scaling	28
2.4.2	Accuracy of SAPT(DFT) interaction energy	31
2.4.3	Timing Performance	40
2.5	Conclusions	49
Chapter 3: Assessment of three-body dispersion models against coupled-cluster benchmarks for crystalline benzene, carbon dioxide, and triazine . .		51
3.1	Abstract	51
3.2	Introduction	52
3.3	Theory and Method	55
3.3.1	Axilrod–Teller–Muto three-body dispersion	55
3.3.2	Three-body CKS FDDS dispersion	58
3.3.3	Three-body crystal lattice energies	59
3.4	Results and Discussions	61
3.4.1	Dependence of energies on the minimum intermonomer distance, R_{\min}	61
3.4.2	Dependence of energies on the maximum intermonomer distance, R_{\max}	64
3.5	Conclusions	78
Chapter 4: Conclusions and Outlook		80
4.1	Conclusions	80

4.2 Outlook	82
Appendices	85
Appendix A: Supplementary Data for Chapter 2	86
Appendix B: Derivation of Hybrid Kernel FDDS Equations	89
References	95

LIST OF TABLES

2.1	Mean absolute errors (kcal mol^{-1}) and mean unsigned relative errors (%) of the interaction energy components for the Korona S2 test set with various SAPT methods.	33
2.2	Mean absolute error (kcal mol^{-1}) of the interaction energy for S66 with various SAPT methods.	37
2.3	Number of basis functions (N_{bf}), occupied orbitals (N_{occ}), virtual orbitals (N_{vir}) and auxiliary functions (N_{aux}) for different systems and basis sets.	42
2.4	Wall times (in hours) for SAPT(DFT) computations of RDX dimer/aug-cc-pVTZ with hybrid and LHF algorithm.	46
2.5	Wall times (in hours) for PBE0AC SAPT(DFT) computations of the C_{60} -buckycatcher complex using 18 cores of an Intel i9-10980XE processor with hybrid algorithm.	47
3.1	Summary of total three-body contribution to lattice energy (kJ mol^{-1}) of crystalline benzene split by separation domain, for each method involved in this work. Cutoff distances (in \AA) are determined by the smallest of three intermolecular separations, R_{\min} . Percentages reflect the contribution of trimers within each separation domain to the total three-body lattice energy under the corresponding theory level. Errors for each separation range vs. reference CCSD(T)/CBS(a[TQ]Z; δ :aDZ) values in parentheses.	67
3.2	Summary of total three-body contribution to lattice energy (kJ mol^{-1}) of crystalline carbon dioxide split by separation domain, for each method involved in this work. Cutoff distances (in \AA) are determined by the smallest of three intermolecular separations, R_{\min} . Percentages reflect the contribution of trimers within each separation domain to the total three-body lattice energy under the corresponding theory level. Errors for each separation range vs. reference CCSD(T)/CBS(a[TQ]Z; δ :aDZ) values in parentheses.	73

3.3	Summary of total three-body contribution to lattice energy (kJ mol^{-1}) of crystalline triazine split by separation domain, for each method involved in this work. Cutoff distances (in \AA) are determined by the smallest of three intermolecular separations, R_{min} . Percentages reflect the contribution of trimers within each separation domain to the total three-body lattice energy under the corresponding theory level. Errors for each separation range vs. reference CCSD(T)/CBS(a[TQ]Z; δ :aDZ) values in parentheses.	74
3.4	Summary of total three-body contribution to lattice energy (kJ mol^{-1}) of crystalline benzene split by separation domain, for each method involved in this work. Cutoff distances (in \AA) are determined by the largest of three intermolecular separations, R_{max} . Percentages reflect the contribution of trimers within each separation domain to the total three-body lattice energy under the corresponding theory level. Errors for each separation range vs. reference CCSD(T)/CBS(a[TQ]Z; δ :aDZ) values in parentheses.	75
3.5	Summary of total three-body contribution to lattice energy (kJ mol^{-1}) of crystalline carbon dioxide split by separation domain, for each method involved in this work. Cutoff distances (in \AA) are determined by the largest of three intermolecular separations, R_{max} . Percentages reflect the contribution of trimers within each separation domain to the total three-body lattice energy under the corresponding theory level. Errors for each separation range vs. reference CCSD(T)/CBS(a[TQ]Z; δ :aDZ) values in parentheses.	76
3.6	Summary of total three-body contribution to lattice energy (kJ mol^{-1}) of crystalline triazine split by separation domain, for each method involved in this work. Cutoff distances (in \AA) are determined by the largest of three intermolecular separations, R_{max} . Percentages reflect the contribution of trimers within each separation domain to the total three-body lattice energy under the corresponding theory level. Errors for each separation range vs. reference CCSD(T)/CBS(a[TQ]Z; δ :aDZ) values in parentheses.	77
A.1	Mean absolute deviations (kcal mol^{-1}) of the interaction energy components of SAPT2+3(CCD) δ MP2/aug-cc-pVTZ vs SAPT(CCSD)/aug-cc-pVTZ values for the Korona S2 test set.	86
A.2	Mean absolute errors (kcal mol^{-1}) and mean unsigned relative errors (%) of the interaction energy components for the Korona S2 test set with various SAPT methods and the aug-cc-pVTZ basis set.	87
A.3	Mean absolute error (kcal mol^{-1}) of the interaction energy for S66 with various SAPT methods and the aug-cc-pVTZ basis set.	88

LIST OF FIGURES

2.1	LHF orbital/pure ALDA kernel (y-axis) vs non-LHF orbital/hybrid ALDA kernel (x-axis) SAPT(DFT) components for S66 dimers with the aug-cc-pVTZ basis set. All energies are in units of kcal mol ⁻¹ . The components plotted are, from top-left to bottom-right: Electrostatics, exchange, induction, exchange-induction, coupled dispersion, uncoupled dispersion, and uncoupled exchange-dispersion.	28
2.2	Exchange-dispersion fitting results for the S22×5 complexes with the aug-cc-pVTZ basis set. The estimated coupled, non-LHF orbital/hybrid ALDA kernel exchange-dispersion energies from Equation 2.62 (y-axis) are plotted against the coupled, LHF orbital/pure ALDA kernel exchange-dispersion energies (x-axis) computed with Molpro.	29
2.3	Exchange-dispersion fitting results for the S66×8 complexes with the aug-cc-pVTZ basis set. The estimated coupled, non-LHF orbital/hybrid ALDA kernel exchange-dispersion energies from Equation 2.62 (y-axis) are plotted against the coupled, LHF orbital/pure ALDA kernel exchange-dispersion energies (x-axis) computed with Molpro.	30
2.4	Dimer systems tested for program runtime performance: (a) Watson-Crick adenine-thymine complex, (b) RDX dimer and (c) C ₆₀ -buckycatcher complex.	41
2.5	Distribution of wall time among subroutines for each test system with aug-cc-pVDZ and aug-cc-pVTZ basis sets with 6 cores.	43
3.1	Accumulated three-body lattice energy for crystalline benzene as a function of R_{\min} cutoff value, in kJ mol ⁻¹ . MP2+CKS represents MP2 corrected by the three-body CKS FDDS dispersion term, and MP2+ATM represents MP2 corrected by ATM dispersion correction. The suffixes (u), (TT), and (CHG) correspond to undamped, damped with Tang-Toennies damping function[77, 78], and damped with Chai-Head-Gordon damping function[79], respectively.	66

3.2	Accumulated three-body lattice energy for crystalline carbon dioxide as a function of R_{\min} cutoff value, in kJ mol^{-1} . MP2+CKS represents MP2 corrected by the three-body CKS FDDS dispersion term, and MP2+ATM represents MP2 corrected by ATM dispersion correction. The suffixes (u), (TT), and (CHG) correspond to undamped, damped with Tang–Toennies damping function[77, 78], and damped with Chai–Head-Gordon damping function[79], respectively.	68
3.3	Accumulated three-body lattice energy for crystalline triazine as a function of R_{\min} cutoff value, in kJ mol^{-1} . MP2+CKS represents MP2 corrected by the three-body CKS FDDS dispersion term, and MP2+ATM represents MP2 corrected by ATM dispersion correction. The suffixes (u), (TT), and (CHG) correspond to undamped, damped with Tang–Toennies damping function[77, 78], and damped with Chai–Head-Gordon damping function[79], respectively.	69
3.4	Accumulated three-body lattice energy for crystalline benzene as a function of R_{\max} cutoff value, in kJ mol^{-1} . MP2+CKS represents MP2 corrected by the three-body CKS FDDS dispersion term, and MP2+ATM represents MP2 corrected by ATM dispersion correction. The suffixes (u), (TT), and (CHG) correspond to undamped, damped with Tang–Toennies damping function[77, 78], and damped with Chai–Head-Gordon damping function[79], respectively.	70
3.5	Accumulated three-body lattice energy for crystalline carbon dioxide as a function of R_{\max} cutoff value, in kJ mol^{-1} . MP2+CKS represents MP2 corrected by the three-body CKS FDDS dispersion term, and MP2+ATM represents MP2 corrected by ATM dispersion correction. The suffixes (u), (TT), and (CHG) correspond to undamped, damped with Tang–Toennies damping function[77, 78], and damped with Chai–Head-Gordon damping function[79], respectively.	71
3.6	Accumulated three-body lattice energy for crystalline triazine as a function of R_{\max} cutoff value, in kJ mol^{-1} . MP2+CKS represents MP2 corrected by the three-body CKS FDDS dispersion term, and MP2+ATM represents MP2 corrected by ATM dispersion correction. The suffixes (u), (TT), and (CHG) correspond to undamped, damped with Tang–Toennies damping function[77, 78], and damped with Chai–Head-Gordon damping function[79], respectively.	72

SUMMARY

This thesis presents an implementation of the density functional theory based symmetry-adapted perturbation theory [SAPT(DFT)], and its application to interacting systems including dimers, trimers, and molecular crystals. SAPT(DFT) is a computational method for computing interaction energy of noncovalent interactions, which are central to many chemical and biochemical phenomena, such as phase transition, protein-ligand binding and formation of the structure of biomacromolecules. In order to study noncovalent interaction in complex systems, one can use the many-body expansion (MBE) approach to decompose the interaction energy of the complex system into interaction energies of dimers, trimers, tetramers, etc. This makes studying the interaction energies for dimers and trimers meaningful. One of the most important feature of SAPT methods is that their results have very clear physical interpretations; each SAPT term can be assigned to interaction of different physical nature, including electrostatics, exchange-repulsion, induction and dispersion. This allows the physical nature of the interaction of interest to be reflected in addition to the “plain” interaction energy, allowing better understanding of noncovalent interactions.

In Chapter 2, we implemented a variant of SAPT, SAPT(DFT), as a part of the PSI4 quantum chemistry program package, and assessed its performance in accuracy and efficiency. SAPT(DFT) has an advantage of being able to capture the intramonomer electron correlation effects with a relatively low computational cost. This feature makes SAPT(DFT) desirable when one is interested in computing the electrostatics, exchange, induction and dispersion contributions to the interaction energy of an interacting system, many of which requires the intramonomer electron correlation effects to be considered to obtain accurate results. This chapter focused on the treatment of hybrid DFT functionals in SAPT(DFT), in particular the computation of the dispersion energy where a hybrid exchange-correlation kernel is required. We have developed an algorithm that efficiently solves the coupled Kohn-Sham equation with hybrid exchange-correlation kernel, which allows the applica-

tion of SAPT(DFT) with hybrid functionals to dimer systems with sizes comparable to the C₆₀–buckycatcher complex. We have also compared the results of SAPT(DFT) and other SAPT methods to a few benchmark results, and concluded that the accuracy of SAPT(DFT), with a scaling of $O(N^5)$, is comparable to the many-body perturbation theory based SAPT2+ approach, which scales as $O(N^7)$.

In Chapter 3, we attempted to generalize the algorithm developed for the dispersion energy in SAPT(DFT) to the three-body case, and use the many-body expansion approach to study its contribution to the lattice energies of molecular crystals. Unfortunately, our research shows that the SAPT(DFT) dispersion term does not seem to fully capture the three-body dispersion effects in molecular crystals, agreeing the conclusions in previous studies for isolated trimers and liquids, and we attributed this unsatisfactory performance to lack of higher-order exchange-dispersion terms. Nevertheless, we have shown that the Axilrod–Teller–Muto dispersion correction with empirical damping provides a relatively accurate description to the three-body dispersion energy due to fortuitous but consistent error cancellation. We have also analyzed the growth of three-body contribution to crystal lattice energy with respect to the intermonomer distance cutoff of trimers, and it appears that for the molecular crystals where dispersion dominates the three-body contribution to the lattice energy, the error of the computational methods studied in this chapter is mainly contributed by trimers with $R_{\min} < 4 \text{ \AA}$, where R_{\min} is the smallest value among the three pairwise intermonomer closest-contact distances, suggesting the possibility of a drastic reduce in required computational resource for computing the crystal lattice energies by using approximate methods for trimers with $R_{\min} > 4 \text{ \AA}$.

In addition to the advances made in these chapters, this thesis also suggests a few possible future research topics, based on questions arising from the research work related to the thesis. These include implementation of the exchange-dispersion term in SAPT(DFT), which is currently computed by an approximate scaling method in PSI4; implementation of the higher-order exchange-dispersion term for three-body SAPT(DFT) to compensate

the error of three-body SAPT(DFT) dispersion term; and an investigation of the behavior of three-body contribution to the crystal lattice energies for crystals that are not studied in Chapter 3 of this thesis, mainly those consisting polar molecules with stronger dipole-dipole interactions. While we have not explored on these questions here, we hope that further studies on these questions can provide a better insight of understanding noncovalent interactions, as well as allowing development of computational methods in studying these interactions.

CHAPTER 1

INTRODUCTION

1.1 Noncovalent interactions

Noncovalent interactions are the key to many phenomena in chemistry. The simplest example is the stability of condensed phases of matter, such as liquid or crystals. Without noncovalent interactions between molecules, the system will behave like an ideal gas due to the Brownian motion of the molecules, given that the system has a finite temperature. It is the noncovalent interactions that stabilize the molecules in a condensed phase. The noncovalent interactions also govern the phase transition of matters and their thermodynamic properties, such as boiling point, freezing point, and vapor pressure. In sophomore organic chemistry, one usually attempts to compare the boiling points between different organic compounds, based on qualitative statements like “Pentane has stronger intermolecular force between molecules than methane” or “Ethanol has a high boiling point because of the formation of hydrogen bonds”. This type of statements can be sometimes useful, but they clearly lack rigorousness, which makes them unfavorable in serious scientific studies. Also, in some cases there are multiple different types of interactions, and simple qualitative arguments would not be very helpful in explaining how they correlate with each other.

Noncovalent interactions are also critical to the formation of the structures of various biochemical macromolecules, such as protein, DNA and RNA. These interactions are also central to some of the most common biochemical processes, like protein-ligand binding (including drug-protein binding) and protein folding. An important feature of these interactions is that they are highly selective; even a methylation or protonization could completely change the binding property of a ligand. Clearly, a quantitative study will be required to explain the selectivity of these procedures, and furthermore, to develop method-

ologies for predicting them. The physical nature of the interactions are also of interest in explaining these biochemical procedures, for instance, hydrogen bonding and London dispersion could have completely different effects on the binding between biochemical molecules.

All these questions introduced above points to strong interest of studying noncovalent interactions in a quantitative manner. However, such studying in complex systems, like condensed phase or biochemical systems, is not trivial, as they usually involve complex interactions like solvation effects that cannot be easily characterized experimentally, nor can they be easily modeled with high-accuracy quantum mechanical computational methods. For slightly less complicated chemical systems where solvation effects are absent, such as molecular clusters or crystals, the many-body expansion (MBE), which we will describe in more detail in Chapter 3, provides a possible approach to simplify the noncovalent interactions within them. MBE decomposes the interaction energies of a N -body complex system consisting into n -body terms ($n = 2, 3, 4, \dots, N$), each of which consists of the non-additive interaction energies within all n -mers in the N -body system[1, 2]. The most important feature of MBE is probably that the MBE series converges quickly as the number of molecules (or other particles) n increases, so studying noncovalent interactions within dimers and trimers provides a road to understanding noncovalent interactions in complex systems such as molecular crystals.

1.2 Supermolecular approach

By definition, the intermolecular interaction energy of a dimer is the energy difference between the energy of the dimer and the sum of the energies of its two component monomers, i.e., the “stabilization energy” of forming the dimer from two non-interacting monomers. Using the supermolecular approach, one can compute the intermolecular interaction energy of a dimer AB , E_{AB}^{int} :

$$E_{AB}^{\text{int}} = E_{AB} - E_A - E_B, \quad (1.1)$$

where E_A , E_B , and E_{AB} correspond to the energies of monomer A , monomer B , and dimer AB , respectively. It is worth mentioning that we have not specified the computational level of theory for E_A , E_B , and E_{AB} , i.e., we can apply different computational methods to Equation 1.1 to compute the two-body interaction energy E_{AB}^{int} . This allows us to select different computational methods for different chemical systems, in order to achieve the best trade-off between accuracy and computational cost. For benchmark-level accuracy, one usually employs the coupled-cluster singles, doubles, and perturbative triples [CCSD(T)][3] method at the completed basis set (CBS) limit, which is usually achieved by extrapolating the correlation consistent basis sets augmented with diffuse functions (aug-cc-pVXZ, X = D, T, Q). Besides CCSD(T), wavefunction methods such as second-order (MP2) and third-order Møller-Plesset (MP3) perturbation theory are also occasionally used. There are also wavefunction methods optimized specifically for studying noncovalent interactions, such as MP2.5 (average of MP2 and MP3 energies)[4] and spin-component scaled CCSD[5] for noncovalent interactions [SCS(MI)-CCSD][6]. The density functional theory (DFT) is also widely used, but a dispersion correction is needed, usually the -D3[7] or -D4[8] correction, since the typical GGA or hybrid GGA functionals used in DFT do not correctly describe the dispersion interactions between molecules.

For trimers, the interaction energy can be expressed analogously to that of dimers:

$$E_{ABC}^{\text{int}} = E_{ABC} - E_A - E_B - E_C. \quad (1.2)$$

Similar to the case of dimer, the interaction energy of a trimer can be interpreted as the “stabilization energy” to form the trimer. In the many-body expansion, the three-body term is indeed the non-additive contribution of the three-body interaction energy, denoted as

$E_{ABC}^{\text{int.(3)}}$:

$$\begin{aligned} E_{ABC}^{\text{int.(3)}} &= E_{ABC}^{\text{int}} - E_{AB}^{\text{int}} - E_{AC}^{\text{int}} - E_{BC}^{\text{int}} \\ &= E_{ABC} - E_{AB} - E_{AC} - E_{BC} + E_A + E_B + E_C. \end{aligned} \quad (1.3)$$

We will discuss the computation of three-body interaction energies and their contributions to the lattice energies of molecular crystals in Chapter 3.

It is worth noting that the supermolecular approach is subject to the basis set superposition error (BSSE). In Equation 1.1, the computation of E_{AB} involves a larger basis set than those involved in the computations of E_A and E_B . According to the variation principle, a larger basis set is more effective at allowing a low energy to be computed for the system. This results in an overestimation of E_{AB}^{int} in its magnitude, since the dimer is predicted to be “over-stabilized” compared to the sum of the monomers, which have less flexible basis sets. Similar issues apply to the computation of three-body interaction energies for trimers. In order to fix this issue, one common solution is to use the counterpoise (CP) correction[9]. For a dimer AB , one computes E_{AB} , E_A , and E_B , all with the so-called dimer-centered basis set, which includes basis functions constructed on top of all atoms in the dimer AB . For the monomer calculations, fictitious atoms from other monomers (e.g. atoms from monomer B in the computation of E_A) are added to the monomer, and the nuclear charge of these atoms are set to zero. In practice, these fictitious atoms are also called “ghost atoms”. This scheme can be generalized to the three-body case. For a trimer ABC , a trimer-centered basis set will be used in computation of each term in Equation 1.4, introducing the ghost atoms for all monomer and dimer calculations for the atoms that are not included in the original monomer or dimer.

1.3 Symmetry-Adapted Perturbation Theory

While the supermolecular approach can be used to compute the noncovalent interaction energies conveniently, it does not provide a clear physical interpretation of the noncovalent interaction. As we know, there are different types of interactions between molecules, such as hydrogen bonding, dipole-dipole interaction, dipole-induced dipole interaction and London dispersion. In studying noncovalent interactions, it is usually beneficial to understand what the physical nature of the interaction is, but defining these interactions rigorously is not trivial.

The Symmetry-Adapted Perturbation Theory (SAPT) gives an answer to the question above[10–12]. In SAPT, the noncovalent interaction between molecules is modeled as a perturbation to the zeroth-order Hamiltonian, H_0 , which is the Hamiltonian of the non-interacting system. As it turns out, each energy term, with different perturbation order, have a relatively clear physical interpretation: For a dimer, the first-order perturbation corresponds to electrostatic interactions, which includes ionic bonds, hydrogen bonds and permanent dipole-dipole interactions. The second-order perturbation term can be further divided into the induction term and dispersion term. In perturbation theory, the perturbation wavefunction can be represented in the basis of eigenfunctions of H_0 , and the induction term involves wavefunctions with ground-state eigenfunctions on one monomer but a singly-excited wavefunction on the other monomer, and the dispersion involves those in which neither monomer is in its ground-state wavefunction, but instead both are in singly-excited states. Higher-order terms can also be attributed to induction or dispersion based on the behavior of their corresponding eigenfunctions, but in most cases, at least for dimers, second-order terms are sufficient to capture the physical nature of the noncovalent interaction within the system. To satisfy the Pauli exclusion principle, the wavefunctions involved in the perturbation theory scheme above are imposed with an antisymmetry operator (and that is why it is named “symmetry-adapted”), which results in the energy correction terms

on each perturbation order: exchange term on the first-order, and exchange-induction and exchange-dispersion terms on the second-order, depending on whether the eigenfunction is singly or doubly excited. In the convention of our group, we consider the exchange-induction and exchange-dispersion terms as a correction to the induction and dispersion terms respectively.

Given the mathematical formulations above, one can now assign each SAPT term to certain physical type of noncovalent interaction. The ground-state and excited-state eigenfunctions of H_0 can be interpreted as “permanent” and “instantaneous/induced” electric dipoles, respectively. Therefore, the electrostatic term represents the interaction between permanent dipoles (or charges), and other generalized interactions of this type (it is also called a “polarization” term), the induction term includes the dipole-induced dipole interaction, and the dispersion term represents the London dispersion interaction, which is usually interpreted as an interaction between instantaneous electric dipoles. The exchange term captures short-range repulsion, sometimes referred to “steric repulsion” by organic chemists, which is a direct result of Pauli exclusion principle. With these physical interpretation of SAPT terms, SAPT becomes an extremely useful tool to study various noncovalent interactions, by analyzing the contribution of each SAPT term and its corresponding physical interpretation to the total interaction energy of the system.

The most common choice of the zeroth-order Hamiltonian H_0 in SAPT is the Fock operator of the non-interacting system. For a dimer AB , the zeroth-order Hamiltonian would be $H_0 = F_A + F_B$. The simplest SAPT formulation, SAPT0, adds a interaction term V_{AB} to H_0 which represents the noncovalent interaction between monomers A and B . While SAPT0 is computationally cheap, it has an apparent downside of lacking considerations of intramonomer electron correlations, i.e., the electron correlations are only considered between electron pairs with one in each monomers, but those with both electrons in the same monomer are neglected. A common solution to take into account intramonomer correlations is to add the fluctuation potentials W_A and W_B into the SAPT Hamiltonian, each of

which represents the electron correlations within each monomer, and form a perturbation series in terms of all three perturbations, V_{AB} , W_A , and W_B . Such formulation is usually referred to “many-body SAPT”, and is formally called SAPT2, SAPT2+, SAPT2+3, etc.[12] depending on the perturbation order of the fluctuation potentials and the corresponding SAPT terms included in the formalism.

However, these many-body SAPT methods are usually computationally expensive, due to the SAPT terms with high perturbation order. Although these methods can achieve similar accuracy to that of CCSD(T) in computing interaction energies, their computational cost is also comparable to CCSD(T), both of which scaling as $O(N^7)$ (SAPT2 scales as $O(N^6)$, but does not have any intramonomer correlations in the dispersion terms). As an alternative, to capture the intramonomer correlations, the SAPT(DFT) method has been developed over the past two decades. The basic idea of SAPT(DFT) is to replace the Fock operators in the zeroth-order Hamiltonian with the Kohn-Sham operators, which have a term for the exchange-correlation potential, to take the intramonomer correlations into consideration. We will introduce more details on the SAPT(DFT) in Chapter 2.

1.4 Organization of thesis

In the rest of the thesis, research based on the backgrounds described in this introduction will be presented. In Chapter 2, we show an implementation of the SAPT(DFT) method, with improvements specifically on efficient computation of the dispersion term of SAPT(DFT) using hybrid exchange-correlation kernels. This enables the description of monomers with hybrid functionals, where a fraction of Hartree–Fock type exchange term is mixed into the exchange-correlation potential, which improves the accuracy of the electron densities and is thus preferred in application in SAPT(DFT) to describe the monomers. The accuracy and efficiency of our SAPT(DFT) implementation are also tested in this chapter. In Chapter 3, we focus on the contribution of three-body dispersion to crystal lattice energies. We use various computational methods to model these three-body dispersion con-

tributions, including a SAPT(DFT)-like method as studied in Chapter 2. We also study the dependence of intermonomer distances on the three-body dispersion energies of trimers, and use the results to propose a practical workflow to compute these three-body dispersion contributions, which heavily reduces the computational resources needed to compute them.

CHAPTER 2

IMPLEMENTATION OF SYMMETRY-ADAPTED PERTURBATION THEORY BASED ON DENSITY FUNCTIONAL THEORY AND USING HYBRID EXCHANGE-CORRELATION KERNELS FOR DISPERSION TERMS

2.1 Abstract

We report the implementation of a symmetry-adapted perturbation theory algorithm based on a density functional theory description of the monomers [SAPT(DFT)]. The implementation adopts a density-fitting treatment of hybrid exchange-correlation kernels to enable the description of monomers with hybrid functionals, as in the algorithm by Bukowski, Podeszwa, and Szalewicz [Chem. Phys. Lett. **414**, 111 (2005)]. We have improved the algorithm by increasing numerical stability with QR factorization, and optimized the computation of the exchange-correlation kernel with its 2-index density-fitted representation. The algorithm scales as $O(N^5)$ formally and is usable for systems with up to ~ 3000 basis functions, as demonstrated for the C_{60} -buckycatcher complex with the aug-cc-pVDZ basis set. The hybrid-kernel-based SAPT(DFT) algorithm is shown to be as accurate as SAPT(DFT) implementations based on local effective exact exchange potentials obtained from the local Hartree-Fock (LHF) method, while avoiding the lower-scaling [$O(N^4)$] but iterative and sometimes hard-to-converge LHF process. The hybrid-kernel algorithm outperforms Hartree-Fock-based SAPT (SAPT0) for the S66 test set, and its accuracy is comparable to the many-body perturbation theory based SAPT2+ approach, which scales as $O(N^7)$, although SAPT2+ exhibits a more narrow distribution of errors.

2.2 Introduction

Symmetry Adapted Perturbation Theory (SAPT)[10–12] is known as one of the most powerful methods for studying intermolecular interactions. A key advantage of SAPT is its clear physical interpretation; each term in SAPT can be attributed to certain type of intermolecular force. This provides additional physical insight, especially when investigating systems with more complex interactions, such as π - π interactions, which feature important contributions from both electrostatics and London dispersion interactions[13]. Perhaps the most commonly used variant of SAPT, SAPT0, uses a Hartree–Fock description of monomers and the interaction between monomers is modeled as a perturbation to the non-interacting system. While being computationally inexpensive compared to many quantum mechanical models, SAPT0 completely neglects the electron correlation within each monomer, which could lead to inaccurate component energies and total interaction energies. The conventional many-body SAPT methods address this shortcoming by employing a triple-perturbation theory with the intermolecular interaction and intramolecular fluctuation potentials as different perturbations. Unfortunately, this approach is computationally costly, with formal scaling of $O(N^6)$ and higher, and would not be affordable for larger systems, particularly many systems of biological interest.

Alternatively, a mixture of density functional theory (DFT) and SAPT has been developed, known as SAPT(DFT) or DFT-SAPT by different groups of developers. The original idea of SAPT(DFT) was proposed in 2001 by Williams and Chabalowski[14] by replacing the Hartree–Fock description of monomers with Kohn–Sham DFT, expecting that the effect of the exchange-correlation (xc) potential in DFT would go into the Kohn–Sham orbitals, and that these modified orbitals would allow some approximate accounting of intramolecular correlation effects in the SAPT terms. This scheme was extremely appealing in that the intramolecular correlation could be included in SAPT with a drastic reduction in computational time, compared to the conventional many-body SAPT method. However,

while this approach correctly predicted binding for many typical dimer systems (as opposed to supermolecular HF and DFT), it failed to outperform SAPT0 quantitatively, especially in second-order terms. Williams and Chabalowski attributed the failure for second-order terms to the underestimation of the occupied-virtual orbital energy gap in most contemporary DFT functionals[15]. They also noticed the trend that the first-order energies were more likely to fail for large intermolecular distances and nonpolar systems, but the main cause of this problem was not immediately apparent.

Based on these drawbacks of the original SAPT(DFT) scheme, later referred to as SAPT(KS) after SAPT(DFT) was further developed into a more sophisticated theory, Jansen and Hesselmann published an insightful comment[16] pointing out two crucial facts. First, the SAPT(KS) method is not potentially exact, i.e., it would not be exact even if the exact exchange-correlation potential was available, for all terms except for $E_{\text{elst}}^{(1)}$. This is because the zeroth-order wavefunction in SAPT(KS) is the so-called Kohn–Sham wavefunction under the Kohn–Sham DFT framework. The Kohn–Sham system would generate the same density as the electronic system, and thus the correct electrostatic energy, which solely depends on the electronic density. However, $E_{\text{exch}}^{(1)}$ depends on density matrices, and the Kohn–Sham wavefunction are not guaranteed to describe density matrices of the system correctly, and $E_{\text{exch}}^{(1)}$ are therefore not potentially exact. Likewise, this also applies to other higher order terms that have dependencies on density matrices. Furthermore, the second-order energies in SAPT(KS) were calculated using sum-over-states formulae, which corresponds to using what is referred to in SAPT as an “uncoupled” approximation that neglects orbital relaxation effects, i.e., the changes in Coulomb and exchange-correlation potentials in response to the perturbation-induced change of the electron density. In SAPT0 and other higher-order HF-based SAPT theories, “coupled” induction terms have generally been used,[10, 17] and Patkowski et al. have justified this by writing induction energy as the minimum of a functional of the orbitals.[18]

It is worth pointing out that although $E_{\text{elst}}^{(1)}$ is potentially exact, the quantitative ac-

curacy of it was not satisfactory in the original work of Williams and Chabalowski,[14] and they conjectured that the poor accuracy could be due to poor description of electronic density of DFT in the asymptotic area. This conjecture was confirmed by Hesselmann and Jansen (HJ)[19], and they applied an asymptotic correction to the PBE0 functional of Perdew et al.[20, 21] by splicing it with the asymptotically correct LB94 functional of van Leeuwen and Baerends[22] through the gradient-regulation asymptotic correction (GRAC) scheme[23]. The use of PBE0 together with LB94 and the GRAC scheme is referred to as PBE0AC by HJ. Misquitta and Szalewicz (MS) independently confirmed the conjecture above[24], and they proposed to use the Fermi-Amaldi[25] function in the asymptotic range, together with the splicing scheme of Tozer and Handy[26]. Both asymptotic correction schemes correct the wrong asymptotic behavior of the GGA functionals, which decay exponentially while the exact xc-potential should decay as $1/r$. This allowed the accurate reproduction of electron density at long range[27], and thus produced more accurate first-order and induction energies[17, 19, 24]. To include the orbital relaxation effects, HJ and MS independently reformulated the equations for induction[17, 28] and dispersion[29, 30] energies in terms of frequency-dependent density-density response functions, or frequency-dependent density susceptibilities (FDDS). MS and coworkers also pointed out that the “uncoupled” sum-over-states formulae for induction and dispersion energies are equivalent to using the Kohn–Sham wavefunction as an approximation to the exact electronic wavefunction[30], i.e., the uncoupled FDDS is equivalent to that of the Kohn–Sham system, and the coupled FDDS is equivalent to that of the true electronic system. With the coupled FDDS which is available from coupled-perturbed time-dependent density functional theory (TDDFT), the induction and dispersion energies could be potentially exact. On the other hand, HJ have shown that for SAPT(DFT), the correct long-range behavior (and thus physically correct virtual orbital eigenvalues from an asymptotically corrected xc-potential) is not sufficient for computing the dispersion energy accurately without using the coupled FDDS, i.e., the virtual orbital eigenvalue issue is not the only reason of the

failure of SAPT(KS) in second-order terms.

In the above SAPT(DFT) scheme, the most expensive part would be solving for the coupled FDDS from the TDDFT equations, and computing the dispersion energy from the coupled FDDS, both of which scale as $O(N_{occ}^3 N_{vir}^3)$, where N_{occ} and N_{vir} represent the number of occupied and virtual orbitals respectively. The density-fitting technique[31, 32] has been used by both groups developing SAPT(DFT). In both approaches, the adiabatic local-density approximation (ALDA) of the xc kernel has been employed, and it has been shown that such an approximation is satisfactory for computing response properties and dispersion energies[30, 33], but a hybrid ALDA kernel (i.e., linear combination of HF and ALDA kernels) would be required for hybrid xc-potentials in order to reproduce accurate dispersion energies[29, 34].

With the density-fitting technique, the scaling of solving the TDDFT equation with the pure ALDA kernel for FDDS is $O(N_{occ} N_{vir} N_{aux}^2)$ [34], and computing the dispersion energy from the FDDS scales as $O(N_{aux}^3)$ [35], where N_{aux} is the number of density-fitting auxiliary functions. Scalewicz and co-workers developed an approach to compute the coupled FDDS with the hybrid ALDA kernel using the density-fitting approximation[36]. This algorithm has to handle the Hartree–Fock-like exchange terms in the hybrid ALDA kernel, and thus scales as $O(N_{occ}^2 N_{vir}^2 N_{aux})$. On the other hand, Hesselmann and Jansen developed a scheme[34] replacing the Hartree–Fock-like exchange part in the xc-potential by a local effective exact exchange potential, which is obtained from the local Hartree–Fock (LHF) method by Della Sala and Görling[37]. They have also shown in the same work that combining this localized xc-potential, named LPBE0AC, and the pure ALDA kernel generates nearly identical dispersion energies as the non-localized PBE0AC potential combined with a hybrid ALDA kernel. Both approaches have enabled the use of a hybrid functional in SAPT(DFT), with one nominally scaling as $O(N^5)$ and another as $O(N^4)$, but the latter has a larger prefactor due to the self-consistent LHF calculation. It is also worth pointing out that even if the LHF approach has a $O(N^4)$ scaling for the coupled dispersion term

with density-fitting, the exchange-dispersion term, whether uncoupled or coupled, would not benefit significantly from density-fitting and still scales as $O(N^5)$ nominally.

One main restriction in applying SAPT(DFT) to larger systems is the need to generate intermediate tensors that are too large to store in main memory, so they must be stored on disk. In the SAPT2020 code developed by Szalewicz and co-workers[38], the disk space requirement is $O(N^4)$ for hybrid functionals, which should limit the size of the system to roughly 1000 basis functions, although the user has the choice to use non-hybrid functionals to avoid this limitation. Another major improvement on the SAPT(DFT) dispersion algorithm was the use of a 2-index representation $(P|f_{xc}|Q)$ for the xc kernel by Pitoňák and Hesselmann[39], instead of the 3-index representation $(ia|f_{xc}|P)$ used in earlier work[34, 36]. In addition to the 2-index representation, Pitoňák and Hesselmann also introduced a grid-free algorithm[39] identical to grid-free DFT methods of Almlöf and others[40–42], reducing the cost computing $(P|f_{xc}|Q)$ significantly by avoiding computations on a grid, which typically has a size of 10^5 to 10^6 for larger systems.

In this work, we introduce and implement an algorithm for SAPT(DFT) based on the algorithms by Jansen and Szalewicz, with substantial improvements for the dispersion terms. Our algorithm is capable of computations with hybrid functionals without the use of LHF approximations, while reducing the disk requirement to $O(N^3)$ by careful handling of 4-index integrals and 4-index tensors, allowing the code to work for larger systems with up to 3000 basis functions. We have also integrated Pitoňák and Hesselmann’s 2-index xc kernel representation[39] into our code with support for hybrid ALDA kernels. In addition, while Ref. 43 has suggested an effective method for estimating coupled exchange-dispersion energies by scaling the uncoupled energies by a fixed factor, we noticed that the factor would be accurate only for uncoupled exchange-dispersion energies computed from Kohn–Sham orbitals with the LHF approximation; therefore, we have also estimated and tested a new scaling factor for non-LHF orbitals, using the S22×5 and S66×8 data sets[44–47].

In this work we report details of our implementation and the aforementioned new scal-

ing factor to estimate coupled exchange-dispersion energies from uncoupled ones, we test the accuracy of the interaction energies and their components, and we examine the computational efficiency of the code. Our SAPT(DFT) code is publicly available as part of the open-source PSI4 quantum chemistry program package[48].

2.3 Theory

2.3.1 JK-based terms

In our SAPT(DFT) code, the first-order (electrostatics and exchange) and induction terms can be computed from the molecular orbital (MO) coefficients and generalized Coulomb and Exchange (J and K) matrices, in addition to the coupled-perturbed Kohn–Sham (CPKS) amplitudes for coupled induction energies. As opposed to the usual JK matrices which are functionals of the density matrix, generalized JK matrices are functions of arbitrary matrices \mathbf{D} of size $N_{\text{AO}} \times N_{\text{AO}}$, where N_{AO} is the number of atomic orbitals:

$$(\mathbf{J}[\mathbf{D}])_{\mu\nu} = \sum_{\lambda\sigma} \mathbf{D}_{\lambda\sigma} (\mu\nu|\lambda\sigma), \quad (2.1)$$

$$(\mathbf{K}[\mathbf{D}])_{\mu\nu} = \sum_{\lambda\sigma} \mathbf{D}_{\lambda\sigma} (\mu\lambda|\nu\sigma). \quad (2.2)$$

details are suggested to refer to Ref. 10 and 49. Here we follow the equations of Ref. 34 for electrostatics, exchange, and induction terms. We do not repeat the derivation of these equations here, but we refer the reader to Refs. 10, 34 and 49 for more details on the origins of the working equations for these JK-based terms. We will be using the element-wise dot products in the following equations. The dot product between square matrices \mathbf{A} and \mathbf{B} is defined as

$$\mathbf{A} \cdot \mathbf{B} = \sum_{i,j} A_{ij} B_{ij} = \text{Tr}(\mathbf{AB}) \quad (2.3)$$

The electrostatics energy is given by

$$E_{\text{elst}}^{(1)} = 2\mathbf{P}^A \cdot \mathbf{V}^B + 2\mathbf{P}^B \cdot \mathbf{V}^A + 4\mathbf{P}^B \cdot \mathbf{J}^A + V_{\text{nuc}}, \quad (2.4)$$

where \mathbf{P}^X ($X = \text{monomer } A, B$) is the one-particle density matrix, constructed from the occupied-orbital columns of each isolated-monomer SCF coefficient matrix,

$$\mathbf{P}^X = \mathbf{C}^{X,occ}(\mathbf{C}^{X,occ})^\dagger, \quad (2.5)$$

\mathbf{V}^X the nuclear potential, \mathbf{J}^X the Coulomb matrix, and V_{nuc} the (intermolecular) nuclear repulsion energy. The first two terms of Equation 2.4 provide electron-nuclear attraction, and the third term provides electron-electron repulsion ($\mathbf{P}^A \cdot \mathbf{J}^B = \mathbf{P}^B \cdot \mathbf{J}^A$ so we have combined these terms).

The exchange energy in the S^2 approximation (i.e., linear approximation in terms of permutation operator in the antisymmetrizer) is given by

$$\begin{aligned} E_{\text{exch}}^{(1)}(S^2) = & -2(\mathbf{P}^A \mathbf{S}^{\text{AO}} \mathbf{P}^B \mathbf{S}^{\text{AO}} \mathbf{P}^{A,vir}) \cdot \boldsymbol{\omega}^B - 2(\mathbf{P}^B \mathbf{S}^{\text{AO}} \mathbf{P}^A \mathbf{S}^{\text{AO}} \mathbf{P}^{B,vir}) \cdot \boldsymbol{\omega}^A \\ & -2(\mathbf{P}^{A,vir} \mathbf{S}^{\text{AO}} \mathbf{P}^B) \cdot \mathbf{K} [\mathbf{P}^A \mathbf{S}^{\text{AO}} \mathbf{P}^{B,vir}], \end{aligned} \quad (2.6)$$

where $\mathbf{P}^{X,vir}$ is a density-like matrix, but constructed from the virtual-orbital columns of the SCF coefficient matrices,

$$\mathbf{P}^{X,vir} = \mathbf{C}^{X,vir}(\mathbf{C}^{X,vir})^\dagger, \quad (2.7)$$

and $\boldsymbol{\omega}^X$ represents the electrostatic potential generated by the electrons and nuclei of monomer X,

$$\boldsymbol{\omega}^X = 2\mathbf{J}^X + \mathbf{V}^X, \quad (2.8)$$

and \mathbf{S}^{AO} is the overlap matrix under the atomic orbital basis.

The full S^∞ exchange energy (without the S^2 approximation) is given by

$$\begin{aligned}
E_{\text{exch}}^{(1)} &= -2\mathbf{P}^A \cdot \mathbf{K}^B + 2\mathbf{T}^{AB} \cdot (\mathbf{h}^A + \mathbf{h}^B) \\
&\quad + 2\mathbf{T}^{AA} \cdot \mathbf{h}^B + 2\mathbf{T}^{BB} \cdot \mathbf{h}^A \\
&\quad + 2\mathbf{T}^{BB} \cdot \mathbf{W}^{AB} + 2\mathbf{T}^{AA} \cdot \mathbf{W}^{AB} \\
&\quad + 2\mathbf{T}^{BB} \cdot \mathbf{W}^{AA} + 2\mathbf{T}^{AB} \cdot \mathbf{W}^{AB},
\end{aligned} \tag{2.9}$$

where

$$\mathbf{h}^X = \mathbf{V}^X + 2\mathbf{J}^X - \mathbf{K}^X, \tag{2.10}$$

$$\mathbf{T}^{XY} = \mathbf{C}^{X,\text{occ}} \mathbf{T}_{\text{MO}}^{XY} (\mathbf{C}^{Y,\text{occ}})^\dagger, \tag{2.11}$$

$$\mathbf{W}^{XY} = 2\mathbf{J} [\mathbf{T}^{XY}] - \mathbf{K} [\mathbf{T}^{XY}], \tag{2.12}$$

$$\mathbf{T} = \begin{bmatrix} \mathbf{1} & \mathbf{S}^{MO} \\ (\mathbf{S}^{MO})^\text{T} & \mathbf{1} \end{bmatrix}^{-1} - \begin{bmatrix} \mathbf{1} & \mathbf{0} \\ \mathbf{0} & \mathbf{1} \end{bmatrix}, \tag{2.13}$$

$\mathbf{T}_{\text{MO}}^{XY}$ is the block of \mathbf{T} corresponding to molecular orbitals of X in rows and Y in columns, and \mathbf{S}^{MO} is the overlap matrix under the molecular orbital basis.

The induction energy, which consists of the interaction arising from the perturbation of monomer A by the (unperturbed) static electric field of monomer B ($E_{\text{ind}}^{(2)}(A \leftarrow B)$), and *vice versa* ($E_{\text{ind}}^{(2)}(A \rightarrow B)$), is given by

$$E_{\text{ind}}^{(2)}(A \leftarrow B) = 2\mathbf{x}^A \cdot \tilde{\boldsymbol{\omega}}^B, \tag{2.14}$$

$$E_{\text{ind}}^{(2)}(A \rightarrow B) = 2\mathbf{x}^B \cdot \tilde{\boldsymbol{\omega}}^A. \tag{2.15}$$

\mathbf{x}^X represents the response of monomer X to the electric potential of the other monomer, solved for using coupled-perturbed Kohn–Sham as described below, and expressed in the basis of occupied and virtual molecular orbitals of monomer X . $\tilde{\omega}^X$ is the electric potential of monomer X (Equation 2.8, originally expressed in the atomic orbital basis) transformed into the occupied-virtual MO product space of monomer Y so that it can be dotted against \mathbf{x}^Y in the above expressions for the induction energy,

$$\tilde{\omega}^X = (\mathbf{C}^{Y,occ})^\dagger \boldsymbol{\omega}^X \mathbf{C}^{Y,vir}. \quad (2.16)$$

The exchange-induction term under the S^2 approximation is

$$\begin{aligned} E_{\text{exch-ind}}^{(2)}(S^2)(A \leftarrow B) &= 2\mathbf{x}^A \cdot ((\mathbf{C}^{A,occ})^\dagger (-\mathbf{K}^B - 2\mathbf{J}[\mathbf{O}] + \mathbf{K}[\mathbf{O}] + 2\mathbf{J}[\mathbf{P}^B \mathbf{S}^{AO}]) \\ &\quad + \mathbf{S}^{AO} \mathbf{P}^B (-\mathbf{h}^A + \mathbf{S}^{AO} \mathbf{P}^A \boldsymbol{\omega}^B + \boldsymbol{\omega}^A \mathbf{P}^B \mathbf{S}^{AO} - \mathbf{K}[\mathbf{O}]^T) \\ &\quad + (-\mathbf{h}^B + \boldsymbol{\omega}^B \mathbf{P}^A \mathbf{S}^{AO} - \mathbf{K}[\mathbf{O}]) \mathbf{P}^B \mathbf{S}^{AO}) \mathbf{C}^{A,vir}, \end{aligned}$$

$$\begin{aligned} E_{\text{exch-ind}}^{(2)}(S^2)(A \rightarrow B) &= 2\mathbf{x}^B \cdot ((\mathbf{C}^{B,occ})^\dagger (-\mathbf{K}^A - 2\mathbf{J}[\mathbf{O}] + \mathbf{K}[\mathbf{O}] + 2\mathbf{J}[\mathbf{P}^A \mathbf{S}^{AO}]) \\ &\quad + \mathbf{S}^{AO} \mathbf{P}^A (-\mathbf{h}^B + \mathbf{S}^{AO} \mathbf{P}^B \boldsymbol{\omega}^A + \boldsymbol{\omega}^B \mathbf{P}^A \mathbf{S}^{AO} - \mathbf{K}[\mathbf{O}]^T) \\ &\quad + (-\mathbf{h}^A + \boldsymbol{\omega}^A \mathbf{P}^B \mathbf{S}^{AO} - \mathbf{K}[\mathbf{O}]) \mathbf{P}^A \mathbf{S}^{AO}) \mathbf{C}^{B,vir}, \end{aligned}$$

where

$$\mathbf{O} = \mathbf{P}^A \mathbf{S}^{AO} \mathbf{P}^B. \quad (2.19)$$

For uncoupled induction and exchange-induction energies, the amplitudes are

$$(\mathbf{x}^X)_r^a = -\frac{(\tilde{\omega}^X)_r^a}{\epsilon_r - \epsilon_a}, \quad (2.20)$$

where a and r run over all occupied and virtual molecular orbitals respectively of monomer X .

For coupled induction, the amplitudes are solved from the CPKS equations, where \mathbf{x} and $\boldsymbol{\omega}$ are treated as $(N_{occ}N_{vir})$ -dimensional vectors. The CPKS equations can be expressed as the following linear system of equations:

$$\mathbf{H}^{(1)}\mathbf{x}^A = \boldsymbol{\omega}^B, \quad (2.21)$$

$$\mathbf{H}^{(1)}\mathbf{x}^B = \boldsymbol{\omega}^A, \quad (2.22)$$

and the CPKS Hessian $\mathbf{H}^{(1)}$ can be constructed from

$$\mathbf{H}^{(1)} = \mathbf{d} + 4\mathbf{H}_0^{(1)} + \mathbf{H}_r^{(1)}, \quad (2.23)$$

$$(\mathbf{d})_{ar,a'r'} = (\epsilon_r - \epsilon_a) \delta_{aa'} \delta_{rr'}, \quad (2.24)$$

$$\left(\mathbf{H}_0^{(1)}\right)_{ar,a'r'} = (ar|a'r') + \int \phi_a \phi_r \phi_{a'} \phi_{r'} \frac{\delta v_{xc}}{\delta \rho} d\mathbf{r}, \quad (2.25)$$

$$\left(\mathbf{H}_r^{(1)}\right)_{ar,a'r'} = -\xi [(aa'|rr') + (ar'|a'r)]. \quad (2.26)$$

The CPKS equations can be solved by the conjugate gradient solver in PSI4 designed for CPHF, with a slight modification by adding a v_{xc} matrix to the \mathbf{J} matrix and scaling \mathbf{K} by ξ , where v_{xc} is the exchange-correlation potential, and ξ is the fraction of Hartree-Fock exchange in the DFT xc potential.

2.3.2 Asymptotic correction

As introduced before, HJ performed asymptotic correction on PBE0 by splicing it with LB94 using the gradient-regulated asymptotic correction (GRAC) scheme by Grüning et

al.[23] Another common correction scheme, the Fermi-Amaldi-Tozer-Handy correction, mainly adopted by MS and coworkers is not yet implemented in PSI4.

In the framework of GRAC, the general form of the asymptotically corrected xc potential can be written as a linear combination of the bulk region potential v_{xc}^b and the asymptotic correction potential v_{xc}^a :

$$v_{xc}^{b-AC}(\mathbf{r}) = [1 - f(\mathbf{r})]v_{xc}^b(\mathbf{r}) + f(\mathbf{r})v_{xc}^a(\mathbf{r}). \quad (2.27)$$

In the instance of PBE0AC, v_{xc}^b is PBE0 which is the base functional, and v_{xc}^a is LB94, a functional that is asymptotically correct but behaves poorly in the bulk region. In the GRAC scheme, the switching function $f(\mathbf{r})$ takes the following form:

$$f[x(\mathbf{r})] = \frac{1}{1 + e^{-\alpha[x(\mathbf{r})-\beta]}}, \quad (2.28)$$

$$x(\mathbf{r}) = \frac{|\nabla\rho(\mathbf{r})|}{\rho^{4/3}(\mathbf{r})}. \quad (2.29)$$

With the form given, the switching function $f(\mathbf{r})$ approaches to unity in the asymptotic region and vanishes in the bulk region. As a result, the combined functional behaves similarly to PBE0 at short intermolecular distance r and to LB94 at large r , thus being able to combine the advantages of both functionals and reproduce accurate electron densities over all distances. One example can be found in Figure 2 of Ref. 27, where the radial density of neon atom is computed with HF, PBE0, LB94 and PBE0AC, and compared with coupled-cluster singles, doubles, and perturbative triples [CCSD(T)][3] densities as a benchmark[27, 50].

As a consequence of the discontinuity of the exact xc potential as the number of electrons increases[51], the exact potential should not vanish asymptotically but converge to,

according to the generalized Koopmans' theorem[26]:

$$v_{XC,\sigma}(\infty) = \epsilon_{\text{HOMO},\sigma} + I_{\sigma}, \quad (2.30)$$

where $\epsilon_{\text{HOMO},\sigma}$ is the highest occupied Kohn–Sham orbital eigenvalue, and I_{σ} is the ionization potential for removing the highest occupied electron of spin σ . Therefore, the value $v_{XC,\sigma}(\infty)$, also known as the asymptotic shift, becomes an essential parameter for the GRAC scheme to determine the proper asymptotic behavior of the corrected potential. In practice, $\epsilon_{\text{HOMO},\sigma}$ is easily obtained from a conventional KS-DFT calculation (without asymptotic shift), and the ionization potential is either obtained experimentally or computationally by explicitly computing the energy of the ionized state (e.g., M^+ cation for a neutral molecule M).

2.3.3 Dispersion Terms

In the traditional SAPT theory, the second-order dispersion term is written in a sum-over-state form, as introduced before:

$$E_{disp}^{(2)} = -4 \sum_{abrs} \frac{|(ar|bs)|^2}{\epsilon_{ar} + \epsilon_{bs}}. \quad (2.31)$$

As mentioned before, the sum-over-state expression of the dispersion term corresponds to the uncoupled approximation of the dispersion energy of the system. With the Casimir-Polder identity, the dispersion term can be rewritten in terms of the uncoupled FDDS[52, 53]:

$$E_{disp}^{(2)} = -\frac{1}{2\pi} \int_0^{\infty} d\omega \int d\mathbf{r}_A d\mathbf{r}'_A d\mathbf{r}_B d\mathbf{r}'_B \frac{1}{|\mathbf{r}_A - \mathbf{r}_B|} \frac{1}{|\mathbf{r}'_A - \mathbf{r}'_B|} \chi_0^A(\mathbf{r}_A, \mathbf{r}'_A | i\omega) \chi_0^B(\mathbf{r}_B, \mathbf{r}'_B | i\omega), \quad (2.32)$$

$$\chi_0(\mathbf{r}, \mathbf{r}' | i\omega) = 4 \sum_{ar} \frac{\epsilon_{ar}}{\epsilon_{ar}^2 + \omega^2} \phi_i(\mathbf{r}) \phi_a(\mathbf{r}) \phi_i(\mathbf{r}') \phi_a(\mathbf{r}'). \quad (2.33)$$

In Equation 2.33, the FDDS is represented in the position space, and this gives it a clear physical interpretation: the linear response of density at the coordinate \mathbf{r}' with respect to a perturbation of density at the coordinate \mathbf{r} under the frequency $i\omega$ in the frequency domain. As mentioned above, the uncoupled FDDS $\chi_0(\mathbf{r}, \mathbf{r}'|\omega)$ describes the linear response property of the Kohn–Sham wavefunction, and Equation 2.32 would also give the dispersion energy of the Kohn–Sham system[30]. The results in Ref. 29 shows that such an approximation would result in an overestimation of dispersion energies by more than 30% on average. To compute the coupled dispersion energy, one would need to solve for the coupled FDDS from the TDDFT equation. In the response function formalism, the equation is written as

$$\chi(\mathbf{r}, \mathbf{r}'|\omega) = \chi_0(\mathbf{r}, \mathbf{r}'|\omega) + \int d\omega d\mathbf{r}_1 d\mathbf{r}_2 \chi_0(\mathbf{r}, \mathbf{r}_1|\omega) \left[\frac{1}{r_{12}} + f_{xc}(\mathbf{r}_1, \mathbf{r}_2, \omega) \right] \chi(\mathbf{r}_2, \mathbf{r}'|\omega). \quad (2.34)$$

With the density fitting technique, the FDDS can be expressed under the auxiliary basis set representation with matrix elements $(P|\chi|Q)$. For non-hybrid xc potential and kernel, the solution of the coupled FDDS with the matrix representation is:

$$\chi = \chi_0 + \chi_0 \mathbf{S}^{-1} \mathbf{W} (\mathbf{S} - \chi_0 \mathbf{S}^{-1} \mathbf{W})^{-1} \chi_0, \quad (2.35)$$

where \mathbf{S} is the Coulomb metric in the auxiliary basis set

$$\mathbf{S}_{PQ} = (P | \frac{1}{r_{12}} | Q), \quad (2.36)$$

and the operator \mathbf{W} denotes the interelectronic interactions including Coulomb, exchange, and correlation effects:

$$\mathbf{W}_{PQ} = \left(P \left| \frac{1}{r_{12}} \right| Q \right) + (P | f_{xc} | Q). \quad (2.37)$$

The xc kernel can be computed with a grid-free DFT algorithm proposed by Almlöf and co-workers[39–42], where the xc kernel functional is imposed on the electron density operator ($P|\rho|Q$) diagonalized under the DF auxiliary basis representation.

The dispersion energy may be computed by integrating over the FDDS:

$$E_{disp}^{(2)} = -\frac{1}{2\pi} \int_0^\infty d\omega (\mathbf{S}^{-1} \boldsymbol{\chi}^A \mathbf{S}^{-1}) \boldsymbol{\chi}^B. \quad (2.38)$$

For a hybrid xc kernel, we have derived a set of equations based on the algorithm by Bukowski and co-workers in 2005[36]. Without the density fitting approximation, the FDDS (expressed in the orbital representation $\mathbf{C}_{ar,a'r'}(i\omega)$) can be solved from the following matrix equation from coupled Kohn-Sham theory:

$$(\mathbf{H}^{(2)} \mathbf{H}^{(1)} + \omega^2 \mathbf{I}) \mathbf{C}(i\omega) = -4\mathbf{H}^{(2)}, \quad (2.39)$$

where \mathbf{I} denotes the unit matrix of dimension $N_{occ}N_{vir}$, $\mathbf{H}^{(1)}$ defined by Equation 2.23, and $\mathbf{H}^{(2)}$ is written as the following:

$$\mathbf{H}^{(2)} = \mathbf{d} + \mathbf{H}_r^{(2)}, \quad (2.40)$$

$$(\mathbf{H}_r^{(2)})_{ar,a'r'} = -\xi [(aa'|rr') - (ar'|a'r)], \quad (2.41)$$

and \mathbf{d} is given in Equation 2.24.

In the work of Bukowski et al.[36], they proposed an algorithm to solve the equation above utilizing the density fitting technique. The algorithm lowers the $O(N^6)$ scaling of the non-DF version to $O(N^5)$, but it has several downsides: First, their algorithm is iterative, and we later discovered that this would not be necessary. Second, the xc kernel is represented as a 3-index tensor in this algorithm, and the evaluation of the kernel is also not as cheap as the grid-free DFT algorithm mentioned above. After utilizing the grid-free DFT

algorithm and the 2-index DF auxiliary basis representation of the xc kernel and FDDS, along with proper arrangement of the procedures of storing 3-index intermediates on disk, we rewrite the results of Bukowski et al. into the following form, which is a modification of Equation 2.35:

$$\chi = \chi'_0 + (\chi'_0 \mathbf{S}^{-1} \mathbf{W} + \frac{1}{4} \mathbf{K}(\mathbf{R}^T)^{-1} \mathbf{S}) [\mathbf{S} - (\chi'_0 \mathbf{S}^{-1} \mathbf{W} + \frac{1}{4} \mathbf{K}(\mathbf{R}^T)^{-1} \mathbf{S})]^{-1} \chi'_0. \quad (2.42)$$

All quantities here are expressed in the density fitting auxiliary basis and have dimension $N_{aux} \times N_{aux}$. The matrix \mathbf{K} includes the effect of Hartree–Fock type exchange integrals in the TDDFT Hessian:

$$\mathbf{K} = -\xi[\mathbf{K}_1(\lambda d) + \mathbf{K}_2(\lambda d)] + \xi^2 \mathbf{K}_{21}(\lambda), \quad (2.43)$$

and \mathbf{K} can be further divided into \mathbf{K}_1 contributed by \mathbf{H}_1 , \mathbf{K}_2 contributed by \mathbf{H}_2 and \mathbf{K}_{21} contributed by their product,

$$[\mathbf{K}_1(\lambda d)]_{PQ} = \sum_{ar, a'r'} (P|ar) \lambda_{ar} d_{ar} [(aa'|rr') + (ar'|a'r)] (a'r'|Q|Q), \quad (2.44)$$

$$[\mathbf{K}_2(\lambda d)]_{PQ} = \sum_{ar, a'r'} (P|ar) \lambda_{ar} d_{ar} [(aa'|rr') - (ar'|a'r)] (a'r'|Q|Q), \quad (2.45)$$

$$[\mathbf{K}_{21}(\lambda)]_{PQ} = \sum_{ar, a'r', a''r''} (P|ar) \lambda_{ar} [(aa''|rr'') - (ar''|a''r)] [(a'a''|r'r'') - (a'r''|a''r')] (a'r'|Q|Q), \quad (2.46)$$

and χ'_0 is the uncoupled FDDS “corrected” by removing the portion of ALDA exchange that is replaced by Hartree–Fock type exchange:

$$\chi'_0 = \chi_0 - \xi \mathbf{K}'_2(\lambda), \quad (2.47)$$

$$[\mathbf{K}'_2(\lambda)]_{PQ} = \sum_{ar, a'r'} (P|ar)\lambda_{ar}[(aa'|rr') - (ar'|a'r)](a'r'|Q), \quad (2.48)$$

$$d_{ar} = \epsilon_r - \epsilon_a, \quad (2.49)$$

$$\lambda_{ar} = -\frac{4}{d_{ar}^2 + \omega^2}, \quad (2.50)$$

and the 3-index tensor $(ar|\mathbf{Q}|Q)$ and matrix \mathbf{R} comes from a QR factorization of the tensor $(ar|Q)$ (as a $N_{occ}N_{vir} \times N_{aux}$ matrix). QR factorization decomposes any matrix into product of an orthogonal matrix \mathbf{Q} and an upper triangular matrix \mathbf{R} . We needed the QR factorization here because the equations above originally include the pseudo-inverse of $(ar|Q)$, which has a relatively large condition number, and QR factorization of such a matrix helps avoid further condition problems when trying to invert it. In the formulae above, what actually appears is the pseudo-inverse of the transposed 3-index tensor $(Q|ar)$:

$$(Q|ar) = (\mathbf{QR})^T = \mathbf{R}^T \mathbf{Q}^T, \quad (2.51)$$

$$[(Q|ar)]^\dagger = \mathbf{Q}(\mathbf{R}^T)^{-1}. \quad (2.52)$$

More details on the derivation of the equations above will be included in Appendix B.

For hybrid functionals ($\xi \neq 0$), the most expensive part of the algorithm is computing the matrices with Hartree–Fock type exchange, i.e. $\mathbf{K}_1, \mathbf{K}_2, \mathbf{K}'_2, \mathbf{K}_{21}$, with a scaling of $O(N_{occ}^2 N_{vir}^2 N_{aux})$. For non-hybrid functionals all these matrices vanish, and the scaling of the algorithm reduces to $O(N_{occ} N_{vir} N_{aux}^2)$. While Equation 2.44–Equation 2.46 seem to be very complicated, the scaling above can be achieved by storing the following intermediate

3-index tensors on the disk:

$$(ar|\mathbf{Y}|Q) = [(a'r|ar') - (aa'|rr')](a'r'|Q), \quad (2.53)$$

$$(ar|\mathbf{Q}_X|Q) = [(a'r|ar') + (aa'|rr')](a'r'|Q), \quad (2.54)$$

$$(ar|\mathbf{Q}_Y|Q) = [(a'r|ar') - (aa'|rr')](a'r'|Q), \quad (2.55)$$

and the \mathbf{K} matrices can be obtained from these intermediates:

$$[\mathbf{K}_1(\lambda d)]_{PQ} = -\xi \sum_{ar} (P|ar) \lambda_{ar} d_{ar} (ar|\mathbf{Q}_X|Q), \quad (2.56)$$

$$[\mathbf{K}_2(\lambda d)]_{PQ} = -\xi \sum_{ar} (P|ar) \lambda_{ar} d_{ar} (ar|\mathbf{Q}_Y|Q), \quad (2.57)$$

$$[\mathbf{K}_{21}(\lambda)]_{PQ} = \xi^2 \sum_{ar} (P|\mathbf{Y}|ar) \lambda_{ar} (ar|\mathbf{Q}_X|Q), \quad (2.58)$$

$$[\mathbf{K}'_2(\lambda)]_{PQ} = -\xi \sum_{ar} (P|ar) \lambda_{ar} (ar|\mathbf{Y}|Q). \quad (2.59)$$

2.3.4 Exchange-Dispersion Scaling

The computation of exchange-dispersion energy has been a challenge in SAPT(DFT). The uncoupled approximation has been shown unsatisfactory, and although Garcia et al.[54] have resolved the problem of the requirement of the storage of 4-index TDDFT amplitudes on disk when computing the coupled exchange-dispersion energy explicitly[43], the coupled exchange-dispersion energy with hybrid kernel might be considerably more computationally demanding than the pure ALDA kernel case implemented by Garcia et al.

Nevertheless, the solution provided by Garcia et al. is valuable, and we should pursue the implementation of coupled exchange-dispersion term with hybrid kernel in the future. One way to avoid the explicit computation of coupled exchange-dispersion energy, proposed by Bukowski et al.[49], is to estimate its value by scaling its uncoupled counterpart:

$$\tilde{E}_{\text{exch-disp,r}}^{(2)} = E_{\text{exch-disp,u}}^{(2)} \cdot \frac{E_{\text{disp,r}}^{(2)}}{E_{\text{disp,u}}^{(2)}}. \quad (2.60)$$

This scaling scheme is straightforward, but was shown by Hesselmann and Korona [43] to strongly underestimate the coupled exchange-dispersion energies for larger values according to results on the S22 \times 5 test set[44]. In the same paper, they proposed to scale the uncoupled exchange-dispersion energy by a fixed factor from linear fitting instead:

$$\tilde{E}_{\text{exch-disp,r}}^{(2)} = \alpha \cdot E_{\text{exch-disp,u}}^{(2)} (\alpha = 0.686361). \quad (2.61)$$

From the results on S22 \times 5, the fixed factor scheme was shown extremely successful for estimating the coupled exchange-dispersion energies, with a mean absolute error of merely 0.03 kcal mol⁻¹ as opposed to 0.19 kcal mol⁻¹ for the conventional scaling scheme. However, these results are based on the local Hartree–Fock approximation for DFT calculations as proposed in Ref 34. As we will demonstrate later, the uncoupled dispersion and exchange-dispersion energies would be heavily affected by the occupied-virtual orbital energy gap, which appears in the denominator of the uncoupled dispersion amplitudes, and differs between LHF and non-LHF algorithms significantly. Fortunately, the linear correlation between exact coupled exchange-dispersion energies and the non-LHF uncoupled values is still satisfactory, and thus we are able to obtain a new scaling factor from linear fitting.

2.4 Results and Discussions

2.4.1 Exchange-Dispersion Scaling

As mentioned above, it is computationally costly to evaluate coupled exchange-dispersion energies with hybrid kernels, and so we wish to estimate these terms by scaling the uncoupled exchange-dispersion energies. However, we cannot use existing scaling factors from the literature using LHF approaches, because the difference in the occupied-virtual orbital energy gap between LHF and non-LHF approaches affects the uncoupled exchange-dispersion energies. We have plotted each SAPT(DFT) energy term calculated from LHF and non-LHF orbitals in Figure 2.1 for the S66 test set[45]. In all SAPT(DFT) calculations in this section, we use the PBE0AC xc potential to generate the Kohn–Sham orbitals, except for calculations adopting the LHF approach, where the exact exchange of PBE0AC would be localized with LHF as described in Ref. 34, and we use the augmented version of the correlation-consistent basis sets of Dunning and coworkers, aug-cc-pVDZ and aug-cc-pVTZ[55, 56].

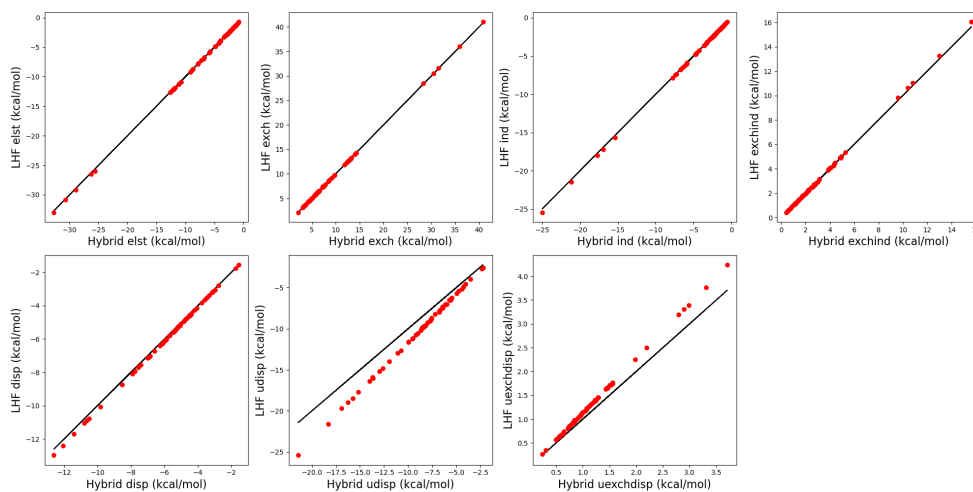


Figure 2.1: LHF orbital/pure ALDA kernel (y-axis) vs non-LHF orbital/hybrid ALDA kernel (x-axis) SAPT(DFT) components for S66 dimers with the aug-cc-pVTZ basis set. All energies are in units of kcal mol^{-1} . The components plotted are, from top-left to bottom-right: Electrostatics, exchange, induction, exchange-induction, coupled dispersion, uncoupled dispersion, and uncoupled exchange-dispersion.

The plots show that while the first-order and induction terms are almost unaffected by the LHF orbitals, the uncoupled dispersion and exchange-dispersion energies are substantially affected. Nevertheless, it is fortunate that the uncoupled terms between LHF and non-LHF orbitals seem to approximately follow a linear relationship, which would be very helpful for us to build up our scaling scheme for the exchange-dispersion energy. It is also worth mentioning that although computed from totally different algorithms, the coupled dispersion energies from the non-LHF potential combined with a hybrid ALDA kernel turn out to be almost identical to their LHF potential / pure ALDA kernel counterparts. From these results, we can safely conclude that we can perform another linear fitting to obtain a new scaling factor appropriate for scaling uncoupled exchange energies computed with non-LHF orbitals.

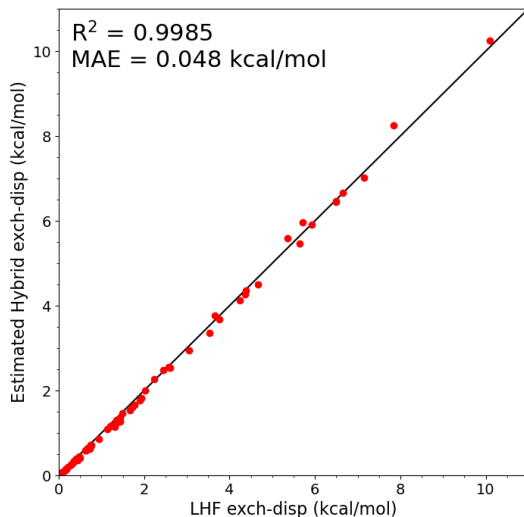


Figure 2.2: Exchange-dispersion fitting results for the $S22 \times 5$ complexes with the aug-cc-pVTZ basis set. The estimated coupled, non-LHF orbital/hybrid ALDA kernel exchange-dispersion energies from Equation 2.62 (y-axis) are plotted against the coupled, LHF orbital/pure ALDA kernel exchange-dispersion energies (x-axis) computed with Molpro.

We perform a linear fit between LHF orbital / pure ALDA kernel coupled exchange-dispersion energies and non-LHF orbital / hybrid ALDA kernel uncoupled exchange-dispersion energies for the $S22 \times 5$ test set. As expected, we are able to establish a linear correlation

here, given by the following expression

$$E_{\text{exch-disp}}^{(2)}(\text{coupled}) \approx \alpha \cdot E_{\text{exch-disp}}^{(2)}(\text{uncoupled}) (\alpha = 0.770). \quad (2.62)$$

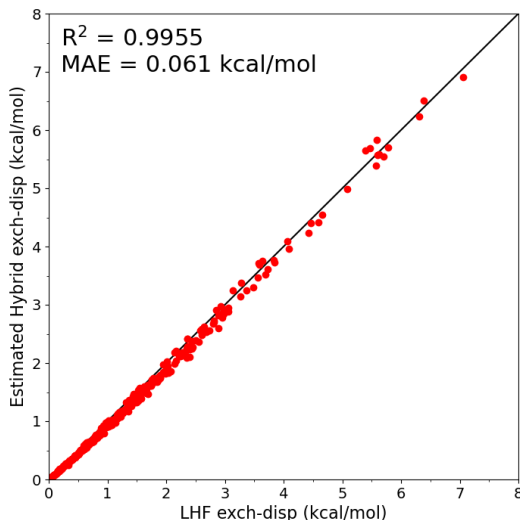


Figure 2.3: Exchange-dispersion fitting results for the $S66 \times 8$ complexes with the aug-cc-pVTZ basis set. The estimated coupled, non-LHF orbital/hybrid ALDA kernel exchange-dispersion energies from Equation 2.62 (y-axis) are plotted against the coupled, LHF orbital/pure ALDA kernel exchange-dispersion energies (x-axis) computed with Molpro.

The mean absolute error of the estimated coupled exchange-dispersion energy is $0.048 \text{ kcal mol}^{-1}$, and the correlation coefficient of the linear fitting is 0.9985 (Figure 2.2). While not quite as good as the results ($0.03 \text{ kcal mol}^{-1}$ and 0.9993) in Ref. 43, this fit is still satisfactory for the purpose of estimating the exchange-dispersion energy in SAPT(DFT). In order to validate the scaling scheme, we scale the uncoupled exchange-dispersion energies of $S66 \times 8$ with the fitted scaling factor 0.770 from $S22 \times 5$ and compare with the reference values from the LHF approach. This estimation has a mean absolute error of $0.061 \text{ kcal mol}^{-1}$ and a correlation coefficient of 0.9955 (Figure 2.3). These results suggest that this scaling scheme should suffice for estimating exchange-dispersion energies in SAPT(DFT) with hybrid functionals when LHF is not used.

2.4.2 Accuracy of SAPT(DFT) interaction energy

To assess the accuracy of termwise and total interaction energies of SAPT(DFT), we compare to benchmark results. For energy components (exchange, electrostatics, induction, and dispersion), SAPT based on CCSD monomer wavefunctions, i.e., SAPT(CCSD), should provide good reference values[57]. Compared to many-body perturbation theory based SAPT, this approach avoids potential poor or oscillatory convergence with respect to the perturbation order of the intramolecular correlation. Unfortunately, SAPT(CCSD) is very computationally costly, and the published SAPT(CCSD) results are only available for a limited set of systems containing no more than 10 atoms[57]. We compare SAPT(DFT) energy components to these available SAPT(CCSD) energy components below.

In order to examine a larger test set that is more inclusive of common types of intermolecular interactions, we also compare SAPT(DFT) energy components to those from the more computationally tractable SAPT2+3(CCD) δ MP2 approach[58] for the S66 set of van der Waals dimers[46, 47]. This method is a many-body perturbation theory approach to SAPT, although it utilizes coupled-cluster theory for dispersion [in particular, the CCSD+ST(CCD) approach of Williams et al.][59]. It has the potential advantage over SAPT(CCSD) that certain terms are included through third order in the intermolecular perturbation \hat{V} , and certain higher-order terms (mainly induction-like) are implicitly included through the “ δ MP2” correction, which is a generalization of the δ HF correction commonly used in SAPT[58]. Total energies computed with this approach have been found to be quite accurate in comparison with CCSD(T)[58].

SAPT(CCSD) Reference

In order to assess the performance of our hybrid-kernel SAPT(DFT) scheme, we compare the results of several SAPT schemes, using SAPT(CCSD) as the reference for each component. As mentioned above, SAPT(CCSD) results are only available for a limited set of small systems; here we use published SAPT(CCSD)/aug-cc-pVTZ results for a set

of 14 dimers named S2 by Korona[57]. Our comparison includes our implementation of hybrid-kernel SAPT(DFT) in Psi4 and the LHF-orbital SAPT(DFT) as implemented in Molpro[60], both using the aug-cc-pVTZ basis set, and SAPT0 with the aug-cc-pVDZ basis set (SAPT0 has better error cancellation for total interaction energies when used with basis sets of this size [58]). Direct comparison against SAPT0 in the same aug-cc-pVTZ basis is provided in Appendix A for the interested reader.

Also, in order to apply the GRAC scheme, one needs to know the highest occupied orbital eigenvalue and the ionization potential of both monomers in each dimer. In our work, the HOMO eigenvalues are obtained by running a DFT calculation with the plain PBE0 functional and aug-cc-pVTZ basis set, and the ionization potentials for Korona S2 systems are obtained from the original work of Korona[57].

Table 2.1: Mean absolute errors (kcal mol⁻¹) and mean unsigned relative errors (%) of the interaction energy components for the Korona S2 test set with various SAPT methods.

Method ^a	MAE	MURE	Error Distribution ^b					
			4	OB	1	0	1	UB
Electrostatics								
SAPT(DFT) hybrid	0.112	2.39						
SAPT(DFT) LHF	0.114	3.68						
SAPT0	0.520	8.61						
Exchange								
SAPT(DFT) hybrid	0.251	3.38						
SAPT(DFT) LHF	0.258	3.09						
SAPT0	1.757	12.88		█				
Induction								
SAPT(DFT) hybrid	0.148	2.79						
SAPT(DFT) LHF	0.192	2.97						
SAPT0	1.993	16.83		█				
Exchange-Induction								
SAPT(DFT) hybrid	0.144	4.03						
SAPT(DFT) LHF	0.165	4.76						
SAPT0	1.551	26.80		█				
Dispersion								
SAPT(DFT) hybrid	0.175	3.68						
SAPT(DFT) LHF	0.141	2.77						
SAPT(DFT) non-hybrid	0.326	9.58						
SAPT0	0.811	24.86		█				
Exchange-Dispersion								
SAPT(DFT) hybrid	0.062	12.47						
SAPT(DFT) LHF	0.039	3.25						
SAPT0	0.265	36.11						
Total								
SAPT(DFT) hybrid	0.155	4.98						
SAPT(DFT) LHF	0.189	4.17						
SAPT(DFT) non-hybrid	0.244	10.64						
SAPT0	1.237	19.63		█				

Results for the S2 test set are presented in Table 2.1. Both the mean absolute error (MAE) and the mean unsigned error (MURE) with respect to SAPT(CCSD) are presented, because of the existence of strongly interacting systems in S2 (e.g., HF dimer) that might skew the statistics of absolute errors. In addition to the statistics, strip charts are included in the table as a visual representation of errors from all database members. Each vertical line in the chart represents the error (in kcal mol⁻¹) of the SAPT term of interest for a dimer in S2 with respect to SAPT(CCSD)/aug-cc-pVTZ, either on the overbound (−) or the underbound (+) side, and a black rectangular marker (always on the overbound side) is used to indicate the mean absolute error over S2 of the given SAPT term and theory level.

The mean absolute error of the total interaction energy and every SAPT term is below 0.2 kcal mol⁻¹ for the hybrid-kernel SAPT(DFT) and the LHF-orbital SAPT(DFT), with the exception of exchange energies. The mean unsigned relative errors for these two approaches are also below 5% for the total interaction energy and all components, with the exception of the exchange-dispersion term of hybrid-kernel SAPT(DFT), which has a mean unsigned relative error of 12.47%. Nevertheless, because of the small magnitude of the exchange-dispersion term, the mean absolute error of hybrid-kernel SAPT(DFT) for this term remains only 0.062 kcal mol⁻¹, meaning that this error has only a very small effect on the overall dispersion interaction or the total interaction energy.

For the S2 test set, hybrid-kernel SAPT(DFT)/aug-cc-pVTZ and the LHF-orbital SAPT(DFT)/aug-cc-pVTZ show significantly improved accuracy vs. SAPT0/aug-cc-pVDZ, when compared to SAPT(CCSD)/aug-cc-pVTZ benchmark components and total energies. This is consistent with our previous findings for SAPT(DFT)/aug-cc-pVTZ vs SAPT0/aug-cc-pVDZ for total interaction energies for the S22, NBC10, HBC6, and HSG test sets[58]. The mean absolute errors for the exchange, induction, and exchange-induction terms for SAPT0 are larger than 1 kcal mol⁻¹, i.e., larger than “chemical accuracy”. The mean absolute error in the total interaction energy is also slightly over 1 kcal mol⁻¹, which is comparable to its mean absolute errors for some other test sets[58].

The results for dispersion in Table 2.1 show a drawback of what we have labelled the “non-hybrid” SAPT(DFT) approach, i.e., computing the dispersion energy using a hybrid functional and pure ALDA kernel directly (as if one would do with a non-hybrid functional); this approach has a mean absolute error of 0.326 kcal mol⁻¹ and mean unsigned relative error of 9.58% in the dispersion term, which is less satisfactory compared to 0.175 kcal mol⁻¹ and 3.68% for hybrid-kernel SAPT(DFT), and 0.141 kcal mol⁻¹ and 2.77% for LHF SAPT(DFT). From the strip chart, we can observe that all SAPT(DFT) approaches underbind the dispersion interactions in S2, and the “non-hybrid” approach underbinds them to a larger extent. This systematic error introduced by the combination of hybrid xc potential and pure ALDA xc kernel was discussed in Ref. 34, which points out that the hybrid xc potential broadens the occupied-virtual orbital energy gaps and thus lowers the magnitude of dispersion energies. In general, the SAPT(CCSD) results of Korona S2 are fairly accurately reproduced with both SAPT(DFT) approaches that have a proper treatment for the hybrid DFT functional, namely a hybrid ALDA kernel or a LHF variation to the xc potential. The mean absolute error for the dispersion term is roughly doubled for “non-hybrid” SAPT(DFT), although it nevertheless remains modest at a third of one kcal mol⁻¹, and error cancellation for this test set leaves the MAE for total interaction energies only slightly elevated (0.244 kcal mol⁻¹) vs hybrid-kernel SAPT(DFT) and LHF-orbital SAPT(DFT) (0.155 and 0.189 kcal mol⁻¹, respectively). “Non-hybrid” SAPT(DFT) remains a significant improvement over SAPT0/aug-cc-pVDZ for this test set.

For the interested reader, Table A.1 provides a comparison of SAPT2+3(CCD) δ MP2 vs SAPT(CCSD), both in the aug-cc-pVTZ basis, for the Korona S2 test set. Differences between these two high-level SAPT treatments can be taken as a measure of the approximate accuracy of each approach. As mentioned above, SAPT(CCSD) and SAPT2+3(CCD) δ MP2 have accuracy advantages and disadvantages relative to each other. Table A.1 shows that across all energy components, and the total interaction energy, the great majority of the S2 systems show differences of less than 0.3 kcal mol⁻¹, with occasional outliers. Mean abso-

lute deviations between the methods are 0.1–0.2 kcal mol⁻¹ for components, and slightly larger for the overall interaction energy (0.32 kcal mol⁻¹). Compared to these differences, SAPT(DFT) hybrid and SAPT(DFT) LHF are in extremely good agreement with each other for S2, and on average their errors vs SAPT(CCSD) are similar to the differences between SAPT(CCSD) and SAPT2+3(CCD) δ MP2.

SAPT2+3(CCD) δ MP2 Reference

To investigate more completely, we compare to the larger S66 test set[45], here using SAPT2+3(CCD) δ MP2 values as the reference. As before, we compare three approaches to SAPT(DFT), and also the least computationally expensive version of SAPT, SAPT0. We also include the “silver standard” SAPT2+/aug-cc-pVDZ, and “gold standard” SAPT2+(3) δ MP2, which are Pauling points of SAPT theory as shown in Ref. 58. Direct comparisons against SAPT0 and SAPT2+ in the aug-cc-pVTZ basis, which generally provides poorer error cancellation for those levels of SAPT, are provided in Appendix A. The ionization potentials of molecules needed for SAPT(DFT) calculations are computed from the energy of each molecule and its +1 cation, using the PBE0 functional and the def2-TZVPP basis set[61].

Table 2.2: Mean absolute error (kcal mol⁻¹) of the interaction energy for S66 with various SAPT methods.

Method ^a	Total	HB	MX	DD	Error Distribution ^b						
					4	OB	1	0	1	UB	4
Electrostatics											
SAPT(DFT) hybrid	0.374	0.556	0.177	0.311							
SAPT(DFT) LHF	0.423	0.666	0.196	0.319							
SAPT0	0.613	1.034	0.439	0.297							
SAPT2+	0.236	0.270	0.136	0.263							
SAPT2+(3) δ MP2	0.000	0.000	0.000	0.000							
Exchange											
SAPT(DFT) hybrid	0.886	1.127	0.426	0.926							
SAPT(DFT) LHF	0.886	1.121	0.431	0.928							
SAPT0	0.675	0.942	0.263	0.658							
SAPT2+	0.337	0.467	0.222	0.277							
SAPT2+(3) δ MP2	0.000	0.000	0.000	0.000							
Induction											
SAPT(DFT) hybrid	0.211	0.201	0.212	0.220							
SAPT(DFT) LHF	0.224	0.223	0.223	0.225							
SAPT0	0.241	0.200	0.261	0.271							
SAPT2+	0.327	0.384	0.250	0.318							
SAPT2+(3) δ MP2	0.152	0.179	0.121	0.145							
Dispersion											
SAPT(DFT) hybrid	0.370	0.260	0.219	0.573							
SAPT(DFT) LHF	0.308	0.200	0.173	0.499							
SAPT(DFT) non-hybrid	0.635	0.581	0.419	0.822							
SAPT0	0.443	0.862	0.162	0.195							
SAPT2+	0.235	0.397	0.169	0.115							
SAPT2+(3) δ MP2	0.093	0.129	0.056	0.080							
Total											
SAPT(DFT) hybrid	0.334	0.588	0.107	0.217							
SAPT(DFT) LHF	0.234	0.382	0.046	0.199							
SAPT(DFT) non-hybrid	0.604	0.955	0.389	0.385							
SAPT0	0.990	1.197	0.692	0.965							
SAPT2+	0.230	0.235	0.138	0.280							
SAPT2+(3) δ MP2	0.105	0.056	0.082	0.169							

In S66, the dimers are divided into 3 subsets by dominating contributions to the interaction: 23 dimers dominated by electrostatic interactions, typically hydrogen-bonding (HB); 23 dispersion-dominated interactions (DD); and 20 mixed-influence (MX) dimers. Mean absolute errors for energy components and total interaction energies are presented in Table 2.2, for S66 overall and also for each subset (HB, MX, DD). Similarly to Table 2.1, strip charts show error distributions, and in this case, lines for each error are color coded for the dominant interaction type in each dimer: red for HB, green for MX, and blue for DD.

As shown in Table 2.2, the mean absolute errors over S66 for SAPT(DFT) with the PBE0AC functional and the aug-cc-pVTZ basis set are 0.334 (hybrid kernel), 0.234 (LHF orbitals with ALDA kernel), and 0.604 kcal mol⁻¹ (non-hybrid pure ALDA kernel). The close agreement between the hybrid kernel and LHF approaches mimics that seen for S2, and persists for both for mean absolute errors as well as error distributions. The larger error for the non-hybrid approach is also consistent with the results for S2, although the differences are magnified here for the S66 test set, which includes larger molecules. The non-hybrid SAPT(DFT) dispersion is almost always underbound (consistent with the S2 results), whereas the hybrid kernel and LHF approaches are somewhat more balanced in their error distributions. With the exception of the dispersion-dominated complexes, mean absolute errors for dispersion are almost twice as large for non-hybrid SAPT(DFT) vs hybrid kernel or LHF-based SAPT(DFT).

All three SAPT(DFT) approaches considered here provide an improvement in the MAE compared to 0.990 kcal mol⁻¹ for SAPT0/aug-cc-pVDZ. For S66, SAPT0 is nearly always overbound, whereas the behavior of SAPT(DFT) is somewhat more balanced (although the majority of the complexes are underbound). Both the hybrid-kernel and LHF-orbital SAPT(DFT) approaches provide similar MAE's overall and across subsets compared to the computationally expensive SAPT2+/aug-cc-pVDZ approach, which has an MAE across S66 of 0.230 kcal mol⁻¹. However, MAE's for the hybrid-kernel and LHF-

based SAPT(DFT) are somewhat worse than SAPT2+ for the hydrogen-bonded subset, and error distributions across S66 are wider for SAPT(DFT) compared to SAPT2+. Errors for total interaction energies and their components are much smaller for high-level SAPT2+(3) δ MP2/aug-cc-pVTZ, with an overall MAE across S66 of only 0.105 kcal mol⁻¹. Our findings for errors in total interaction energies of S66 for the LHF-orbital SAPT(DFT), SAPT0, SAPT2+, and SAPT2+(3) δ MP2 methods are in qualitative agreement with our previous study of errors in total interaction energies for the S22, NBC10, HBC6, and HSG test sets[58].

Regarding energy components, SAPT(DFT) and SAPT0 exhibit roughly similar error distributions for electrostatics, with hydrogen-bonded systems tending to be overbound, and with dispersion-dominated dimers having their error distribution shifted a little towards the underbound side. Overall SAPT(DFT) is more reliable than SAPT0 on average for electrostatics, especially for H-bonded systems, where there are several significantly overbound systems with SAPT0. For dispersion-dominated complexes, SAPT(DFT) performs similarly to SAPT0 for electrostatics. Errors for induction are quite similar for SAPT0, SAPT(DFT), and SAPT2+. For dispersion energies, SAPT0 tends to underbind hydrogen-bonded complexes (sometimes significantly), and slightly overbinds dispersion-dominated complexes. SAPT(DFT) with the hybrid kernel or LHF orbitals, by contrast, shows some underbound dispersion-dominated complexes and a few overbound H-bonded complexes. On average, hybrid-kernel or LHF-based SAPT(DFT) is more accurate than SAPT0 for dispersion, especially for H-bonded complexes; the errors for the dispersion-dominated subset are slightly larger for SAPT(DFT) than SAPT0 (perhaps due to a favorable error cancellation between the simple treatment of dispersion in SAPT0 and the modest aug-cc-pVDZ basis set used here for SAPT0). As pointed out above, the “non-hybrid” approach to SAPT(DFT) exhibits larger MAE’s for dispersion than hybrid kernel or LHF-based SAPT(DFT), and they are generally worse than SAPT0 except for a slight improvement for the H-bonded subset. For the exchange term, SAPT(DFT) shows a wide

range of errors, spanning the entire ± 1 kcal mol⁻¹ range, with several larger errors on the overbound side for dispersion-dominated dimers, and several larger errors on the underbound side, generally hydrogen-bonded. The SAPT0 error distribution is compressed and shifted towards the overbound side, and it exhibits more strongly overbound outliers (now more frequently of the hydrogen-bonding type). The overall MAE for exchange is somewhat similar for SAPT0 and SAPT(DFT).

In summary, SAPT(DFT) with the PBE0AC functional and the aug-cc-pVTZ basis set performs similarly across total interaction energies and their components whether we use the LHF-orbital formulation or the hybrid kernel, and in general interaction energies and their components are superior to those from SAPT0, except for the exchange component. SAPT(DFT) results for total interaction energies have similar MAE's as the computationally much more expensive SAPT2+ wavefunction-based SAPT, although the error distribution is wider for SAPT(DFT). Similarly, energy components from SAPT(DFT) are often of roughly similar quality as SAPT2+ on average (although larger errors are seen for exchange energies), but the error distributions are wider. Using SAPT(DFT) with the PBE0AC functional but without either the hybrid kernel or an LHF-orbital approach creates larger errors in the dispersion term and the overall interaction energy; this approach remains more accurate on average than SAPT0 but is no longer competitive with SAPT2+ in accuracy.

2.4.3 Timing Performance

In order to investigate the efficiency of our hybrid kernel dispersion algorithm and our overall SAPT(DFT) implementation, we obtained runtimes for the Watson-Crick adenine-thymine complex (WCAT) and the RDX dimer using different numbers of cores (1, 2, 4, and 6) on an Intel Core i7-6800K processor (6 cores, 3.4 GHz) with 128 GB RAM. The geometry of adenine-thymine is obtained from the S22 test set[62] and the RDX dimer from Ref. 49. The aug-cc-pVDZ and aug-cc-pVTZ basis sets are used for both systems. Below, we will also discuss timings for the C₆₀-buckycatcher complex using an aug-cc-pVDZ

basis. The testing systems in this section are shown in Figure 2.4, and the number of basis functions (N_{bf}), occupied orbitals (N_{occ}), virtual orbitals (N_{vir}) and auxiliary functions (N_{aux}) of each combination of dimer system and basis set are listed in Table 2.3.

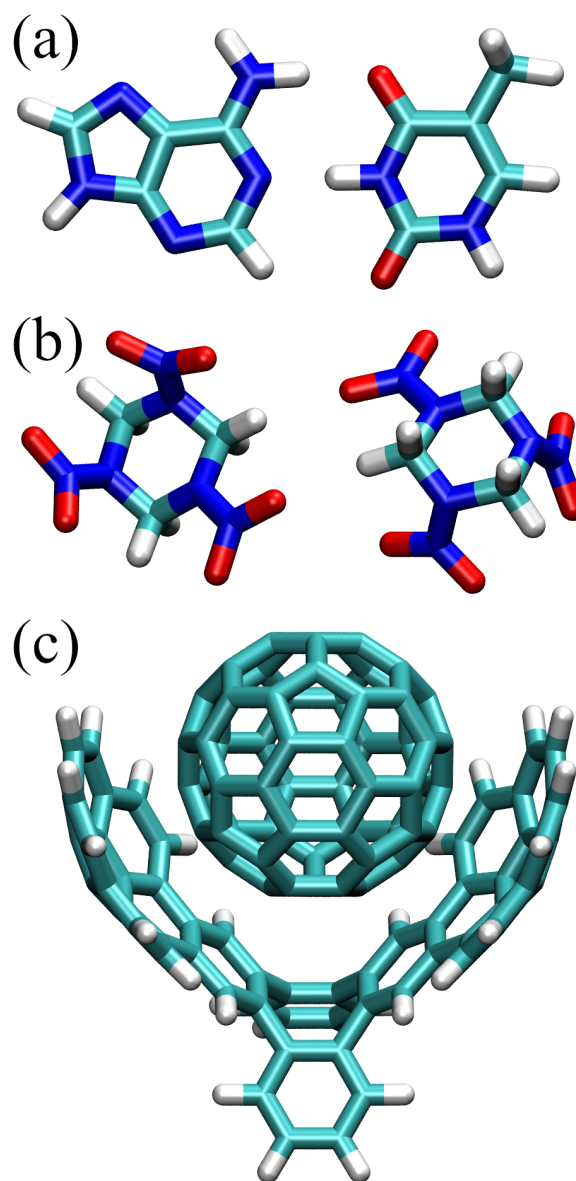


Figure 2.4: Dimer systems tested for program runtime performance: (a) Watson-Crick adenine-thymine complex, (b) RDX dimer and (c) C_{60} -buckycatcher complex.

Table 2.3: Number of basis functions (N_{bf}), occupied orbitals (N_{occ}), virtual orbitals (N_{vir}) and auxiliary functions (N_{aux}) for different systems and basis sets.

System Size	Adenine-Thymine		RDX dimer		Buckycatcher
	aDZ	aTZ	aDZ	aTZ	aDZ
N_{bf}	536	1127	798	1656	3012
$N_{occ,A}$	35	35	57	57	180
$N_{vir,A}$	501	1092	741	1599	2832
$N_{occ,B}$	33	33	57	57	194
$N_{vir,B}$	503	1094	741	1599	2818
N_{aux}	1621	2520	2436	3732	9284

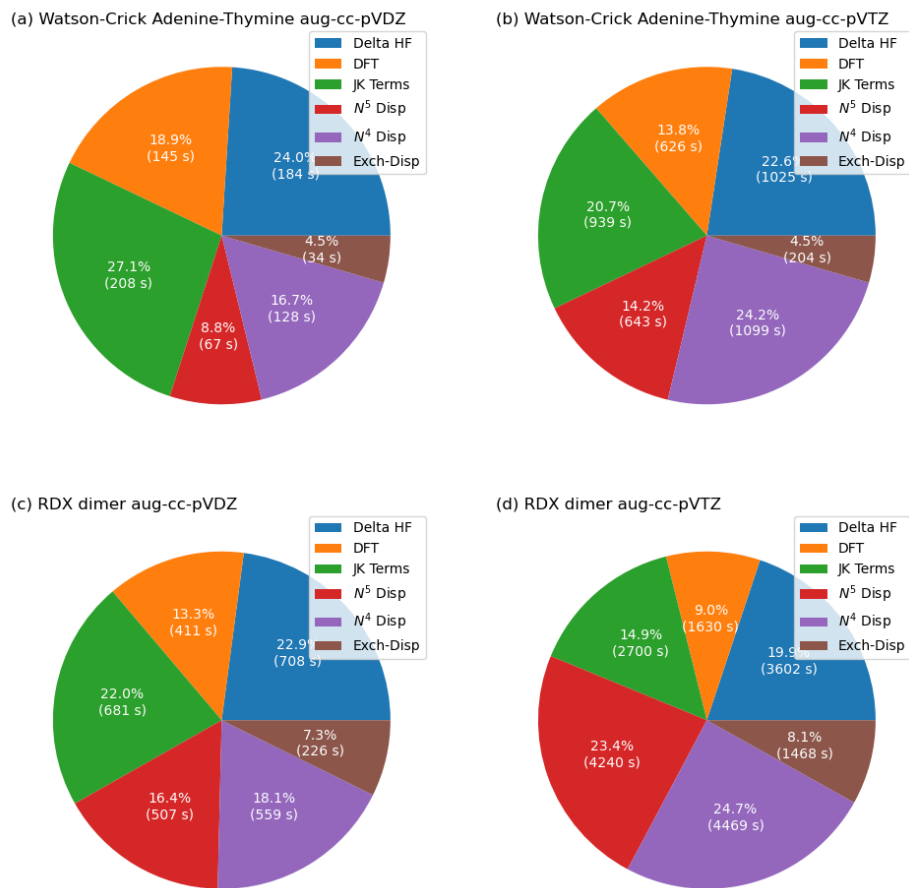


Figure 2.5: Distribution of wall time among subroutines for each test system with aug-cc-pVDZ and aug-cc-pVTZ basis sets with 6 cores.

Timings results of WCAT and RDX dimer are presented in Figure 2.5, showing the the breakdown of the timing data by module for the test systems using 6 cores. The entire SAPT(DFT) computation is divided into 6 modules:

1. “Delta HF” for the computations related to evaluating the δHF term[34], including HF calculations of dimer and monomer, and a SAPT0 calculation of the electrostatics, exchange and induction terms.
2. “DFT” for the DFT calculation of both monomers in order to obtain the Kohn-Sham orbitals.

3. “JK Terms” for the electrostatics, exchange, induction, and exchange-induction terms, all of which computed from certain generalized Coulomb (J) and exchange (K) matrices. Induction and exchange-induction take nearly all of the time for the JK terms (more than 90% for these test cases).
4. “ N^5 Disp” for the $O(N^5)$ steps in the dispersion term, namely the frequency-independent parts of Equation 2.44–Equation 2.48.
5. “ N^4 Disp” for everything in the dispersion term aside from “ N^5 Disp”. This mainly includes the integration over ω as in Equation 2.32, and the integral transformation step which involves the most disk I/O operations.
6. “Exch-Disp” for the exchange-dispersion term as described in subsection 2.3.4. This module also scales as $O(N^5)$ like “ N^5 Disp”.

For our RDX and WCAT test cases, one would hardly claim that the $O(N^5)$ modules contribute dominantly to the total computational time. The “Exch-Disp” module takes up less than 10% of the total wall time, while the percentage of “ N^5 Disp” varies from 8.8% to 23.4% for different system sizes. The timings are distributed somewhat evenly between each module for all test cases; every block, from “Delta HF” to “ N^4 Disp”, takes a considerable portion of the total wall time for these test cases. This suggests that the $O(N^5)$ scaling is not a major concern in SAPT(DFT) calculations of systems below 2000 basis functions; the total computational cost is more affected by iterative steps with lower formal scaling, including SCF calculations, CPKS calculations in the induction terms, and integration over ω . The fraction taken by the “ N^5 Disp” block of the total wall time also indicates the computational cost that could be saved, if one would use the “non-hybrid” approach as indicated in subsection 2.4.2. From the results in subsection 2.4.2 and subsection 2.4.2, the improvement in the accuracies of dispersion energies and total interaction energies introduced the hybrid-kernel algorithm is significant enough to justify the additional computational cost from the “ N^5 Disp” block. It is also interesting to note

that these $O(N^5)$ blocks take a larger fraction of the total job walltime in RDX dimer/aug-cc-pVDZ than in WCAT/aug-cc-pVTZ, even though the former does not have as many basis functions as the latter; this is partly because the detailed scaling of the $O(N^5)$ terms is $O(N_{occ}^2 N_{vir}^2 N_{aux})$, and the number of occupied orbitals for RDX dimer/aug-cc-pVDZ is almost twice of that for WCAT/aug-cc-pVTZ, while N_{vir} and N_{aux} change by a smaller ratio.

Our timings results affirm the utility of the hybrid-kernel algorithm as an alternative to the LHF algorithm, even though the former scales formally as $O(N^5)$ and the latter as $O(N^4)$, because the LHF algorithm will have a much larger prefactor. Although we have not implemented the LHF algorithm ourselves, we can obtain a more detailed comparison by performing test computations with the current hybrid kernel algorithm and the LHF algorithm implemented in the Molpro program package[60]. We present the results of this comparison for RDX dimer in the aug-cc-pVTZ basis in Table 2.4. Here, the LHF algorithm takes 12.80 hours with 6 cores, while the hybrid algorithm implemented in this work only takes a total walltime of 5.03 hours. The DFT calculation with the LHF algorithm takes 2.29 hours, which is about $5\times$ slower than the hybrid algorithm, where a regular DFT calculation without LHF approximation is performed. The regular DFT calculation took 13 iterations to converge for both monomers, while the LHF-DFT calculation took 19 and 43 iterations respectively, and this implies that the LHF approach might present some hindrance to the convergence of the SCF procedure. Also, the Molpro program has not implemented a 2-index representation of the xc kernel as of version 2019.2 tested here, and the formation of the xc kernel costs a significant amount of time with the 3-index representation. The time integration part involves contractions between the xc kernel and other tensors, so it is also affected by the 3-index representation of the kernel. For the subroutines that are exclusive to the hybrid kernel algorithm, including the $O(N^5)$ part, the total wall time is only 2.35 hours, only slightly longer than the cost introduced in DFT by the LHF approximation, so we may conclude that even if we do not consider the difference between

2-index and 3-index representation of the xc kernel, the $O(N^5)$ hybrid kernel algorithm would have an advantage for systems around the size of RDX dimer with the aug-cc-pVTZ basis, or smaller.

Table 2.4: Wall times (in hours) for SAPT(DFT) computations of RDX dimer/aug-cc-pVTZ with hybrid and LHF algorithm.

Subroutine	Hybrid	LHF
Delta HF	0.96	N/A ¹
DFT	0.45	2.29
xc kernel	0.08	4.17
FDDS object ²	2.35	N/A
Disp time integration	0.37	3.59
Exch-disp	0.41	1.99
Total	5.03	12.80

Table 2.5: Wall times (in hours) for PBE0AC SAPT(DFT) computations of the C₆₀-buckycatcher complex using 18 cores of an Intel i9-10980XE processor with hybrid algorithm.

Subroutine	Wall Time
Delta HF	29.1
Dimer HF	6.3
C60 HF	6.2
Buckycatcher HF	6.6
Prepare JK	0.5
Exchange	0.5
Induction	8.9
DFT	14.8
C60 DFT	7.1
Buckycatcher DFT	7.7
JK Terms	10.0
Prepare JK	0.5
Exchange	0.5
Induction	8.9
Dispersion	42.7
Transformation	10.5
QR Factorization	0.5
Form X	7.0
Form Y	13.1
Time integration	4.3
Exchange-dispersion	6.8

We also performed PBE0AC SAPT(DFT) computations with the hybrid kernel on the C₆₀-buckcatcher complex using the aug-cc-pVDZ basis set. The numbers of occupied and virtual orbitals, etc., are listed in Table 2.3 along with the previous test systems. The geometry of the complex was taken from Ref. 63 (complex C60@2). Because of the large size of the system, we used a more powerful computer for our timings tests, namely, an 18-core Intel Core i9-10980XE processor at 3.0 GHz, with 256 GB of RAM and a scratch disk array of three 7200 rpm disk drives in RAID0 configuration. The wall time of the entire calculation was 4.03 days, and the detailed timing information is shown in Table 2.5. For this system with 3012 basis functions, the $O(N^5)$ contributions to the dispersion term become more significant than in the previous test cases, and overall the dispersion component is now the most time-consuming step (although followed closely by the time required to compute δ_{HF}).

The integral transformation procedure in the dispersion term is quite expensive, comparable to the $O(N^5)$ terms, and this can be attributed to the disk operation required for writing large 3-index integrals of form $(rr'|Q)$ which are later used to reform the 4-index MO integral of form $(aa'|rr')$ as in Equation 2.44–Equation 2.48.

In fact, this calculation has also been performed in Ref. 64 with a non-hybrid DFT functional (HCTH407) and pure ALDA kernel, which allows the dispersion term to scale as $O(N^4)$ in contrast to the case of hybrid xc-kernel of $O(N^5)$. That work accomplished the same calculation with less computational cost than that reported here, because of the avoidance of the $O(N^5)$ terms with the non-hybrid functional (and likely also omitting the δ_{HF} step). Using a non-hybrid functional is an effective approach when trying to perform SAPT(DFT) calculations for large systems with limited computation resources, but our computation demonstrates that even the hybrid xc-kernel variant of SAPT(DFT) is now able to handle systems with around 3000 basis functions.

2.5 Conclusions

We have reported an implementation of symmetry-adapted perturbation theory based on a density functional theory description of the monomers, i.e., SAPT(DFT)[30, 34, 49], in the PSI4 open-source quantum chemistry program[48]. Hybrid functionals have become preferred for applications of SAPT(DFT), especially the PBE0 hybrid functional (with an asymptotic correction term to achieve correct long-range behavior of the potential)[19, 57]. However, the use of hybrid functionals complicates the dispersion and exchange-dispersion terms, requiring either computational steps that scale as $O(N^5)$ [compared to $O(N^4)$ without the use of a hybrid kernel for dispersion], or else the construction of a local representation of the Hartree-Fock potential (LHF) that can then be used with a simpler ALDA kernel in the treatment of dispersion. Although the latter choice formally scales as only $O(N^4)$, in practice the LHF equations can be hard to converge and thus may require substantial time. Here, we have implemented an $O(N^5)$ algorithm allowing the hybrid kernel to be used for dispersion, based on the algorithm of Bukowski et al.[36]

We have improved this algorithm by using a 2-index representation of the exchange-correlation kernel as proposed by Pitoňák and Hesselmann[39], and by improving the numerical stability replacing the “projector” in Bukowski’s work (Ref. 36) with a pseudoinverse operation based on QR factorization. We have also optimized the tensor contraction procedures to minimize disk I/O, which affects the efficiency of the algorithm heavily as the system size increases.

Our algorithm scales as $O(N^5)$ formally in the dispersion and exchange-dispersion term, but in practice, the iterative $O(N^4)$ induction term usually contributes a non-negligible or even dominating portion to the total computational cost, especially for small or medium-sized systems with less than 2000 basis functions. Timings of each step in the algorithm justify our choice of the SAPT(DFT) algorithm based on hybrid xc-kernel over the LHF approach, because in most systems that are small enough to be computed with SAPT(DFT),

the prefactor is shown to have more influence to the total computational cost than the formal scaling.

Using the new code, we examined the accuracy of SAPT(DFT) using the hybrid kernel for dispersion, comparing to the LHF-based treatment and also to results obtained using PBE0AC with neither LHF orbitals nor a hybrid kernel for dispersion. The latter approach is not as accurate as the former two, but LHF-based and hybrid-kernel-based SAPT(DFT) give very similar results, once we reformulate the scaling factor used to estimate the coupled exchange-dispersion energy from the uncoupled exchange-dispersion energy. The appropriate scaling factor is shown here to be heavily dependent of whether the DFT algorithm used to generate the molecular orbitals adopts the LHF approximation. Based on results for diverse non-covalent interactions in the S66 test set, the SAPT(DFT) results are generally more accurate than their SAPT0 counterparts, with the exception of the exchange component. The mean absolute error of SAPT(DFT) is comparable to that of SAPT2+, which scales as $O(N^7)$ as opposed to $O(N^5)$ for hybrid-kernel SAPT(DFT), for the total interaction energy and all components except for exchange, although the error distributions are wider for SAPT(DFT).

CHAPTER 3
ASSESSMENT OF THREE-BODY DISPERSION MODELS AGAINST
COUPLED-CLUSTER BENCHMARKS FOR CRYSTALLINE BENZENE,
CARBON DIOXIDE, AND TRIAZINE

3.1 Abstract

To study the contribution of three-body dispersion to crystal lattice energies, we compute the three-body contributions to the lattice energies for crystalline benzene, carbon dioxide, and triazine using various computational methods. We show that these contributions converge quickly as the intermolecular distances between the monomers grow. In particular, the smallest value among the three pairwise intermonomer closest-contact distances, R_{\min} , shows strong correlation with the three-body contribution to lattice energy, and the largest of the closest-contact distances, R_{\max} , serves as a cutoff criterion to limit the number of trimers to be considered. We considered all trimers up to $R_{\max} = 15 \text{ \AA}$. The trimers with $R_{\min} < 4 \text{ \AA}$ contribute 90.4%, 90.6%, and 93.9% of the total three-body contributions for crystalline benzene, carbon dioxide, and triazine, respectively, for the coupled-cluster singles, doubles, and perturbative triples [CCSD(T)] method. For trimers with $R_{\min} > 4 \text{ \AA}$, the second-order Møller-Plesset perturbation theory (MP2) complemented with the Axilrod–Teller–Muto (ATM) three-body dispersion correction reproduces the CCSD(T) values for the cumulative three-body contributions with error of less than 0.1 kJ mol^{-1} . Moreover, the three-body dispersion converges by $R_{\max} = 10 \text{ \AA}$. From these results, it appears that in molecular crystals where dispersion dominates the three-body contribution to the lattice energy, the trimers with $R_{\min} > 4 \text{ \AA}$ can be computed with the MP2+ATM method to reduce the computational cost, and those with $R_{\max} > 10 \text{ \AA}$ appear to be essentially negligible.

3.2 Introduction

The many-body expansion (MBE) is a widely used computational method for computing the interaction energies of non-covalent molecular aggregates, such as molecular clusters and molecular crystals[1, 2]. The MBE expresses the interaction energy as the sum of n -body ($n = 2, 3, 4, \dots$) terms, each of which involves interactions between n molecules simultaneously. Because the MBE series converges quickly as the number of molecules involved n increases, in approximate computations it may be truncated at low order. The simplest MBE approach would be to truncate the series at $n = 2$, i.e. approximate the total interaction energy of the many-body system with the sum of all pairwise interactions. Such an approximation benefits from its low computational cost, which stems on the relatively modest number of possible dimer combinations, $\frac{N(N-1)}{2}$, as opposed to $2^N - 1$ for the full many-body expansion, where N is the total number of molecules in the system. However, for several instances such as crystalline benzene[65, 66] and water clusters[67], the many-body ($n \geq 3$) effect can contribute 10%–20% to the total interaction energy of the system and is thus not negligible. Such examples point to the importance of an effective method to compute many-body interaction energies, especially the three-body ones, which make up the major contribution of many-body interaction energies.

In 2015, Beran and coworkers constructed the 3B-69 benchmark set, which consists of the three-body interaction energies of 69 trimers with their geometries extracted from 23 different molecular crystals[68], filling the vacancy of a benchmark data set for three-body interactions. These workers demonstrated the crucial fact that DFT-D3 does not perform as well for the nonadditive three-body contribution to interaction energies as it does to two-body contributions, mainly because of the delocalization error which prevents DFT from predicting the three-body polarization energies correctly. This work has also shown that the popular exchange functionals seem to have difficulty describing three-body exchange effects. For the wavefunction methods, they recommended MP2.5 (average of MP2

and MP3 energies) [4] and spin-component scaled CCSD[5] for noncovalent interactions [SCS(MI)-CCSD][6] for computing three-body interaction energies, but both of them scale as $O(N^6)$, restricting their usefulness for important practical applications like computing the lattice energies of molecular crystals. They have also used an *ab initio* force field[66, 69] to estimate the polarization and dispersion contribution to the three-body interaction energy, with the latter based on the Axilrod–Teller–Muto (ATM) formula[70, 71]. From these results, they reconfirmed that MP2 is a good approximation to three-body polarization effects, but it lacks three-body dispersion.

Besides the wavefunction and DFT supermolecular approaches, an alternative approach to model three-body interactions was introduced by Podaszwa and Szalewicz in 2007[72]. In this approach, the symmetry-adapted perturbation theory based on density functional theory [SAPT(DFT)][30, 34] was generalized to three-body interactions. In addition to demonstrating how to express several of the components of the three-body interaction in the SAPT(DFT) framework, they also proposed a hybrid SAPT/supermolecular model that they called MP2+SDFT, which adds the third-order nonadditive three-body dispersion energy from the coupled Kohn-Sham (CKS) frequency-dependent density susceptibility (FDDS), denoted as $E_{\text{disp}}^{(3)}(\text{CKS})$, to the supermolecular MP2 interaction energy. This model is inspired by the fact that the supermolecular MP2 intrinsically contains two-body and three-body interactions with a partial accounting of electron correlation, but it misses three-body dispersion. While the MP2+SDFT model has a low scaling of $O(N^5)$, their results seem to show that the $E_{\text{disp}}^{(3)}(\text{CKS})$ correction might not be an ideal description of the interactions missing in the supermolecular MP2 approach. This model obtains accurate interaction energies for helium trimer and water trimer, but the results are less accurate for argon trimer and benzene trimer, especially at closer intermolecular distances. Such contrasting results between different systems implies the possibility that the MP2+SDFT model could be less promising for trimer systems with greater dispersion effects.

In 2015, Huang and Beran attempted to replace the CKS dispersion in the MP2+SDFT

model of Podeszwa and Szalewicz with a damped ATM dispersion term, and added it to the supermolecular MP2 three-body interaction energy[73]. This new model with ATM dispersion is called MP2+ATM in their paper. They have shown that MP2+SDFT model (or, as Huang and Beran refer to it, MP2+CKS) overestimates the repulsive nonadditive three-body interaction energy, and they have attributed this discrepancy to some missed higher-order attractive exchange terms in this model. On the other hand, the ATM dispersion is effectively the triple-dipole term of the multipole expansion of the three-body CKS dispersion[74]. The three-body dispersion energy becomes less repulsive by dropping out terms with quadrupoles or higher, and its magnitude is further diminished by the empirical damping. As a result of fortuitous error cancellation, the MP2+ATM model provides much better agreement with respect to CCSD(T) than MP2+CKS for various systems including 3B-69[73]. The potential energy surface of pyrazole trimer also shows that the error cancellation behaves consistently well along different intermolecular distances. In the end of their work, they suggested that MP2+ATM would be an effective model for treating three-body intermolecular interactions. This study also examined the MP2+ATM model for 65 symmetry-unique trimers in crystalline benzene, and it indicated that MP2+ATM is promising, with a small error of 0.18 kcal/mol for the three-body contribution to the crystal lattice energy. Nevertheless, an in-depth analysis of the effectiveness of MP2+ATM, MP2+CKS and other computational methods over trimers of different intermolecular distances and geometric configurations still remains lacking.

In this work, we provide a more thorough assessment of several approximate methods for computing the three-body contributions to the crystal lattice energy of small organic molecules expected to feature significant three-body dispersion effects. These approximate methods include CCSD(T), MP2+ATM, MP2+CKS, MP2.5 and SCS(MI)-CCSD. To assess these methods, we obtain benchmark-quality CCSD(T) three-body interaction energies for a large number of trimers in the crystal, up to 15 Angstrom cutoff for the closest contact distance between monomers. This includes 1977, 1948, and 750 trimers for the

benzene, carbon dioxide, and triazine crystals, respectively. Since the interaction energies of all significant trimers within the crystal system will be computed, we are able to analyze the contribution to the three-body lattice energy for various geometrical subsets of the trimer set within each crystal based on intermolecular distances between monomers. From this analysis, we reveal the fact that the trimers with at least two monomers with close intermolecular distance contributes the vast majority of the three-body lattice energies, and we are able to save plenty of computational resource by ignoring the trimers with monomers far apart from each other, or use a cheaper computational method to compute their contributions.

3.3 Theory and Method

3.3.1 Axilrod–Teller–Muto three-body dispersion

The three-body dispersion energy of a trimer can be approximated as a summation over triples of atoms in the system, using the Axilrod–Teller–Muto formula for three-body triple-dipole dispersion[70, 71]:

$$E_{ATM}^{abc} = C_9^{abc} \frac{1 + 3\cos\theta_a\cos\theta_b\cos\theta_c}{(R_{ab}R_{bc}R_{ca})^3}, \quad (3.1)$$

where R_{ab} is the distance between atoms a and b (and similarly for R_{bc} and R_{ca} ; θ_a , θ_b , and θ_c are the angles of the triangle formed by the three atoms, each symbol representing the angle with the corresponding atom as the vertex. C_9^{abc} is the dispersion coefficient for the atom triplet abc , and can be obtained from the frequency-dependent dipole polarizabilities of the atoms:

$$C_9^{abc} = \frac{3}{\pi} \int_0^\infty d\omega \alpha^a(i\omega)\alpha^b(i\omega)\alpha^c(i\omega). \quad (3.2)$$

In practice, the C_9^{abc} coefficient can be approximated by a geometric mean of two-body

C_6 coefficients:

$$C_9^{abc} \approx \sqrt{C_6^{ab} C_6^{bc} C_6^{ca}}, \quad (3.3)$$

and in this work, we utilize the C_6 coefficients from the DFT-D4 program of Grimme and coworkers[8, 75, 76], which are based on interpolations of tabulated atomic imaginary frequency-dependent polarizabilities, using information for each atom’s chemical environment.

The total ATM three-body dispersion energy of trimer ABC is obtained by summing E_{ATM}^{abc} over all atom triplets from the trimer, in which one atom is on each monomer (terms with two or more atoms on each monomer would contribute to dimer or monomer energies and thus cancel out when computing the nonadditive three-body energy):

$$E_{ATM} = \sum_{a \in A} \sum_{b \in B} \sum_{c \in C} f^{(9)} E_{ATM}^{abc}, \quad (3.4)$$

where $f^{(9)}$ is an empirical damping function that damps the ATM dispersion energy at short interatomic distances. In this work, we implement two different damping functions that are previously mentioned in other studies. In the work of Beran and coworkers on three-body interactions for 3B-69 and other systems[68, 73], they wrote the damping function as a product of three two-body Tang–Toennies (TT) damping functions[77, 78]:

$$f_9^{abc}(\beta) = f_6^{ab}(R_{ab}, \beta) f_6^{ac}(R_{ab}, \beta) f_6^{ca}(R_{ab}, \beta), \quad (3.5)$$

where the two-body damping function $f_6(R, \beta)$ is given as

$$f_6(R, \beta) = 1 - \sum_{k=0}^6 \left(\frac{(\beta R)^k}{k!} \right) e^{-\beta R}, \quad (3.6)$$

β is an empirical parameter which depends on the van der Waals radii r^{vdW} of the atoms

involved in $f_6(R, \beta)$ [77]:

$$\beta = -0.31(r_a^{vdW} + r_b^{vdW}) + 3.43[\text{bohr}^{-1}], \quad (3.7)$$

and the values of r^{vdW} are taken from the representative CCSD van der Waals radii, which are 2.63, 3.34, 3.18 and 3.07 bohr for hydrogen, carbon, nitrogen and oxygen respectively[77].

Another form of damping function, employed in the DFT-D4 program package, uses a zero-damping scheme proposed by Chai and Head-Gordon (CHG)[79]:

$$f_{damp}^{(9)}(\bar{R}_{abc}) = \frac{1}{1 + 6(\bar{R}_{abc})^{-16}}, \quad (3.8)$$

where \bar{R}_{abc} is a measure of the average interatomic distance:

$$\bar{R}_{abc} = (R_{ab}R_{bc}R_{ca}/R_{0,BJ}^{ab}R_{0,BJ}^{ac}R_{0,BJ}^{ca})^{1/3}. \quad (3.9)$$

In this damping scheme, the quantity $R_{0,BJ}^{ab}$ is defined as it is in the Becke-Johnson (BJ) damping function, i.e.[80],

$$R_{0,BJ}^{ab} = a_1 R_0^{ab} + a_2, \quad (3.10)$$

where the R_0^{ab} is the cutoff distance of each atom pair

$$R_0^{ab} = \sqrt{\frac{C_8^{ab}}{C_6^{ab}}}, \quad (3.11)$$

and the parameters a_1 and a_2 are dependent on the density functional chosen for a DFT-D calculation. In our work, we use the values for Hartree–Fock, which are $a_1 = 0.4496$ and $a_2 = 3.3574$.

3.3.2 Three-body CKS FDDS dispersion

An alternative way to compute the three-body interaction energy arises from the third-order dispersion energy in SAPT(DFT). In two-body SAPT(DFT), the leading contribution of the dispersion energy is of the second order, which corresponds to the product of the FDDS's of two monomers. Using the Casimir-Polder identity, the two-body dispersion energy can be written as an integration over frequency, ω , of the FDDS product[52, 53]:

$$E_{disp}^{(2)} = -\frac{1}{2\pi} \int_0^\infty d\omega \int d\mathbf{r}_A d\mathbf{r}'_A d\mathbf{r}_B d\mathbf{r}'_B \frac{1}{|\mathbf{r}_A - \mathbf{r}_B|} \frac{1}{|\mathbf{r}'_A - \mathbf{r}'_B|} \chi^A(\mathbf{r}_A, \mathbf{r}'_A | i\omega) \chi^B(\mathbf{r}_B, \mathbf{r}'_B | i\omega), \quad (3.12)$$

and transforming the FDDS in the position space into the density-fitting auxiliary basis representation yields[39]

$$E_{disp}^{(2)} = -\frac{1}{2\pi} \int_0^\infty d\omega \text{Tr} (\mathbf{S}^{-1} \boldsymbol{\chi}^A \mathbf{S}^{-1} \boldsymbol{\chi}^B), \quad (3.13)$$

where \mathbf{S} is the Coulomb metric in the auxiliary basis set:

$$\mathbf{S}_{PQ} = (P | \frac{1}{r_{12}} | Q). \quad (3.14)$$

As discussed in Ref. 30, the coupled FDDS needs to be computed rather than the uncoupled one, in order to obtain accurate dispersion energies. The coupled FDDS can be solved with the time-dependent coupled Kohn-Sham (TD-CKS) theory[30]. We recently reported an improved algorithm to compute the dispersion contribution in SAPT(DFT) using hybrid kernels, based on a QR factorization of certain intermediates and using a density-fitting representation of the FDDS and other intermediate quantities. Further details are provided in Ref. 81.

For the three-body case, the leading contribution of the nonadditive three-body dispersion energy is of the third order. The formula of three-body $E_{disp}^{(3)}$ is similar to that of

two-body $E_{disp}^{(2)}$ [72]:

$$E_{disp}^{(3)} = -\frac{1}{\pi} \int_0^\infty d\omega \int d\mathbf{r}_A d\mathbf{r}'_A d\mathbf{r}_B d\mathbf{r}'_B d\mathbf{r}_C d\mathbf{r}'_C \frac{1}{|\mathbf{r}_A - \mathbf{r}_B|} \frac{1}{|\mathbf{r}'_A - \mathbf{r}_C|} \frac{1}{|\mathbf{r}'_B - \mathbf{r}'_C|} \chi^A(\mathbf{r}_A, \mathbf{r}'_A | i\omega) \chi^B(\mathbf{r}_B, \mathbf{r}'_B | i\omega) \chi^C(\mathbf{r}_C, \mathbf{r}'_C | i\omega), \quad (3.15)$$

or in the auxiliary basis representation[73]:

$$E_{disp}^{(3)} = -\frac{1}{\pi} \int_0^\infty d\omega \text{Tr} (\mathbf{S}^{-1} \boldsymbol{\chi}^A \mathbf{S}^{-1} \boldsymbol{\chi}^B \mathbf{S}^{-1} \boldsymbol{\chi}^C). \quad (3.16)$$

3.3.3 Three-body crystal lattice energies

In this work, we investigate the three-body contribution to the lattice energy of crystalline benzene, carbon dioxide, and triazine. The crystal structures are obtained from the Cambridge Structural Database (CSD)[82], and we have used the CrystaLattE program package of Borca et al.[83] to generate sets of trimer geometries from the CIF files for each crystal structure. The CrystaLattE program generates symmetry-unique trimers, and for each it also determines the number of symmetry-equivalent replicas \mathcal{R}_M in the crystal. The contribution (per monomer) of the symmetry-unique trimer M to the total three-body lattice energy \mathcal{C}_M is thus computed as

$$\mathcal{C}_M = \mathcal{R}_M \times \frac{\Delta E_M^{int,3}}{3}, \quad (3.17)$$

where $\Delta E_M^{int,3}$ is the nonadditive three-body interaction energy of trimer M .

We compute the $\Delta E_M^{int,3}$ for each trimer with various methods, including CCSD(T), MP2, MP2.5, SCS(MI)-CCSD. We also employ the MP2+ATM and MP2+CKS dispersion correction schemes in addition to these traditional wavefunction methods, where the ATM dispersion term is computed both undamped or damped (with either TT or CHG as the damping function). The MP2 interaction energy is computed by performing a two-point

CBS extrapolation[84] for the MP2 correlation energy using aug-cc-pVTZ and aug-cc-pVQZ basis sets. The Hartree–Fock reference part of the MP2 interaction energy is computed with the aug-cc-pVQZ basis set. For the purpose of readability, in the rest of the paper, we will refer this scheme for computing MP2 interaction energy as MP2/CBS(a[TQ]Z).

For other wavefunction methods, a focal point approach, in which the interaction energy is approximated by adding to the MP2/CBS(a[TQ]Z) interaction energy a correction for higher-order electron correlation, computed as the difference between a higher-level method and MP2, using a relatively small basis set, aug-cc-pVDZ in this work[85, 86]. By employing the focal point approach, one avoids expensive computations with high-level theory like CCSD(T) with a large basis set. For example, the CCSD(T) interaction energy is approximated by

$$E(\text{CCSD(T)}) \approx E(\text{MP2/CBS}) + \delta_{\text{MP2}}^{\text{CCSD(T)}/\text{aDZ}}, \quad (3.18)$$

where the difference between CCSD(T) and MP2 energies is computed under the aug-cc-pVDZ basis set:

$$\delta_{\text{MP2}}^{\text{CCSD(T)}/\text{aDZ}} = E(\text{CCSD(T)/aDZ}) - E(\text{MP2/aDZ}). \quad (3.19)$$

The focal point approach exploits the fact that higher-order correlation effects beyond MP2 are usually captured adequately in smaller basis sets. The interaction energies for MP2.5 and SCS(MI)-CCSD can be computed in a similar way. In the rest of the paper, we will use a shorthand notation for such focal point schemes for convenience; the CCSD(T) interaction energy computed from the focal point approach as shown above will be represented as CCSD(T)/CBS(a[TQ]Z; δ :aDZ), and other methods can be abbreviated similarly.

When computing the crystal lattice energy using the many-body expansion, an infinite number of n -mers could be generated due to the periodic nature of the system. Therefore, one needs to apply a cutoff criterion based on intermolecular separations, assuming

that the interaction energies for n -mers will decay reasonably fast as the molecules grow further apart, as should be the case for molecular crystals. In this work, we follow some definitions and procedures from Ref. 83. First, the *closest-contact separation* for dimer is defined as the minimum interatomic distance between two atoms, one of which on each monomer. Second, the trimer cutoff criterions compute the longest of the three pairwise closest-contact separations within a trimer and ensures that it is shorter than a given cutoff distance. In this work we will apply a trimer cutoff of 15 Å for the trimers considered in the computation of crystal lattice energies. For convenience, we will use R_{\max} to represent the largest of the closest separations between the three pairs of monomers in a trimer, and we also define R_{\min} as the smallest of the three closest-contact separations. To describe the spatial arrangement of the trimer, we also define θ_{\max} of trimer as the largest angle of the triangle formed by centers of mass (COMs) of its three monomers.

3.4 Results and Discussions

For each crystal (benzene, carbon dioxide and triazine), we generated a single set of trimers consistent with a “trimer cutoff” of 15 Å. We will analyze the crystal lattice energy from various subsets based on geometrical parameters defined in subsection 3.3.3. By evaluating the contribution to the three-body lattice energies for different subsets, we can study how the energies depend on the geometrical parameters of the trimers involved. For example, the three-body lattice energies for different trimer cutoff thresholds could teach us how the lattice energy accumulates as trimers with greater intermolecular separations are taken account into the computation. We will be using R_{\min} , R_{\max} and θ_{\max} to determine the trimer subsets and investigate how the three-body lattice energy depends on them.

3.4.1 Dependence of energies on the minimum intermonomer distance, R_{\min}

We first look at how the three-body lattice energy grows as the R_{\min} cutoff threshold increases. In Figure 3.1–Figure 3.3, the accumulative three-body lattice energy is plotted

against the R_{\min} cutoff value, for which any trimers with R_{\min} greater than the cutoff are ignored. Each curve corresponds to a level of theory introduced in subsection 3.3.3, where shorthand notations are used to represent different damping schemes for the ATM dispersion correction in the MP2+ATM method: (u) for undamped, (TT) for the Tang–Toennies damping function[77, 78], and (CHG) for the Chai–Head-Gordon damping function [79]. From these graphs, we observe a few trends among the three molecular crystals.

For all of these crystals, the trimers with R_{\min} less than 4 Å contribute most of the three-body lattice energies, for all methods involved, and the cumulative lattice energies converge quickly as the R_{\min} cutoff increases. MP2, which lacks three-body dispersion effects, only accounts for a very small portion of the true three-body contribution to the lattice energy, especially for crystalline benzene, as it only captures 14% of the reference value from CCSD(T)/CBS(a[TQ]Z; δ :aDZ). This indicates the importance of three-body dispersion for the lattice energies of the crystals studied in this work. The CKS or undamped ATM dispersion corrections are shown to significantly overestimate the three-body dispersion for all three systems, and the damping of ATM dispersion results in fortuitous but consistent error cancellation, which agrees with the conclusion of Huang and Beran[73]. The SCS(MI)-CCSD lattice energies match the CCSD(T) references very well for the three crystals studied, proving that it is effective as an alternative to CCSD(T) for studying three-body interactions, not only for gas-phase trimers at equilibrium distance, as shown in the 3B-69 benchmark study[68], but also for molecular crystals. On the other hand, the MP2.5 method, which performs well for the 3B-69 systems, lacks consistency in predicting the three-body lattice energies accurately; the MP2.5 three-body lattice energy for crystalline benzene reproduces the CCSD(T) result well, but it overestimates the three-body contribution to the lattice energy for crystalline triazine and underestimates it for crystalline carbon dioxide. It appears that the MP3 scaling factor of 0.5 in the MP2.5 approach is only good for trimers at near-equilibrium intermolecular distance and it may be less robust for condensed phase systems like crystals.

It is also worth mentioning that while Huang and Beran have stated that the ATM formula underestimates the CKS dispersion in Ref. 73, the results for carbon dioxide crystal show the opposite, with the value of ATM dispersion being slightly greater than that of CKS dispersion. As pointed out by Huang and Beran, the damping function for the ATM model partially cancels the error of CKS dispersion due to ignoring higher-order exchange and correlation terms. From our results, the Tang–Toennies damping function damps the ATM dispersion more heavily than the Chai–Head-Gordon damping function, and produces more accurate three-body lattice energy as a result of better error cancellation. MP2+ATM(TT) and MP2.5 exhibit similar errors versus CCSD(T) for crystalline carbon dioxide, and MP2+ATM(TT) is even slightly more accurate than MP2.5 for crystalline triazine. Given the cheap computational cost of the ATM dispersion correction, the MP2+ATM approach with the Tang–Toennies damping function seems to be a good approximation to CCSD(T) for computing three-body contributions to crystal lattice energies.

In Table 3.1–Table 3.3, the three-body lattice energy contributions for each R_{\min} domain are presented for each computational method. The trimers within each crystal structure are split into three domains, or subsets, based on their R_{\min} values: short- ($R_{\min} \leq 4 \text{ \AA}$), medium- ($4 \text{ \AA} < R_{\min} \leq 7 \text{ \AA}$), and long-range ($7 \text{ \AA} < R_{\min} \leq 15 \text{ \AA}$). In these tables, we also list the percentage contributions of each subset to the total three-body lattice energy for each method. For most computational methods in all three crystals, the short-range subset accounts for more than 90% of the three-body lattice energies, with less than 30% of the number of symmetry-unique trimers considered. On the contrary, the long-range subset only contributes 1%–2% of the total three-body lattice energy. We have also listed the errors of the subset contributions with respect to the CCSD(T)/CBS reference values for each method in the parentheses. From these errors, one can conclude that any method that involves proper treatment of three-body dispersion effects, i.e. any method except for MP2, has its error almost completely in the short-range domain. For each method except for MP2 and for all three crystal systems, the total error in the medium- and long-range

is less than 0.1 kJ mol^{-1} . From the results above, we can conclude that the three-body dispersion effect at medium- and long-range, while being less significant in its magnitude, can be accurately modeled by any of the approximate methods studied in this work (except for MP2), including direct dispersion corrections like ATM and CKS, and wavefunction methods like MP2.5 and SCS(MI)-CCSD. This fact agrees with the comments on CKS dispersion correction by Huang and Beran[73], that the discrepancy between MP2+CKS and CCSD(T) for three-body interaction energies is because the MP2+CKS model lacks higher-order exchange terms. For trimers with $R_{\min} > 4$, the molecules are apparently far apart enough from each other for any exchange-repulsion effects to vanish. Therefore, the CKS dispersion term, as well as ATM, which is an approximation to it, describes the three-body dispersion effect very accurately at long-range where exchange-repulsion effects do not exist. The percentages and errors of three-body lattice energy contributions in different ranges of R_{\min} also suggest that it is sufficient to perform CCSD(T) calculations only for the trimers in the short-range domain, and compute the contribution in the medium- and long-range domain with a cheaper approximate method such as MP2+CKS or MP2+ATM, while still obtaining very high-accuracy three-body lattice energies with less than 0.1 kJ mol^{-1} error compared to computing all trimers with CCSD(T), allowing one to avoid more than 70% of the expensive CCSD(T) computations that are not necessary in order to obtain high-quality lattice energies. Even larger savings may be obtained by adding an additional geometric closeness constraint on the trimers to be computed by CCSD(T): we may also require that the largest of the closest contact distances between the monomers, R_{\max} is less than some threshold value. Dependencies of the energies based on this cutoff is considered next.

3.4.2 Dependence of energies on the maximum intermonomer distance, R_{\max}

In subsection 3.4.1, we have shown that R_{\min} is a very good descriptor for the contribution to the three-body crystal lattice energies. However, as stated in subsection 3.3.3, the number

of trimers in a periodic crystal system is infinite, and a cutoff solely based on R_{\min} would not be able to generate a subset with finite number of trimers. Therefore, one also needs to set a cutoff value for R_{\max} to ensure that one only has to compute the three-body interaction energy for a finite number of trimers to obtain the three-body crystal lattice energy. Similar to the analysis for R_{\min} , in Figure 3.4–Figure 3.6, we plot the accumulative three-body lattice energy against the R_{\max} cutoff value.

As opposed to the quick convergence for the crystal lattice energies with respect to R_{\min} , the crystal lattice energies do not show similar quick convergence along different cutoff values of R_{\max} . This suggests that the long-range interactions are crucial in computing three-body lattice energies accurately, and one needs to consider trimers with relatively large R_{\max} . In other words, although one of the intermonomer distances (R_{\min}) needs to be relatively small for the three-body interaction energy to be significant, the longest intermonomer distance (R_{\max}) can be relatively large. As discussed above, CKS and ATM dispersion corrections overestimate the dispersion contribution to the three-body lattice energies, and the Tang–Toennies damping function provides consistent error cancellations and allows the MP2+ATM model to predict the three-body lattice energies with good accuracy.

The accumulative three-body lattice energies for all three crystals appear to be converged by 10 Å. In order to observe if 10 Å is a good cutoff value of R_{\max} , we tabulate the contributions to three-body crystal lattice energies, for various computational methods, over different domains of R_{\max} values in Table 3.4–Table 3.6. For the domains of R_{\max} , we split the “long-range” domain in two: medium-long-range ($7 \text{ \AA} < R_{\max} \leq 10 \text{ \AA}$) and long-range ($10 \text{ \AA} < R_{\max} \leq 15 \text{ \AA}$), resulting in 4 R_{\max} domains. The larger errors from medium-, medium-long- and long-range bins in Table 3.4–Table 3.6, compared to those seen in Table 3.1–Table 3.3, indicate that errors correlate more strongly with the smallest of three pairwise closest contact distances, R_{\min} , than they do with the largest one R_{\max} . From these tables, ignoring trimers with R_{\max} greater than 10 Å introduces approximately 0.1 kJ mol⁻¹ error in the three-body lattice energy at all levels of theory, including the refer-

ence method CCSD(T)/CBS. On the other hand, the long-range domain includes more than 80% of the unique-symmetry trimers considered, so ignoring them would greatly speed up the computation. Therefore, at least for present systems under consideration, where three-body dispersion is expected to be significant, it appears that three-body dispersion contributions are essentially converged for a cutoff R_{\max} of 10 Å. If we use the relatively inexpensive MP2+ATM approach for trimers with $R_{\min} > 4$ Å and $R_{\max} < 10$ Å, we achieve an error of less than 0.2 kJ mol⁻¹ for the three-body contribution to the lattice energy, compared to the full sets of trimers with $R_{\min} > 4$ Å computed with CCSD(T)/CBS. (Note that the damping function in the ATM dispersion correction is irrelevant for $R_{\min} > 4$ Å, so undamped and damped ATM would produce essentially the same results)

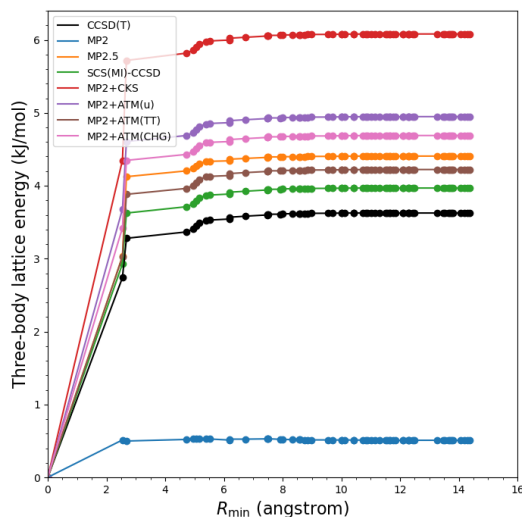


Figure 3.1: Accumulated three-body lattice energy for crystalline benzene as a function of R_{\min} cutoff value, in kJ mol⁻¹. MP2+CKS represents MP2 corrected by the three-body CKS FDDS dispersion term, and MP2+ATM represents MP2 corrected by ATM dispersion correction. The suffixes (u), (TT), and (CHG) correspond to undamped, damped with Tang–Toennies damping function[77, 78], and damped with Chai–Head-Gordon damping function[79], respectively.

Table 3.1: Summary of total three-body contribution to lattice energy (kJ mol^{-1}) of crystalline benzene split by separation domain, for each method involved in this work. Cutoff distances (in \AA) are determined by the smallest of three intermolecular separations, R_{\min} . Percentages reflect the contribution of trimers within each separation domain to the total three-body lattice energy under the corresponding theory level. Errors for each separation range vs. reference CCSD(T)/CBS(a[TQ]Z; δ :aDZ) values in parentheses.

Method	Range			
	Total	Short	Medium	Long
	$R_{\min} \leq 15$	$R_{\min} \leq 4$	$4 < R_{\min} \leq 7$	$7 < R_{\min} \leq 15$
CCSD(T)/CBS(a[TQ]Z; δ :aDZ)	3.63	3.28	0.30	0.04
	100.0%	90.4%	8.4%	1.2%
	Ref.	Ref.	Ref.	Ref.
MP2/CBS(a[TQ]Z)	0.51	0.50	0.03	-0.02
	100.0%	98.0%	5.1%	-3.1%
	(-3.12)	(-2.78)	(-0.28)	(-0.06)
MP2.5/CBS(a[TQ]Z; δ :aDZ)	4.41	4.12	0.25	0.03
	100.0%	93.6%	5.7%	0.7%
	(0.78)	(0.85)	(-0.05)	(-0.01)
SCS(MI)-CCSD/CBS(a[TQ]Z; δ :aDZ)	3.97	3.62	0.30	0.04
	100.0%	91.3%	7.6%	1.1%
	(0.34)	(0.35)	(-0.00)	(0.00)
MP2 + CKS disp	6.08	5.72	0.32	0.05
	100.0%	94.0%	5.2%	0.7%
	(2.46)	(2.44)	(0.01)	(0.00)
MP2 + undamped ATM disp	4.95	4.61	0.30	0.04
	100.0%	93.1%	6.0%	0.9%
	(1.32)	(1.33)	(-0.01)	(-0.00)
MP2 + damped(TT) ATM disp	4.22	3.88	0.30	0.04
	100.0%	91.9%	7.1%	1.0%
	(0.60)	(0.60)	(-0.01)	(-0.00)
MP2 + damped(CHG) ATM disp	4.69	4.35	0.30	0.04
	100.0%	92.7%	6.4%	0.9%
	(1.06)	(1.07)	(-0.01)	(-0.00)
Number of Unique Trimers	1977	494	710	773
	100.0%	25.0%	35.9%	39.1%

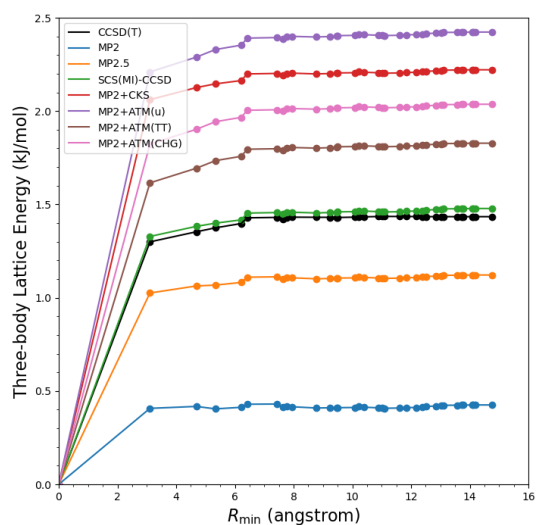


Figure 3.2: Accumulated three-body lattice energy for crystalline carbon dioxide as a function of R_{\min} cutoff value, in kJ mol^{-1} . MP2+CKS represents MP2 corrected by the three-body CKS FDDS dispersion term, and MP2+ATM represents MP2 corrected by ATM dispersion correction. The suffixes (u), (TT), and (CHG) correspond to undamped, damped with Tang–Toennies damping function[77, 78], and damped with Chai–Head-Gordon damping function[79], respectively.

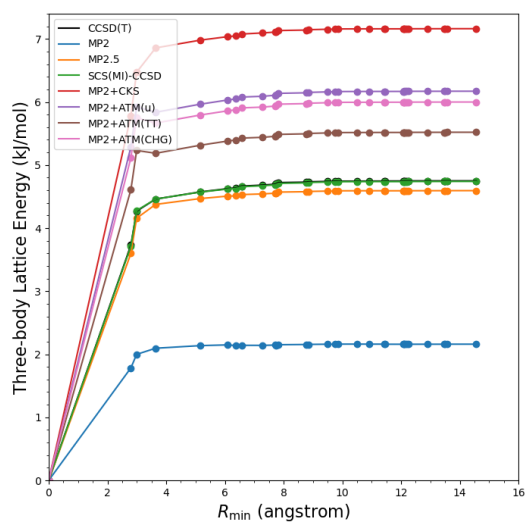


Figure 3.3: Accumulated three-body lattice energy for crystalline triazine as a function of R_{\min} cutoff value, in kJ mol^{-1} . MP2+CKS represents MP2 corrected by the three-body CKS FDDS dispersion term, and MP2+ATM represents MP2 corrected by ATM dispersion correction. The suffixes (u), (TT), and (CHG) correspond to undamped, damped with Tang–Toennies damping function[77, 78], and damped with Chai–Head–Gordon damping function[79], respectively.

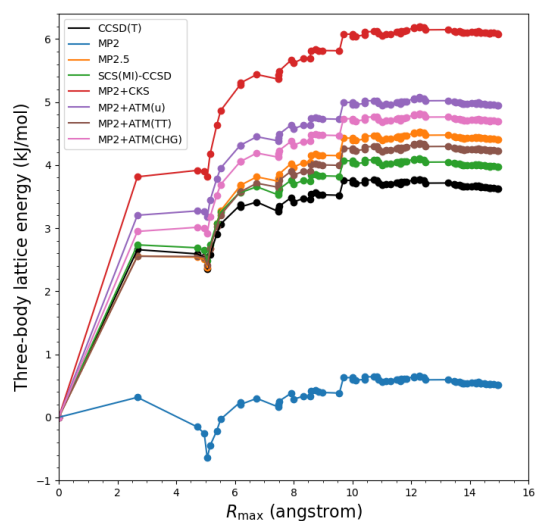


Figure 3.4: Accumulated three-body lattice energy for crystalline benzene as a function of R_{\max} cutoff value, in kJ mol^{-1} . MP2+CKS represents MP2 corrected by the three-body CKS FDDS dispersion term, and MP2+ATM represents MP2 corrected by ATM dispersion correction. The suffixes (u), (TT), and (CHG) correspond to undamped, damped with Tang–Toennies damping function[77, 78], and damped with Chai–Head–Gordon damping function[79], respectively.

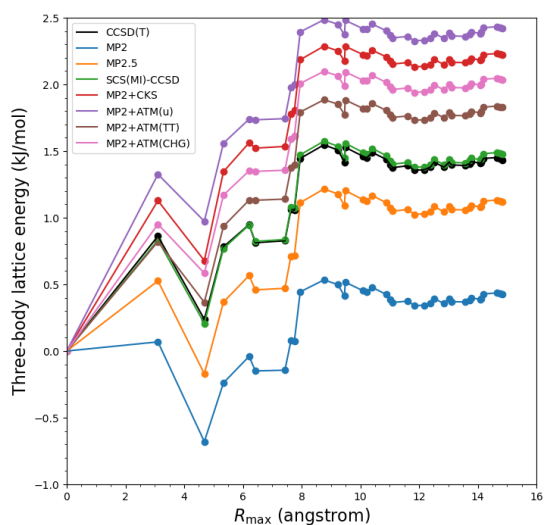


Figure 3.5: Accumulated three-body lattice energy for crystalline carbon dioxide as a function of R_{\max} cutoff value, in kJ mol^{-1} . MP2+CKS represents MP2 corrected by the three-body CKS FDDS dispersion term, and MP2+ATM represents MP2 corrected by ATM dispersion correction. The suffixes (u), (TT), and (CHG) correspond to undamped, damped with Tang–Toennies damping function[77, 78], and damped with Chai–Head-Gordon damping function[79], respectively.

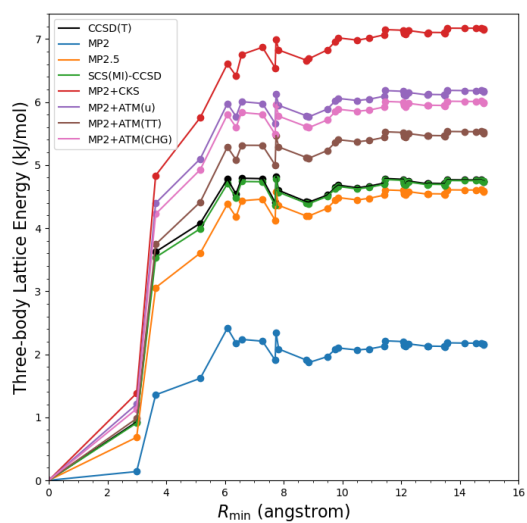


Figure 3.6: Accumulated three-body lattice energy for crystalline triazine as a function of R_{\max} cutoff value, in kJ mol^{-1} . MP2+CKS represents MP2 corrected by the three-body CKS FDDS dispersion term, and MP2+ATM represents MP2 corrected by ATM dispersion correction. The suffixes (u), (TT), and (CHG) correspond to undamped, damped with Tang–Toennies damping function[77, 78], and damped with Chai–Head–Gordon damping function[79], respectively.

Table 3.2: Summary of total three-body contribution to lattice energy (kJ mol^{-1}) of crystalline carbon dioxide split by separation domain, for each method involved in this work. Cutoff distances (in \AA) are determined by the smallest of three intermolecular separations, R_{\min} . Percentages reflect the contribution of trimers within each separation domain to the total three-body lattice energy under the corresponding theory level. Errors for each separation range vs. reference CCSD(T)/CBS(a[TQ]Z; δ :aDZ) values in parentheses.

Method	Range			
	Total $R_{\min} \leq 15$	Short $R_{\min} \leq 4$	Medium $4 < R_{\min} \leq 7$	Long $7 < R_{\min} \leq 15$
CCSD(T)/CBS(a[TQ]Z; δ :aDZ)	1.43	1.30	0.13	0.01
	100.0%	90.6%	9.0%	0.4%
	Ref.	Ref.	Ref.	Ref.
MP2/CBS(a[TQ]Z)	0.43	0.41	0.02	-0.00
	100.0%	95.7%	5.2%	-0.9%
	(-1.01)	(-0.89)	(-0.11)	(-0.01)
MP2.5/CBS(a[TQ]Z; δ :aDZ)	1.12	1.03	0.08	0.01
	100.0%	91.4%	7.5%	1.1%
	(-0.31)	(-0.27)	(-0.04)	(0.01)
SCS(MI)-CCSD/CBS(a[TQ]Z; δ :aDZ)	1.48	1.33	0.13	0.02
	100.0%	89.9%	8.5%	1.7%
	(0.04)	(0.03)	(-0.00)	(0.02)
MP2 + CKS disp	2.22	2.06	0.14	0.02
	100.0%	92.8%	6.2%	1.0%
	(0.79)	(0.76)	(0.01)	(0.02)
MP2 + undamped ATM disp	2.42	2.21	0.18	0.03
	100.0%	91.2%	7.5%	1.3%
	(0.99)	(0.91)	(0.05)	(0.03)
MP2 + damped(TT) ATM disp	1.83	1.62	0.18	0.03
	100.0%	88.4%	9.9%	1.8%
	(0.39)	(0.32)	(0.05)	(0.03)
MP2 + damped(CHG) ATM disp	2.04	1.82	0.18	0.03
	100.0%	89.5%	8.9%	1.6%
	(0.60)	(0.52)	(0.05)	(0.03)
Number of Unique Trimers	1948	309	637	1002
	100.0%	15.9%	32.7%	51.4%

Table 3.3: Summary of total three-body contribution to lattice energy (kJ mol^{-1}) of crystalline triazine split by separation domain, for each method involved in this work. Cutoff distances (in \AA) are determined by the smallest of three intermolecular separations, R_{\min} . Percentages reflect the contribution of trimers within each separation domain to the total three-body lattice energy under the corresponding theory level. Errors for each separation range vs. reference CCSD(T)/CBS(a[TQ]Z; δ :aDZ) values in parentheses.

Method	Range			
	Total $R_{\min} \leq 15$	Short $R_{\min} \leq 4$	Medium $4 < R_{\min} \leq 7$	Long $7 < R_{\min} \leq 15$
CCSD(T)/CBS(a[TQ]Z; δ :aDZ)	4.75	4.46	0.21	0.08
	100.0%	93.9%	4.3%	1.7%
	Ref.	Ref.	Ref.	Ref.
MP2/CBS(a[TQ]Z)	2.16	2.10	0.05	0.02
	100.0%	97.0%	2.1%	0.9%
	(-2.59)	(-2.37)	(-0.16)	(-0.06)
MP2.5/CBS(a[TQ]Z; δ :aDZ)	4.59	4.38	0.16	0.06
	100.0%	95.3%	3.4%	1.3%
	(-0.16)	(-0.08)	(-0.05)	(-0.02)
SCS(MI)-CCSD/CBS(a[TQ]Z; δ :aDZ)	4.74	4.46	0.20	0.08
	100.0%	94.1%	4.1%	1.8%
	(-0.01)	(0.00)	(-0.01)	(0.00)
MP2 + CKS disp	7.16	6.86	0.22	0.08
	100.0%	95.7%	3.1%	1.2%
	(2.41)	(2.40)	(0.01)	(0.00)
MP2 + undamped ATM disp	6.17	5.84	0.24	0.09
	100.0%	94.6%	3.9%	1.5%
	(1.42)	(1.38)	(0.04)	(0.01)
MP2 + damped(TT) ATM disp	5.52	5.19	0.24	0.09
	100.0%	94.0%	4.4%	1.7%
	(0.77)	(0.73)	(0.03)	(0.01)
MP2 + damped(CHG) ATM disp	6.00	5.67	0.24	0.09
	100.0%	94.4%	4.0%	1.5%
	(1.25)	(1.21)	(0.04)	(0.01)
Number of Unique Trimers	750	211	210	329
	100.0%	28.1%	28.0%	43.9%

Table 3.4: Summary of total three-body contribution to lattice energy (kJ mol^{-1}) of crystalline benzene split by separation domain, for each method involved in this work. Cutoff distances (in Å) are determined by the largest of three intermolecular separations, R_{max} . Percentages reflect the contribution of trimers within each separation domain to the total three-body lattice energy under the corresponding theory level. Errors for each separation range vs. reference CCSD(T)/CBS(a[TQ]Z; δ :aDZ) values in parentheses.

Method	Range				
	Total $R_{\text{max}} \leq 15$	Short $R_{\text{max}} \leq 4$	Medium $4 < R_{\text{max}} \leq 7$	Medium-Long $7 < R_{\text{max}} \leq 10$	Long $10 < R_{\text{max}} \leq 15$
CCSD(T)/CBS(a[TQ]Z; δ :aDZ)	3.63	2.66	0.75	0.35	-0.14
	100.0%	73.3%	20.8%	9.6%	-3.8%
	Ref.	Ref.	Ref.	Ref.	Ref.
MP2/CBS(a[TQ]Z)	0.51	0.32	-0.02	0.33	-0.12
	100.0%	62.3%	-3.3%	64.9%	-23.9%
	(-3.12)	(-2.34)	(-0.77)	(-0.02)	(0.02)
MP2.5/CBS(a[TQ]Z; δ :aDZ)	4.41	2.56	1.25	0.62	-0.02
	100.0%	58.1%	28.4%	14.0%	-0.5%
	(0.78)	(-0.10)	(0.50)	(0.27)	(0.12)
SCS(MI)-CCSD/CBS(a[TQ]Z; δ :aDZ)	3.97	2.73	0.92	0.42	-0.10
	100.0%	68.9%	23.2%	10.5%	-2.6%
	(0.34)	(0.08)	(0.17)	(0.07)	(0.03)
MP2 + CKS disp	6.08	3.81	1.62	0.64	0.00
	100.0%	62.7%	26.7%	10.5%	0.1%
	(2.46)	(1.16)	(0.87)	(0.29)	(0.14)
MP2 + undamped ATM disp	4.95	3.20	1.25	0.54	-0.04
	100.0%	64.8%	25.2%	11.0%	-0.9%
	(1.32)	(0.55)	(0.49)	(0.19)	(0.09)
MP2 + damped(TT) ATM disp	4.22	2.55	1.16	0.55	-0.04
	100.0%	60.5%	27.4%	13.1%	-1.0%
	(0.60)	(-0.11)	(0.40)	(0.20)	(0.10)
MP2 + damped(CHG) ATM disp	4.69	2.95	1.24	0.54	-0.04
	100.0%	62.9%	26.5%	11.6%	-1.0%
	(1.06)	(0.29)	(0.49)	(0.19)	(0.09)
Number of Unique Trimers	1977	4	52	173	1748
	100.0%	0.2%	2.6%	8.8%	88.4%

Table 3.5: Summary of total three-body contribution to lattice energy (kJ mol^{-1}) of crystalline carbon dioxide split by separation domain, for each method involved in this work. Cutoff distances (in Å) are determined by the largest of three intermolecular separations, R_{max} . Percentages reflect the contribution of trimers within each separation domain to the total three-body lattice energy under the corresponding theory level. Errors for each separation range vs. reference CCSD(T)/CBS(a[TQ]Z; δ :aDZ) values in parentheses.

Method	Range				
	Total $R_{\text{max}} \leq 15$	Short $R_{\text{max}} \leq 4$	Medium $4 < R_{\text{max}} \leq 7$	Medium-Long $7 < R_{\text{max}} \leq 10$	Long $10 < R_{\text{max}} \leq 15$
CCSD(T)/CBS(a[TQ]Z; δ :aDZ)	1.43	0.86	-0.05	0.72	-0.09
	100.0%	60.1%	-3.5%	49.9%	-6.6%
	Ref.	Ref.	Ref.	Ref.	Ref.
MP2/CBS(a[TQ]Z)	0.43	0.07	-0.22	0.67	-0.09
	100.0%	16.1%	-51.2%	156.5%	-21.4%
	(-1.01)	(-0.79)	(-0.17)	(-0.05)	(0.00)
MP2.5/CBS(a[TQ]Z; δ :aDZ)	1.12	0.53	-0.07	0.74	-0.08
	100.0%	46.9%	-6.0%	66.4%	-7.3%
	(-0.31)	(-0.34)	(-0.02)	(0.03)	(0.01)
SCS(MI)-CCSD/CBS(a[TQ]Z; δ :aDZ)	1.48	0.83	-0.01	0.74	-0.08
	100.0%	56.3%	-0.6%	49.8%	-5.5%
	(0.04)	(-0.03)	(0.04)	(0.02)	(0.01)
MP2 + CKS disp	2.22	1.13	0.39	0.76	-0.06
	100.0%	50.8%	17.7%	34.4%	-2.9%
	(0.79)	(0.27)	(0.44)	(0.05)	(0.03)
MP2 + undamped ATM disp	2.42	1.33	0.41	0.75	-0.06
	100.0%	54.7%	16.9%	30.8%	-2.4%
	(0.99)	(0.46)	(0.46)	(0.03)	(0.04)
MP2 + damped(TT) ATM disp	1.83	0.82	0.31	0.75	-0.06
	100.0%	44.9%	17.0%	41.1%	-3.0%
	(0.39)	(-0.04)	(0.36)	(0.04)	(0.04)
MP2 + damped(CHG) ATM disp	2.04	0.95	0.40	0.75	-0.06
	100.0%	46.7%	19.4%	36.6%	-2.8%
	(0.60)	(0.09)	(0.45)	(0.03)	(0.04)
Number of Unique Trimers	1948	2	27	159	1760
	100.0%	0.1%	1.4%	8.2%	90.3%

Table 3.6: Summary of total three-body contribution to lattice energy (kJ mol^{-1}) of crystalline triazine split by separation domain, for each method involved in this work. Cutoff distances (in Å) are determined by the largest of three intermolecular separations, R_{max} . Percentages reflect the contribution of trimers within each separation domain to the total three-body lattice energy under the corresponding theory level. Errors for each separation range vs. reference CCSD(T)/CBS(a[TQ]Z; δ :aDZ) values in parentheses.

Method	Range				
	Total $R_{\text{max}} \leq 15$	Short $R_{\text{max}} \leq 4$	Medium $4 < R_{\text{max}} \leq 7$	Medium-Long $7 < R_{\text{max}} \leq 10$	Long $10 < R_{\text{max}} \leq 15$
CCSD(T)/CBS(a[TQ]Z; δ :aDZ)	4.75	3.62	1.17	-0.11	0.07
	100.0%	76.3%	24.6%	-2.3%	1.4%
	Ref.	Ref.	Ref.	Ref.	Ref.
MP2/CBS(a[TQ]Z)	2.16	1.36	0.88	-0.14	0.06
	100.0%	62.8%	40.7%	-6.3%	2.8%
	(-2.59)	(-2.27)	(-0.29)	(-0.03)	(-0.01)
MP2.5/CBS(a[TQ]Z; δ :aDZ)	4.59	3.06	1.38	0.05	0.11
	100.0%	66.5%	30.0%	1.1%	2.4%
	(-0.16)	(-0.57)	(0.21)	(0.16)	(0.04)
SCS(MI)-CCSD/CBS(a[TQ]Z; δ :aDZ)	4.74	3.54	1.20	-0.08	0.08
	100.0%	74.6%	25.4%	-1.6%	1.7%
	(-0.01)	(-0.09)	(0.03)	(0.03)	(0.01)
MP2 + CKS disp	7.16	4.83	1.92	0.26	0.15
	100.0%	67.5%	26.8%	3.7%	2.0%
	(2.41)	(1.21)	(0.75)	(0.38)	(0.08)
MP2 + undamped ATM disp	6.17	4.40	1.61	0.05	0.12
	100.0%	71.2%	26.1%	0.8%	1.9%
	(1.42)	(0.77)	(0.44)	(0.16)	(0.05)
MP2 + damped(TT) ATM disp	5.52	3.74	1.57	0.09	0.12
	100.0%	67.8%	28.5%	1.6%	2.2%
	(0.77)	(0.12)	(0.40)	(0.20)	(0.05)
MP2 + damped(CHG) ATM disp	6.00	4.22	1.61	0.05	0.12
	100.0%	70.4%	26.8%	0.8%	1.9%
	(1.25)	(0.60)	(0.44)	(0.16)	(0.05)
Number of Unique Trimers	750	3	15	98	634
	100.0%	0.4%	2.0%	13.1%	84.5%

3.5 Conclusions

We have computed the three-body contributions to the lattice energies of crystalline benzene, carbon dioxide, and triazine, using various computational methods, including CCSD(T), MP2, MP2.5 and SCS(MI)-CCSD. In these crystals, the three-body dispersion is crucial in estimating the crystal lattice energies, and MP2 is known to be lacking three-body dispersion. Therefore, we have also employed the MP2+CKS and MP2+ATM methods, which add the coupled Kohn-Sham and Axilrod–Teller–Muto dispersion corrections (with the Tang–Toennies[77, 78] or Chai–Head-Gordon[79] damping function) to the MP2 interaction energies, to provide the three-body dispersion effects missing in MP2. Our results show that MP2+CKS significantly overestimates the three-body dispersion contribution to the lattice energies for these crystals, and MP2+ATM with the Tang–Toennies damping scheme provides a fortuitous but consistent error cancellation and matches well with the reference values from CCSD(T). Interestingly enough, the outstanding performance of MP2+ATM(TT) was also confirmed in predicting liquid state properties [87, 88], indicating that the Tang–Toennies damping scheme might be a good universal choice to combine with the ATM dispersion formula when estimating three-body dispersion energies. SCS(MI)-CCSD retains its outstanding performance in estimating the three-body interaction energies for gas-phase trimer systems[68] in computing the three-body lattice energies in molecular crystals, and MP2.5 becomes less robust in crystal systems despite its good performance in gas-phase trimers.

We also showed that the three-body contributions to lattice energies converge rapidly as the smallest of three pairwise intermonomer closest contact distances R_{\min} grows. The trimers with $R_{\min} < 4 \text{ \AA}$ contributes more than 90% of the total three-body lattice energies for all three crystals, and with almost all computational methods studied. The three-body contributions to lattice energies, especially the dispersion contribution, also converge as the largest of the three intermonomer closest contact distances R_{\max} exceeds 10 \AA . For crystal

systems with significant dispersion influence, like the ones studied in this work, one can estimate the three-body contributions to the crystal lattice energies by using the inexpensive MP2+ATM method for trimers with $R_{\min} > 4 \text{ \AA}$ and $R_{\max} < 10 \text{ \AA}$, and neglecting trimers with $R_{\max} > 10 \text{ \AA}$. Such an approximation drastically reduces the computational resources needed to compute the three-body lattice energies, which involves three-body interaction energy calculations for a massive set of trimers. The errors introduced by this approximation are less than 0.2 kJ mol^{-1} , for the crystals studied here. In systems with larger three-body induction effects, which we might expect in molecular crystals of molecules with larger dipole moments, larger cutoff values for R_{\min} and R_{\max} could be needed. Nevertheless, we would expect MP2 to be satisfactory in describing the long-range induction interactions.

CHAPTER 4

CONCLUSIONS AND OUTLOOK

4.1 Conclusions

In this thesis, we have implemented the Symmetry-Adapted Perturbation Theory with a Kohn-Sham density functional description of the monomers [SAPT(DFT)], as a part of the PSI4 quantum chemistry program package[48], and assessed its performance. With an optimized algorithm as described in Chapter 2, our code is capable to perform SAPT(DFT) calculations for systems with up to ~ 3000 basis functions with hybrid DFT functionals. This allows one to run hybrid SAPT(DFT) calculations on some relatively complicated dimers like the C_{60} -buckycatcher complex, which has a basis function count of 3012 under the aug-cc-pVDZ basis set. We have also tested the accuracies of each SAPT term our SAPT(DFT) code against higher-level SAPT methods, including SAPT(CCSD) and SAPT2+3(CCD) δ MP2, for the Korona S2 dimer set and the S66 dimer set. Our SAPT(DFT) code are shown to have similar accuracies with the SAPT2+ method, which scales as $O(N^7)$.

This work also allowed us to complete a fully-featured open-source implementation of SAPT(DFT) for the first time, which In the past years, Dr. Daniel Smith had written the majority of the current SAPT(DFT) code in PSI4, but left the issue of compatibility between the ALDA exchange-correlation kernel and hybrid functionals unsolved. Our work on the implementation of hybrid ALDA kernels allowed us to complete a fully-featured open-source implementation of SAPT(DFT) for the first time. In other SAPT(DFT) implementations in other non-open-source software packages, including Molpro[60] or SAPT2020[38], the use of hybrid functionals were limited to small systems. The convergence of the local Hartree-Fock iterations had been a severe problem in the Molpro DFT-SAPT (this name is

used by Hesselmann and Jansen instead of SAPT(DFT)[34]) code, and the hybrid ALDA kernel implementation in SAPT2020 suffers from disk storage issues and inefficient disk I/O operations. Our implementation have solved the issues in SAPT2020, by making use of the powerful `lib3index` library in PSI4 designed for operating three-index integrals involved in density-fitting algorithms. We also employed the 2-index representation of the xc kernel, proposed by Pitoňák and Hesselmann, which highly improved the efficiency on calculations involving the kernel.

The success of the hybrid kernel SAPT(DFT) implementation stimulated our group to generalize the SAPT(DFT) dispersion energy to the three-body case, and the coding of this part was lead by our colleague, Zach Glick. Despite the outstanding performance of our SAPT(DFT) code for two-body interactions, in particular the second-order dispersion term, the three-body dispersion energies are shown to be less satisfactory by Beran and coworkers[68, 73]. In their work, they added the three-body dispersion term of SAPT(DFT), which they referred to as “CKS dispersion correction”, to the MP2 nonadditive three-body interaction energy to estimate the total nonadditive three-body interaction energy of a trimer, and compare it to the CCSD(T) result, which is considered as the “gold standard” for interaction energies. For the 3B-69 data set, a set of 69 trimers extracted from 23 different crystal structures, as well as a potential surface computation for pyrazole trimer, the CKS dispersion correction seems to be regularly overestimating the three-body dispersion interactions within trimers, especially for trimers with short intermonomer distances. Our research further studied this issue for a few molecular crystals with significant dispersion interactions, including crystalline benzene, carbon dioxide and triazine. Unfortunately, the CKS dispersion scheme continues to overestimate the three-body dispersion for these crystals. Interestingly enough, the Axilrod–Teller–Muto dispersion correction[70, 71] with an empirical short-range damping using the Tang–Toennies damping function[77, 78] provides much more accurate three-body dispersion energies than CKS, for both 3B-69 and the molecular crystals. Beran and coworkers attributed this to the lack of higher-order exchange and cor-

relation terms for the CKS dispersion correction. Our results agree with this statement, and suggest that the missing term is most likely the three-body exchange-dispersion term. This is because the CKS dispersion is shown to be very accurate for trimers with their monomers far apart from each other, in particular for those with the the smallest value among the three pairwise intermonomer closest-contact distances, R_{\min} , larger than 4 Å. This indicates that the discrepancy in the CKS dispersion mainly arises from exchange repulsion effects.

Besides these findings on the CKS dispersion correction, we have also obtained a few conclusions on studying crystalline benzene, carbon dioxide and triazine. We have concluded that the trimers with $R_{\min} < 4$ Å contribute more than 90% of the nonadditive three-body lattice energies. Also, for trimers with $R_{\min} \geq 4$ Å, we have shown that the cheaper methods, such as MP2 corrected with the ATM or CKS dispersion, are capable for compute the three-body contributions to lattice energies nearly as accurately as CCSD(T). We have also shown that these three-body contributions also start to become negligible as the largest of the three pairwise intermonomer closest contact distances, R_{\max} , exceeds 10 Å. In this study, we have been mainly investigating molecular crystals with significant dispersion effects, and for such crystals, we have proposed to accelerate the computation of the three-body contributions to lattice energies by using a cheaper method for trimers $R_{\min} \geq 4$ Å, and neglecting trimers with a value of $R_{\max} \geq 10$ Å.

4.2 Outlook

As we have discussed above, a few questions have arisen from the studies in this thesis.

In the PSI4 software package, we have successfully implemented a SAPT(DFT) algorithm with support of hybrid exchange-correlation kernel for the dispersion term. However, as discussed in Chapter 2, the exchange-dispersion energy in our code is estimated by applying a scaling factor of 0.770 to its uncoupled approximation. This scaling scheme is proposed by Hesselmann and Korona in 2014[43], to avoid the requirement of storing 4-index TDDFT amplitudes on disk in an explicit exchange-dispersion energy calculation. In

2020, Garcia and Szalewicz proposed a new algorithm that solves this storage issue[54], but this algorithm does not support hybrid exchange-correlation kernel. In a future work, we expect to extend Garcia and Szalewicz’s algorithm to the case of using a hybrid kernel. To achieve this goal, one would need to study the formalism of computing the hybrid kernel FDDS in Chapter 2, as well as the algorithm of Garcia and Szalewicz on avoiding storage of 4-index amplitudes. It would also be helpful to read the group notes by Dr. Jerome Gonthier on the formulae of USAPT0, which includes algebraic details on calculating various SAPT terms. The exchange-dispersion part of the FISAPT code in PSI4, written by Dr. Rob Parrish, is also worth studying on understanding how the FDDS should be contracted with the one- and two-electron integrals. The good news is one should be able to use FDDS formed in the current SAPT(DFT) as-is in computing the exchange-dispersion energy, which reduces the effort needed for this implementation.

Also, as discussed above, the three-body dispersion term of SAPT(DFT) overestimates the three-body dispersion interaction, and this is likely because there is a missing term of the third-order three-body exchange-dispersion energy. While Podeszwa and Szalewicz have derived the SAPT(DFT) terms for three-body interactions, the derivation of third-order exchange-dispersion energy was absent. Therefore, the derivation and implementation of this exchange-dispersion term is of strong interest, and a future work could validate if adding this term would improve the accuracy of the three-body SAPT(DFT) dispersion energies. However, the derivation of the third-order exchange-dispersion term might not be trivial, since it requires a comprehensive understanding of how the SAPT terms were derived, and someone who is interested in deriving it needs to be able to handle the anti-symmetry operator. The implementation of this term is also expected to be harder than that of the two-body exchange-dispersion term, if one intends to use the hybrid kernel FDDS. It is possible to perform a scaling on the “uncoupled” third-order exchange-dispersion energy as we have done in Chapter 2, but it is not guaranteed that the value suggested, 0.770, will still be valid for the three-body third-order case, and it would be a challenging task to

determine this scaling factor if 0.770 would not work.

In our studies in Chapter 3, all three molecular crystals we had covered are influenced significantly by three-body dispersion interactions, i.e., the three-body dispersion contributes majorly to the total three-body contribution to their lattice energies. We have proposed from the results from these crystals that the three-body lattice energies converge at $R_{\min} = 4 \text{ \AA}$ and $R_{\max} = 10 \text{ \AA}$, but this has not been confirmed for crystals consisting of polar molecules with stronger dipole-dipole interactions, which indicates a stronger three-body induction contribution. A study on these molecular crystals with less three-body dispersion influences will be interesting, in terms of determining if the cutoff values for R_{\min} and R_{\max} proposed in Chapter 3 are reasonable for these crystal systems.

Appendices

APPENDIX A
SUPPLEMENTARY DATA FOR CHAPTER 2

Table A.1: Mean absolute deviations (kcal mol^{-1}) of the interaction energy components of SAPT2+3(CCD) δ MP2/aug-cc-pVTZ vs SAPT(CCSD)/aug-cc-pVTZ values for the Korona S2 test set.

Method	MAD	Error Distribution ^a						
		4	OB	1	0	1	UB	4
Electrostatics	0.201				█	█		
Exchange	0.107				█	█		
Total Induction (Induction + Exchange-Induction)	0.179				█	█		
Total Dispersion (Dispersion + Exchange-Dispersion)	0.099				█	█		
Total	0.321				█	█		

Table A.2: Mean absolute errors (kcal mol⁻¹) and mean unsigned relative errors (%) of the interaction energy components for the Korona S2 test set with various SAPT methods and the aug-cc-pVTZ basis set.

Method ^a	MAE	MURE	Error Distribution ^b					
			4	OB	1	0	1	UB
Electrostatics								
SAPT(DFT) hybrid	0.112	2.39						
SAPT(DFT) LHF	0.114	3.68						
SAPT0	0.526	12.54			█			
Exchange								
SAPT(DFT) hybrid	0.251	3.38			█			
SAPT(DFT) LHF	0.258	3.09			█			
SAPT0	1.735	13.78	█					
Induction								
SAPT(DFT) hybrid	0.148	2.79			█			
SAPT(DFT) LHF	0.192	2.97			█			
SAPT0	1.616	14.74	█					
Exchange-Induction								
SAPT(DFT) hybrid	0.144	4.03			█			
SAPT(DFT) LHF	0.165	4.76			█			
SAPT0	1.257	23.17	█					
Dispersion								
SAPT(DFT) hybrid	0.175	3.68			█			
SAPT(DFT) LHF	0.141	2.77			█			
SAPT(DFT) non-hybrid	0.326	9.58			█			
SAPT0	0.501	15.02		█				
Exchange-Dispersion								
SAPT(DFT) hybrid	0.062	12.47			█			
SAPT(DFT) LHF	0.039	3.25			█			
SAPT0	0.198	24.14			█			
Total								
SAPT(DFT) hybrid	0.155	4.98			█			
SAPT(DFT) LHF	0.189	4.17			█			
SAPT(DFT) hon-hybrid	0.244	10.64			█			
SAPT0	1.657	17.10	█					

Table A.3: Mean absolute error (kcal mol⁻¹) of the interaction energy for S66 with various SAPT methods and the aug-cc-pVTZ basis set.

Method ^a	Total	HB	MX	DD	Error Distribution ^b					
					4	OB	1	0	1	UB
Electrostatics										
SAPT(DFT) hybrid	0.374	0.556	0.177	0.311						
SAPT(DFT) LHF	0.423	0.666	0.196	0.319						
SAPT0	0.585	0.995	0.401	0.287						
SAPT2+	0.142	0.175	0.093	0.138						
SAPT2+(3) δ MP2	0.000	0.000	0.000	0.000						
Exchange										
SAPT(DFT) hybrid	0.886	1.127	0.426	0.926						
SAPT(DFT) LHF	0.886	1.121	0.431	0.928						
SAPT0	0.691	0.956	0.277	0.679						
SAPT2+	0.000	0.000	0.000	0.000						
SAPT2+(3) δ MP2	0.000	0.000	0.000	0.000						
Induction										
SAPT(DFT) hybrid	0.211	0.201	0.212	0.220						
SAPT(DFT) LHF	0.224	0.223	0.223	0.225						
SAPT0	0.270	0.261	0.281	0.272						
SAPT2+	0.314	0.365	0.248	0.304						
SAPT2+(3) δ MP2	0.152	0.179	0.121	0.145						
Dispersion										
SAPT(DFT) hybrid	0.370	0.260	0.219	0.573						
SAPT(DFT) LHF	0.308	0.200	0.173	0.499						
SAPT(DFT) non-hybrid	0.635	0.581	0.419	0.822						
SAPT0	0.396	0.429	0.239	0.459						
SAPT2+	0.147	0.062	0.118	0.249						
SAPT2+(3) δ MP2	0.093	0.129	0.056	0.080						
Total										
SAPT(DFT) hybrid	0.334	0.588	0.107	0.217						
SAPT(DFT) LHF	0.234	0.382	0.046	0.199						
SAPT(DFT) non-hybrid	0.604	0.955	0.389	0.385						
SAPT0	1.372	1.672	1.002	1.296						
SAPT2+	0.567	0.540	0.438	0.672						
SAPT2+(3) δ MP2	0.105	0.056	0.082	0.169						

APPENDIX B
DERIVATION OF HYBRID KERNEL FDDS EQUATIONS

From the equation of FDDS by Bukowski et al. in Ref. 36:

$$\tilde{\mathbf{C}} = \overline{\mathbf{D}}^T \boldsymbol{\lambda} \mathbf{H}^{(2)} \overline{\mathbf{D}} + \overline{\mathbf{D}}^T \boldsymbol{\lambda} \overline{\mathbf{F}}' \left(\tilde{\mathbf{I}} - \overline{\mathbf{D}}^T \boldsymbol{\lambda} \overline{\mathbf{F}}' \right)^{-1} \overline{\mathbf{D}}^T \boldsymbol{\lambda} \mathbf{H}^{(2)} \overline{\mathbf{D}}. \quad (\text{B.1})$$

The purpose of separating the diagonal and non-diagonal part of \mathbf{R} in the algorithm of Bukowski et al. is to avoid the inversion of a $ov \times ov$ matrix which would scale as $O(o^3v^3)$, where o and v represent the number of occupied and virtual molecular orbitals, respectively. By separating the non-diagonal part of \mathbf{R} and then collecting its contribution in \mathbf{R}' , they converted the solution to a power series of \mathbf{R}' , each term of which can be represented as a density-fitted representation with a scaling of $O(o^2v^2Q)$, where Q is the number of density-fitting auxiliary functions. In our algorithms, as we will see later, the power series expansion is avoided by computing the pseudoinverse of the three-index density-fitting integral with QR factorization. This also eliminates the need of separating the diagonal and non-diagonal part of \mathbf{R} . Therefore, instead of the definition of $\boldsymbol{\lambda}$ given by Bukowski et al.:

$$\boldsymbol{\lambda} = -4 \left(\mathbf{d}^2 + \mathbf{r} + \omega^2 \mathbf{I}_{ov} \right)^{-1}, \quad (\text{B.2})$$

we have

$$\begin{aligned} \boldsymbol{\lambda} &= -4 \left(\mathbf{d}^2 + \omega^2 \mathbf{I}_{ov} \right)^{-1} \\ &= -\frac{4}{\epsilon_{ar}^2 + \omega^2}, \end{aligned} \quad (\text{B.3})$$

and

$$\boldsymbol{\lambda} \mathbf{d} = \frac{4\epsilon_{ar}}{\epsilon_{ar}^2 + \omega^2} \quad (\text{B.4})$$

Now, we convert the notations in Ref. 36 into those used in Ref. 39, which expresses most intermediate quantities as $Q \times Q$ matrices and allows easier and faster implementation. Equation 9 of Ref. 36 writes:

$$\begin{aligned}\phi_a \phi_r &\approx \sum_Q \bar{\mathbf{D}}_{ar,Q} \chi_Q \\ &= \sum_{PQ} (ar|P) [\mathbf{S}^{-1}]_{PQ} \chi_Q,\end{aligned}\tag{B.5}$$

from which we have

$$(ar|Q) = \bar{\mathbf{D}} \tilde{\mathbf{S}},\tag{B.6}$$

where both \mathbf{S} under our notation and $\tilde{\mathbf{S}}$ under the notation of Bukowski et al. represent the overlap matrix of the auxiliary basis, $(P|Q)$. Note that \mathbf{S} is symmetric, so $\mathbf{S} = \mathbf{S}^T$. To avoid confusion, we will always use \mathbf{S} to represent the overlap matrix in the rest of this chapter.

We then have

$$\begin{aligned}(\chi_0)_{PQ} &= (P|ar) \frac{4\epsilon_{ar}}{\epsilon_{ar}^2 + \omega^2} (ar|Q) \\ &= \left(\mathbf{S} \bar{\mathbf{D}}^T \boldsymbol{\lambda} \mathbf{D} \bar{\mathbf{S}} \right)_{PQ},\end{aligned}$$

and

$$\begin{aligned}(\mathbf{W})_{PQ} &= (P|r_{12}^{-1}|Q) + (P|f_{xc}|Q) \\ &= \int \chi_P(1) \frac{1}{r_{12}} \chi_Q(2) d\mathbf{r}_1 d\mathbf{r}_2 + \int \chi_P \chi_Q \frac{\delta v_{xc}}{\delta \rho} d\mathbf{r}.\end{aligned}\tag{B.7}$$

Comparing Equation B.7 with equation 13 of Ref. 36, one obtains

$$\bar{\mathbf{F}} = \bar{\mathbf{D}} \mathbf{W},\tag{B.8}$$

and

$$\begin{aligned}\chi_0 \mathbf{S}^{-1} \mathbf{W} &= (\mathbf{S} \overline{\mathbf{D}}^T \lambda d \overline{\mathbf{D}} \mathbf{S}) \cdot \mathbf{S}^{-1} \mathbf{W} \\ &= \mathbf{S} \overline{\mathbf{D}}^T \lambda d \overline{\mathbf{F}}.\end{aligned}\tag{B.9}$$

Now we define $\overline{\mathbf{A}}$ that satisfies

$$\overline{\mathbf{A}} \mathbf{D}^T = \mathbf{R}.\tag{B.10}$$

and then we have

$$\mathbf{R} \mathbf{P} = \overline{\mathbf{A}} \mathbf{D}^T = \mathbf{R},\tag{B.11}$$

$$\mathbf{R} \mathbf{Q} = \mathbf{R}' = \mathbf{0}.\tag{B.12}$$

To avoid confusion, in the following contexts, we will use \mathbf{R}' to represent \mathbf{R} in Ref. 36, since we will reserve \mathbf{R} for some other quantity. We will also redefine \mathbf{Q} , and the readers are suggested not to confuse \mathbf{Q} in the following context with the one in Ref. 36.

To solve for $\overline{\mathbf{A}}$, we need to compute the pseudoinverse of $\overline{\mathbf{D}}^T$:

$$\begin{aligned}[\overline{\mathbf{D}}^T]^\dagger &= [\mathbf{S}^{-1}(Q|ar)]^\dagger \\ &= [(Q|ar)]^\dagger \mathbf{S} \\ &= \mathbf{Q}(\mathbf{R}^T)^{-1} \mathbf{S},\end{aligned}\tag{B.13}$$

where we defined \mathbf{Q} and \mathbf{R} to be the result of the QR factorization of $(ar|Q)$:

$$(ar|Q) = \mathbf{Q}\mathbf{R}.\tag{B.14}$$

We can then solve for $\bar{\mathbf{A}}$:

$$\begin{aligned}\bar{\mathbf{A}} &= \mathbf{R}' \left[\bar{\mathbf{D}}^T \right]^\dagger \\ &= \mathbf{R}' \mathbf{Q} (\mathbf{R}^T)^{-1} \mathbf{S}^{-1}.\end{aligned}\tag{B.15}$$

Now we look at the components in Equation B.1 and attempt to translate them into our notations. We first look at $\bar{\mathbf{D}}^T \boldsymbol{\lambda} \mathbf{H}^{(2)} \bar{\mathbf{D}}$:

$$\begin{aligned}\bar{\mathbf{D}}^T \boldsymbol{\lambda} \mathbf{H}^{(2)} \bar{\mathbf{D}} &= \bar{\mathbf{D}}^T \boldsymbol{\lambda} \mathbf{d} \bar{\mathbf{D}} + \bar{\mathbf{D}}^T \boldsymbol{\lambda} \mathbf{H}_r^{(2)} \bar{\mathbf{D}} \\ &= \mathbf{S}^{-1} \boldsymbol{\chi}_0 \mathbf{S}^{-1} + \bar{\mathbf{D}}^t \boldsymbol{\lambda} \mathbf{H}_r^{(2)} \bar{\mathbf{D}}.\end{aligned}\tag{B.16}$$

Now we define $\mathbf{K}'_2(\boldsymbol{\lambda})$ with $\boldsymbol{\lambda}$ as a set of parameter:

$$[\mathbf{K}'_2(\boldsymbol{\lambda})]_{PQ} = \sum_{ar, a'r'} (P|ar) \lambda_{ar} [(aa'|rr') - (ar'|a'r)] (a'r'|Q),\tag{B.17}$$

and also define a “corrected” $\boldsymbol{\chi}_0, \boldsymbol{\chi}'_0$, as described in Chapter 2:

$$\boldsymbol{\chi}'_0 = \boldsymbol{\chi}_0 - \xi \mathbf{K}'_2(\boldsymbol{\lambda}),\tag{B.18}$$

and then we can rewrite Equation B.16 as

$$\bar{\mathbf{D}}^T \boldsymbol{\lambda} \mathbf{H}^{(2)} \bar{\mathbf{D}} = \mathbf{S}^{-1} \boldsymbol{\chi}'_0 \mathbf{S}^{-1}.\tag{B.19}$$

For the other major component $\bar{\mathbf{D}}^T \boldsymbol{\lambda} \mathbf{F}'$, we have

$$\bar{\mathbf{D}}^T \boldsymbol{\lambda} \mathbf{F}' = \bar{\mathbf{D}}^T \boldsymbol{\lambda} \mathbf{H}^{(2)} \mathbf{F} + \frac{1}{4} \bar{\mathbf{D}}^T \boldsymbol{\lambda} \bar{\mathbf{A}}.\tag{B.20}$$

The first term can be rewritten as

$$\begin{aligned}\bar{\mathbf{D}}^T \boldsymbol{\lambda} \mathbf{H}^{(2)} \mathbf{F} &= \bar{\mathbf{D}}^T \boldsymbol{\lambda} \mathbf{H}^{(2)} \bar{\mathbf{D}} \mathbf{W} \\ &= \mathbf{S}^{-1} \boldsymbol{\chi}'_0 \mathbf{S}^{-1} \mathbf{W},\end{aligned}\tag{B.21}$$

and for the second term

$$\bar{\mathbf{D}}^T \boldsymbol{\lambda} \bar{\mathbf{A}} = \bar{\mathbf{D}}^T \boldsymbol{\lambda} \mathbf{R}' \mathbf{Q} (\mathbf{R}^T)^{-1} \mathbf{S}.\tag{B.22}$$

We can now expand \mathbf{R}' using the definition in Ref. 36, and define the quantities based on each term of $\bar{\mathbf{D}}^T \boldsymbol{\lambda} \mathbf{R}' \mathbf{Q}$ as in Equation 2.43, Equation 2.44, Equation 2.45, and Equation 2.46. With these definitions, we can rewrite Equation B.22 as

$$\begin{aligned}\bar{\mathbf{D}}^T \boldsymbol{\lambda} \bar{\mathbf{A}} &= \bar{\mathbf{D}}^T \boldsymbol{\lambda} \mathbf{R}' \mathbf{Q} (\mathbf{R}^T)^{-1} \mathbf{S} \\ &= \mathbf{S}^{-1} \mathbf{K} (\mathbf{R}^T)^{-1} \mathbf{S}.\end{aligned}\tag{B.23}$$

Before finalizing the derivation, we first point out that the FDDS matrix $\boldsymbol{\chi}$ in our notations are not the same with $\tilde{\mathbf{C}}$ in that of Bukowski et al. Imposing Equation B.7 and Equation B.9 into the equation of $\boldsymbol{\chi}$ for the non-hybrid kernel case in Ref. 39, we get

$$\begin{aligned}\boldsymbol{\chi} &= \boldsymbol{\chi}_0 + \boldsymbol{\chi}_0 \mathbf{S}^{-1} \mathbf{W} (\mathbf{S} - \boldsymbol{\chi}_0 \mathbf{S}^{-1} \mathbf{W})^{-1} \boldsymbol{\chi}_0 \\ &= \mathbf{S} \bar{\mathbf{D}}^T \boldsymbol{\lambda} \mathbf{d} \bar{\mathbf{D}} \mathbf{S} + \mathbf{S} \bar{\mathbf{D}}^T \boldsymbol{\lambda} \mathbf{d} \bar{\mathbf{F}} \left(\tilde{\mathbf{I}} - \bar{\mathbf{D}}^T \boldsymbol{\lambda} \mathbf{d} \bar{\mathbf{F}} \right)^{-1} \bar{\mathbf{D}}^T \boldsymbol{\lambda} \mathbf{d} \bar{\mathbf{D}} \mathbf{S} \\ &= \mathbf{S} \tilde{\mathbf{C}} \mathbf{S}.\end{aligned}\tag{B.24}$$

Now we can rewrite the hybrid version of $\tilde{\mathbf{C}}$ into our notations:

$$\begin{aligned}
\boldsymbol{\chi} &= \mathbf{S}\tilde{\mathbf{C}}\mathbf{S} \\
&= \mathbf{S}\bar{\mathbf{D}}^T \boldsymbol{\lambda}\mathbf{H}^{(2)}\bar{\mathbf{D}}\mathbf{S} + \mathbf{S}\bar{\mathbf{D}}^T \boldsymbol{\lambda}\bar{\mathbf{F}}' \left(\tilde{\mathbf{I}} - \bar{\mathbf{D}}^T \boldsymbol{\lambda}\bar{\mathbf{F}}' \right)^{-1} \bar{\mathbf{D}}^T \boldsymbol{\lambda}\mathbf{H}^{(2)}\bar{\mathbf{D}}\mathbf{S} \\
&= \boldsymbol{\chi}'_0 + \left(\boldsymbol{\chi}'_0 \mathbf{S}^{-1} \mathbf{W} + \frac{1}{4} \mathbf{K}(\mathbf{R}^T)^{-1} \mathbf{S} \right) \\
&\quad \left[\mathbf{S} - \left(\boldsymbol{\chi}'_0 \mathbf{S}^{-1} \mathbf{W} + \frac{1}{4} \mathbf{K}(\mathbf{R}^T)^{-1} \mathbf{S} \right) \right]^{-1} \boldsymbol{\chi}'_0.
\end{aligned} \tag{B.25}$$

REFERENCES

- ¹D. Hankins, J. W. Moskowitz, and F. H. Stillinger, “Water molecule interactions”, *J. Chem. Phys.* **53**, 4544 (1970).
- ²H. Stoll and H. Preuß, “On the direct calculation of localized hf orbitals in molecular clusters, layers and solids”, *Theor. Chim. Acta* **46**, 11 (1977).
- ³K. Raghavachari, G. W. Trucks, J. A. Pople, and M. Head-Gordon, “A 5th-order perturbation comparison of electron correlation theories”, *Chem. Phys. Lett.* **157**, 479–483 (1989).
- ⁴M. Pitoňák, P. Neogrady, J. Černý, S. Grimme, and P. Hobza, “Scaled mp3 non-covalent interaction energies agree closely with accurate ccsd(t) benchmark data”, *Chem. Phys. Chem.* **10**, 282 (2009).
- ⁵T. Takatani, E. G. Hohensten, and C. D. Sherrill, “Improvement of the coupled-cluster singles and doubles method via scaling same- and opposite-spin components of the double excitation correlation energy”, *J. Chem. Phys.* **128**, 124111 (2008).
- ⁶M. Pitoňák, J. Řezáč, and P. Hobza, “Spin-component scaled coupled-clusters singles and doubles optimized towards calculation of noncovalent interactions”, *Phys. Chem. Chem. Phys.* **12**, 9611 (2010).
- ⁷S. Grimme, J. Antony, S. Ehrlich, and H. Krieg, “A consistent and accurate ab initio parametrization of density functional dispersion correction (dft-d) for the 94 elements h-pu”, *J. Chem. Phys.* **132**, 154104 (2010).
- ⁸E. Caldeweyher, S. Ehlert, A. Hansen, H. Neugebauer, S. Spicher, C. Bannwarth, and S. Grimme, “A generally applicable atomic-charge dependent london dispersion correction”, *J. Chem. Phys.* **150**, 154122 (2019).
- ⁹S. F. Boys and F. Bernardi, “The calculation of small molecular interactions by the differences of separate total energies. some procedures with reduced errors”, *Mol. Phys.* **18**, 553 (1970).
- ¹⁰B. Jeziorski, R. Moszynski, and K. Szalewicz, “Perturbation theory approach to intermolecular potential energy surfaces of van der Waals complexes”, *Chem. Rev.* **94**, 1887–1930 (1994).
- ¹¹K. Szalewicz, “Symmetry-adapted perturbation theory of intermolecular forces”, *WIREs Comput. Mol. Sci.* **2**, 254–272 (2012).

- ¹²E. G. Hohenstein and C. D. Sherrill, “Wavefunction methods for noncovalent interactions”, *WIREs Comput. Mol. Sci.* **2**, 304–326 (2012).
- ¹³C. D. Sherrill, “Energy component analysis of π interactions”, *Acc. Chem. Res.* **46**, 1020–1028 (2013).
- ¹⁴H. L. Williams and C. F. Chabalowski, “Using kohn-sham orbitals in symmetry-adapted perturbation theory to investigate intermolecular interactions”, *J. Phys. Chem. A* **105**, 646–659 (2001).
- ¹⁵J. P. Perdew and M. Levy, “Physical content of the exact kohn-sham orbital energies: band gaps and derivative discontinuities”, *Phys. Rev. Lett.* **51**, 1884 (1983).
- ¹⁶G. Jansen and A. Heßelmann, “Comment on using kohnsham orbitals in symmetry-adapted perturbation theory to investigate intermolecular interactions”, *J. Phys. Chem. A* **105**, 11156–11157 (2001).
- ¹⁷A. Heßelmann and G. Jansen, “Intermolecular induction and exchange-induction energies from coupled-perturbed kohn-sham density functional theory”, *Chem. Phys. Lett.* **362**, 319–325 (2002).
- ¹⁸K. Patkowski, K. Szalewicz, and B. Jeziorski, “Orbital relaxation and the third-order induction energy in symmetry-adapted perturbation theory”, *Theor. Chem. Acc.* **127**, 211 (2010).
- ¹⁹A. Heßelmann and G. Jansen, “First-order intermolecular interaction energies from kohn-sham orbitals”, *Chem. Phys. Lett.* **357**, 464–470 (2002).
- ²⁰J. P. Perdew, K. Burke, and M. Ernzerhof, “Generalized gradient approximation made simple”, *Phys. Rev. Lett.* **77**, 3865–3868 (1996).
- ²¹C. Adamo and V. Barone, “Toward reliable density functional methods without adjustable parameters: the pbe0 model”, *J. Chem. Phys.* **110**, 6158–6170 (1999).
- ²²R. van Leeuwen and E. J. Baerends, “Exchange-correlation potential with correct asymptotic behavior”, *Phys. Rev. A* **49**, 2421 (1994).
- ²³M. Grüning, O. V. Gritsenko, S. J. A. van Gisbergen, and E. J. Baerends, “Shape corrections to exchange-correlation potentials by gradient-regulated seamless connection of model potentials for inner and outer region”, *J. Chem. Phys.* **114**, 652–660 (2001).
- ²⁴A. J. Misquitta and K. Szalewicz, “Intermolecular forces from asymptotically corrected density functional description of monomers”, *Chem. Phys. Lett* **357**, 301 (2002).
- ²⁵E. Fermi and G. Amaldi, *Mem. Acad. Italia* **6**, 117 (1934).

- ²⁶D. J. Tozer and N. C. Handy, “Improving virtual kohnsham orbitals and eigenvalues: application to excitation energies and static polarizabilities”, *J. Chem. Phys.* **109**, 10180 (1998).
- ²⁷G. Jansen, “Symmetry-adapted perturbation theory based on density functional theory for noncovalent interactions”, *WIREs Comput. Mol. Sci.* **4**, 127–144 (2014).
- ²⁸A. J. Misquitta and K. Szalewicz, “Symmetry-adapted perturbation-theory calculations of intermolecular forces employing density-functional description of monomers”, *J. Chem. Phys.* **122**, 214109 (2005).
- ²⁹A. Heßelmann and G. Jansen, “Intermolecular dispersion energies from time-dependent density functional theory”, *Chem. Phys. Lett.* **367**, 778–784 (2003).
- ³⁰A. J. Misquitta, R. Podeszwa, B. Jeziorski, and K. Szalewicz, “Intermolecular potentials based on symmetry-adapted perturbation theory with dispersion energies from time-dependent density-functional calculations”, *J. Chem. Phys.* **123**, 214103 (2005).
- ³¹E. J. Baerends, D. E. Ellis, and P. Ros, “Self-consistent molecular hartree-fock-slater calculations - i. the computational procedure”, *Chem. Phys.* **2**, 41–51 (1973).
- ³²J. L. Whitten, “Coulombic potential-energy integrals and approximations”, *J. Chem. Phys.* **58**, 4496–4501 (1973).
- ³³S. J. A. van Gisbergen, F. Kootstra, P. R. T. Schipper, O. V. Gritsenko, J. G. Snijders, and E. J. Baerends, “Density-functional-theory response-property calculations with accurate exchange-correlation potentials”, *Phys. Rev. A* **57**, 2556 (1998).
- ³⁴A. Heßelmann, G. Jansen, and M. Schütz, “Density-functional theory-symmetry-adapted intermolecular perturbation theory with density fitting: a new efficient method to study intermolecular interaction energies”, *J. Chem. Phys.* **122**, 014103 (2005).
- ³⁵A. J. Misquitta, B. Jeziorski, and K. Szalewicz, “Dispersion energy from density-functional theory description of monomers”, *Phys. Rev. Lett.* **91**, 033201 (2003).
- ³⁶R. Bukowski, R. Podeszwa, and K. Szalewicz, “Efficient calculation of coupled kohnsham dynamic susceptibility functions and dispersion energies with density fitting”, *Chem. Phys. Lett.* **414**, 111–116 (2005).
- ³⁷F. Della Sala and A. Görling, “Efficient localized hartree-fock methods as effective exact-exchange kohn-sham methods for molecules.”, *J. Chem. Phys.* **115**, 5718 (2001).
- ³⁸R. Bukowski, W. Cencek, J. Garcia, P. Jankowski, M. Jeziorska, B. Jeziorski, S. A. Kucharski, V. F. Lotrich, M. P. Metz, A. J. Misquitta, R. Moszyński, K. Patkowski, R. Podeszwa, F. Rob, S. Rybak, K. Szalewicz, H. L. Williams, R. J. Wheatley, P. E. S.

- Wormer, and P. S. Żuchowski, *SAPT2020: an ab initio program for many-body symmetry-adapted perturbation theory calculations of intermolecular interaction energies*, University of Delaware and University of Warsaw, 2020.
- ³⁹M. Pitonak and A. Heßelmann, “Accurate intermolecular interaction energies from a combination of mp2 and tddft response theory”, *J. Chem. Theory Comput.* **6**, 168–178 (2010).
- ⁴⁰Y. C. Zheng and J. Almlöf, “Density functionals without meshes and grids”, *Chem. Phys. Lett.* **214**, 397 (1993).
- ⁴¹Y. C. Zheng and J. Almlöf, “A grid-free dft implementation of non-local functionals and analytical energy derivatives”, *Mol. Struct. (THEOCHEM)* **388**, 277 (1996).
- ⁴²K. R. Glaesemann and M. S. Gordon, “Investigation of a grid-free density functional theory (dft) approach”, *J. Chem. Phys.* **108**, 9959 (1998).
- ⁴³A. Heßelmann and T. Korona, “Intermolecular symmetry-adapted perturbation theory study of large organic complexes”, *J. Chem. Phys.* **141**, 094107 (2014).
- ⁴⁴L. Gráfová, M. Pitoňák, J. Řezáč, and P. Hobza, “Comparative study of selected wave function and density functional methods for noncovalent interaction energy calculations using the extended S22 data set”, *J. Chem. Theory Comput.* **6**, 2365–2376 (2010).
- ⁴⁵J. Řezáč, K. E. Riley, and P. Hobza, “S66: A well-balanced database of benchmark interaction energies relevant to biomolecular structures”, *J. Chem. Theory Comput.* **7**, 2427–2438 (2011).
- ⁴⁶J. Řezáč, K. E. Riley, and P. Hobza, “Erratum to s66: a well-balanced database of benchmark interaction energies relevant to biomolecular structures”, *J. Chem. Theory Comput.* **10**, 1359–1360 (2014).
- ⁴⁷J. Řezáč, K. E. Riley, and P. Hobza, “Extensions of the s66 data set: more accurate interaction energies and angular-displaced nonequilibrium geometries”, *J. Chem. Theory Comput.* **7**, 3466–3470 (2011).
- ⁴⁸D. G. A. Smith, L. A. Burns, A. C. Simmonett, R. M. Parrish, M. C. Schieber, R. Galvelis, P. Kraus, H. Kruse, R. Di Remigio, A. Alenaizan, A. M. James, S. Lehtola, J. P. Misiewicz, M. Scheurer, R. A. Shaw, J. B. Schriber, Y. Xie, Z. L. Glick, D. A. Sirianni, J. S. O’Brien, J. M. Waldrop, A. Kumar, E. G. Hohenstein, B. P. Pritchard, B. R. Brooks, H. F. Schaefer, A. Y. Sokolov, K. Patkowski, A. E. DePrince, U. Bozkaya, R. A. King, F. A. Evangelista, J. M. Turney, T. D. Crawford, and C. D. Sherrill, “PSI4 1.4: OPEN-SOURCE SOFTWARE FOR HIGH-THROUGHPUT QUANTUM CHEMISTRY”, *J. Chem. Phys.* **152**, 184108 (2020).

- ⁴⁹R. Podeszwa, R. Bukowski, and K. Szalewicz, “Density-fitting method in symmetry-adapted perturbation theory based on Kohn-Sham description of monomers”, *J. Chem. Theory Comput.* **2**, 400–412 (2006).
- ⁵⁰A. Heßelmann, “Die berechnung von intermolekularen wechselwirkungsbeiträgen mit dichtefunktional- und brueckner-coupled-cluster-methoden”, PhD thesis (University Duisburg-Essen, Essen, 2003).
- ⁵¹J. P. Perdew, R. G. Parr, M. Levy, and J. L. Balduz Jr., “Investigation of a grid-free density functional theory (dft) approach”, *Phys. Rev. Lett.* **49**, 1691 (1982).
- ⁵²M. Jaszunski and R. McWeeny, “Time-dependent hartree-fock calculations of dispersion energy”, *Mol. Phys.* **55**, 1275 (1985).
- ⁵³P. J. Knowles and W. J. Meath, “Non-expanded dispersion and induction energies, and damping functions, for molecular interactions with application to hf-he”, *Mol. Phys.* **59**, 965 (1986).
- ⁵⁴J. Garcia and K. Szalewicz, “Ab initio extended hartree-fock plus dispersion method applied to dimers with hundreds of atoms”, *J. Chem. Phys. A* **124**, 1196 (2020).
- ⁵⁵T. H. D. Jr., “Gaussian basis sets for use in correlated molecular calculations. i. the atoms boron through neon and hydrogen”, *J. Chem. Phys.* **90**, 1007 (1989).
- ⁵⁶R. A. Kendall, T. H. D. Jr., and R. J. Harrison, “Electron affinities of the firstrow atoms revisited. systematic basis sets and wave functions”, *J. Chem. Phys.* **96**, 6796 (1992).
- ⁵⁷T. Korona, “A coupled cluster treatment of intramonomer electron correlation within symmetry-adapted perturbation theory: benchmark calculations and a comparison with a density-functional theory description”, *Mol. Phys.* **111**, 3705–3715 (2013).
- ⁵⁸T. M. Parker, L. A. Burns, R. M. Parrish, A. G. Ryno, and C. D. Sherrill, “Levels of symmetry adapted perturbation theory (SAPT). I. Efficiency and performance for interaction energies”, *J. Chem. Phys.* **140**, 094106 (2014).
- ⁵⁹H. L. Williams, K. Szalewicz, R. Moszynski, and B. Jeziorski, “Dispersion energy in the coupled pair approximation with noniterative inclusion of single and triple excitations”, *J. Chem. Phys.* **103**, 4586–4599 (1995).
- ⁶⁰MOLPRO, version 2019.2, a package of ab initio programs, H.-J. Werner, P. J. Knowles, G. Knizia, F. R. Manby, M. Schütz, P. Celani, W. Györffy, D. Kats, T. Korona, R. Lindh, A. Mitrushenkov, G. Rauhut, K. R. Shamasundar, T. B. Adler, R. D. Amos, S. J. Bennie, A. Bernhardsson, A. Berning, D. L. Cooper, M. J. O. Deegan, A. J. Dobbyn, F. Eckert, E. Goll, C. Hampel, A. Heßelmann, G. Hetzer, T. Hrenar, G. Jansen, C. Köppl, S. J. R. Lee, Y. Liu, A. W. Lloyd, Q. Ma, R. A. Mata, A. J. May, S. J. McNicholas, W. Meyer, T.

- F. Miller III, M. E. Mura, A. Nicklass, D. P. O'Neill, P. Palmieri, D. Peng, T. Petrenko, K. Pflüger, R. Pitzer, M. Reiher, T. Shiozaki, H. Stoll, A. J. Stone, R. Tarroni, T. Thorsteins-son, M. Wang, and M. Welborn, see <https://www.molpro.net>.
- ⁶¹F. Weigend and R. Ahlrichs, “Balanced basis sets of split valence, triple zeta valence and quadruple zeta valence quality for h to rn: design and assessment of accuracy”, *Phys. Chem. Chem. Phys.* **7**, 3297 (2005).
- ⁶²P. Jurečka, J. Šponer, J. Černý, and P. Hobza, “Benchmark database of accurate (MP2 and CCSD(T) complete basis set limit) interaction energies of small model complexes, DNA base pairs, and amino acid pairs”, *Phys. Chem. Chem. Phys.* **8**, 1985–1993 (2006).
- ⁶³C. Mück-Lichtenfeld, S. Grimme, L. Kobryn, and A. Sygula, “Inclusion complexes of buckycatcher with c-60 and c-70”, *Phys. Chem. Chem. Phys.* **12**, 7091–7097 (2010).
- ⁶⁴R. Podeszwa, W. Cencek, and K. Szalewicz, “Efficient calculations of dispersion energies for nanoscale systems from coupled density response functions”, *J. Chem. Theory Comput.* **8**, 1963–1969 (2012).
- ⁶⁵R. Podeszwa, B. M. Rice, and K. Szalewicz, “Predicting structure of molecular crystals from first principles”, *Phys. Rev. Lett.* **101**, 115503 (2008).
- ⁶⁶S. Wen and G. J. O. Beran, “Accurate molecular crystal lattice energies from a fragment qm/mm approach with on-the-fly ab initio force field parametrization”, *J. Chem. Theory Comput.* **7**, 3733 (2011).
- ⁶⁷M. Kamiya, S. Hirata, and M. Valiev, “Fast electron correlation methods for molecular clusters without basis set superposition errors”, *J. Chem. Phys.* **128**, 074103 (2008).
- ⁶⁸J. Řezáč, Y. Huang, P. Hobza, and G. J. O. Beran, “Benchmark calculations of three-body intermolecular interactions and the performance of low-cost electronic structure methods”, *J. Chem. Theory Comput.* **11**, 3065 (2015).
- ⁶⁹A. Sebetti and G. J. O. Beran, “Spatially homogeneous qm/mm for systems of interacting molecules with on-the-fly ab initio force-field parametrization”, *J. Chem. Theory Comput.* **6**, 155 (2010).
- ⁷⁰B. M. Axilrod and E. Teller, “Interaction of the van der waals type between three atoms”, *J. Chem. Phys.* **11**, 299 (1943).
- ⁷¹Y. Muto, “Regarding intermolecular forces between non-polar molecules”, *Proc. Phys. Math. Soc. Jpn.* **17**, 629 (1943).
- ⁷²R. Podeszwa and K. Szalewicz, “Three-body symmetry-adapted perturbation theory based on kohn-sham description of the monomers”, *J. Chem. Phys.* **126**, 194101 (2007).

- ⁷³Y. Huang and G. J. O. Beran, “Reliable prediction of three-body intermolecular interactions using dispersion-corrected second-order møller-plesset perturbation theory”, *J. Chem. Phys.* **143**, 044113 (2015).
- ⁷⁴R. J. Bell, “Multipolar expansion for the non-additive third-order interaction energy of three atoms”, *J. Phys. B: Atom. Mol. Phys.* **3**, 751 (1970).
- ⁷⁵E. Caldeweyher, C. Bannwarth, and S. Grimme, “Extension of the d3 dispersion coefficient model”, *J. Chem. Phys.* **147**, 034112 (2017).
- ⁷⁶E. Caldeweyher, J.-M. Mewes, S. Ehlert, and S. Grimme, “Extension and evaluation of the d4 london-dispersion model for periodic systems”, *Phys. Chem. Chem. Phys.* **22**, 8499 (2020).
- ⁷⁷A. Tkatchenko, R. A. DiStasio, R. Car, and M. Scheffler, “Accurate and efficient method for many-body van der waals interactions”, *Phys. Rev. Lett.* **108**, 236402 (2012).
- ⁷⁸K. T. Tang and J. P. Toennies, “An improved simple model for the van der waals potential based on universal damping functions for the dispersion coefficients”, *J. Chem. Phys.* **80**, 3726 (1984).
- ⁷⁹J.-D. Chai and M. Head-Gordon, “Long-range corrected hybrid density functionals with damped atom–atom dispersion corrections”, *Phys. Chem. Chem. Phys.* **10**, 6615 (2000).
- ⁸⁰S. Grimme, S. Ehlrich, and L. Goerigk, “Effect of the damping function in dispersion corrected density functional theory”, *J. Comput. Chem.* **32**, 1456 (2011).
- ⁸¹Y. Xie, D. G. A. Smith, and C. D. Sherrill, “Implementation of symmetry-adapted perturbation theory based on density functional theory and using hybrid exchange-correlation kernels for dispersion terms”, *J. Chem. Phys.* **157**, 024801 (2022).
- ⁸²F. H. Allen, “The cambridge structural database: a quarter of a million crystal structures and rising”, *Acta Crystallogr., Sect. B: Struct. Sci.* **58**, 380 (2002).
- ⁸³C. H. Borca, B. W. Bakr, L. A. Burns, and C. D. Sherrill, “Crystalatte: automated computation of lattice energies of organic crystals exploiting the many-body expansion to achieve dual-level parallelism”, *J. Chem. Phys.* **151**, 144103 (2019).
- ⁸⁴A. Halkier, T. Helgaker, P. Jørgensen, W. Klopper, H. Koch, J. Olsen, and A. K. Wilson, “Basis-set convergence in correlated calculations on ne, n₂, and h₂o”, *Chem. Phys. Lett.* **286**, 243 (1998).
- ⁸⁵L. A. Burns, M. S. Marshall, and C. D. Sherrill, “Comparing counterpoise-corrected, uncorrected, and averaged binding energies for benchmarking noncovalent interactions”, *J. Chem. Theory Comput.* **10**, 49 (2014).

- ⁸⁶M. O. Sinnokrot, E. F. Valeev, and C. D. Sherrill, “Estimates of the ab initio limit for pi–pi interactions: the benzene dimer”, *J. Am. Chem. Soc.* **124**, 10887 (2002).
- ⁸⁷R. Bukowski and K. Szalewicz, “Complete ab initio three-body nonadditive potential in monte carlo simulations of vapor–liquid equilibria and pure phases of argon”, *J. Chem. Phys.* **114**, 9518 (2001).
- ⁸⁸J. G. McDaniel and J. R. Schmidt, “First-principles many-body force fields from the gas phase to liquid: a “universal” approach”, *J. Phys. Chem. B* **118**, 8042 (2014).